NORTHWESTERN UNIVERSITY

Controlling Magneto-optical Properties in 2D InSe

A DISSERTATION

SUBMITTED TO THE GRADUATE SCHOOL
IN PARTIAL FULFILLMENT OF THE REQUIREMENTS

for the degree

DOCTOR OF PHILOSOPHY

Applied Physics

By

Jovan J. Nelson

EVANSTON, ILLINOIS

June 2023

ABSTRACT

Light is a powerful tool for manipulating and probing magnetic states in solid state systems. In particular, optically-induced spin orientation, the ability to orient spin with polarized light, has been extensively utilized in low-dimensional III-V and II-VI semiconductors to pioneer spintronic research. Even though traditional semiconductors have found a wide range of applications, recent research on atomically thin van der Waals materials has revealed intriguing low-dimensional landscapes for optical spin manipulation.

Transition metal dichalcogenides are the standard van der Waals semiconductors that have optical selection rules that allow for the coupling between light and spin. These spins states are locked to valleys, a pseudospin state that is the basis of valleytronics. Yet, TMDs can be limited by spin-valley locking, a phenomenon that strongly couples carrier spin projection to momentum, making it difficult to freely manipulate pseudospin states. In contrast, it is much easier to freely manipulate spins in traditional semiconductors. Platforms that possess free spin manipulation can be more viable candidates for information applications.

Recently, another class of layered materials, III-VI monochalcogenides, has gained significant attention due to their favorable electronic, optical, and magnetic characteristics. Amongst this general class of materials, the optoelectronic attributes of Indium Selenide (InSe) have been seen as considerably beneficial. In addition, there are predictions of spin-polarized optical selection rules near the Γ point, implying no spin-valley locking in layered InSe. In this dissertation, optically-induced spin orientation is verified in InSe, opening the door for controlling optical spin phenomena in a van der Waals material with robust electronic and optical properties. Following this result, this body of work presents studies that reveal fundamental physics governing optical spin dynamics in InSe. When all of these properties are considered together, they motivate fu-

ture research. In particular, combining InSe with 2D magnets for enhanced control over optical spin phenomena. Although there are still many unanswered questions, this dissertation contributes significantly to the body of knowledge of optical spin properties in InSe. Ultimately, aiding the exploration of InSe's potential for future spintronic applications.

ACKNOWLEDGEMENTS

First, I thank God for the opportunity to pursue a Ph.D and for keeping me through all the hardships and difficulties. In Jesus Christ, I find my hope that shines in the darkness. ”Thy word is a lamp unto my feet, and a light unto my path.” - Psalm 119:105.

Thank you to my mother who raised me as a single-parent since I was eight-years old. She has always encouraged me and has helped shape me into the person I am today. Her words, ”You can do anything you put your mind to” and ”Did you do your best? Well, that is all that really matters”, have stuck with me all my life. In many ways, this is also her Ph.D because I wouldn’t be here without her.

Thank you to my father, who passed away when I was eight-years old. I remember the times we would build cars, castles, etc. out of Legos together. I remember asking a million questions while we walked the dogs during a Sunday afternoon. Though you may not be here on Earth to see this, I hope you have a smile on your face up in heaven.

Thanks to all my other family members for your support and prayers. Family functions or other types of hang outs have been filling and life giving. I love you all and appreciate you.

Thank you to my S/O, Sarah K., for all the support and prayers these last couple months. The short time I have spent with you has been fun, adventurous, and filling. You help recharge my battery and have made the Ph.D journey so much more manageable. You have been one of the greatest blessings of my life.

Thank you to everyone in the Graduate Christian Fellowship for your friendships and prayers. Shout out to Tuesday small group (old and new) for great bible studies, snacks, and ice-breaker questions. Shout out to the ”GCF Boiis” for growing in vulnerability and friendship. Also thanks to Mickey Sanchez, InterVarsity staff member, who has been a great spiritual mentor. Thank you

for allowing me to share my doubts and be willing to help guide my spiritual journey.

Thanks to all the good friends I have made before or during my time at Northwestern. Eden and Dr. Bright, we connected during a private screening of the first Black Panther movie, organized by the Northwestern Black Graduate Student Association. Both of you have been good friends since the early days of my Ph.D. Thanks to SPL and Dr. Ashely for ping pong games and helping me step up my drip game (if only a little). Thanks to Dany and Stephen for good coffee chats and good food. Thank you Bronson, Mac, Miranda, Ali Rezai, Alyona, and Dom for listening to my struggles in grad school and giving words of encouragement. Y'all four are friends whom I've known, like, forever.

Thanks to my Applied Physics cohort for being a supportive and lovely group of people. You all were very instrumental in getting though classes, the qualifying exam, and prospectus. Thanks Dr. Hang for the H-Mart grocery runs. Thanks Dr. Sruthi for the mid-work hot chocolate breaks in Kellogg. Thanks Alex for making bread and teaching us how to do it ourselves (I still have your bowl). Thanks Bianca for making vegan cookies when someone had a bad day. Thanks Ali Ehlen for the energy and always inviting us over to party at your house.

Thank you to the three professors at Brown University who helped inspire me during my undergraduate career, which ultimately led me to continue to do a Ph.D. Thank you Prof. Meenakshi Narain for taking me under your wing and caring for both my career and personal development. Because of you, I got to start research early, which was instrumental in my academic career. Rest in peace, you will be missed. Thank you Prof. James Valles for being supportive during my entire time as an undergraduate. Even though I never took a class with you or worked in your research group, you always took the time to meet and help me figure out next steps in my career. Thank you Prof. Chung-I Tan for writing that note in my first physics exam in college, an exam that I completely failed. Because you took the extra time to help me catch up with the rest of the class, I

continued with physics and will earn a Ph.D in Applied Physics (close enough to physics).

Thanks to all the members of the Stern group for support, encouragement, good snacks, and good conversations. Especially wanted to thank Dr. Trevor, the ”Pump-Probe Wiz”, for his patients and showing me the ropes in my first year.

Thanks to Dr. Dima for making all the key samples that I have used in my research. Thanks to Dr. Shawn, though we only worked together for a short period of time, I enjoyed the late nights we chatted it up while doing experiments in the lab.

Thanks to my advisor Dr. Nathaniel Stern for research and academic support. I appreciated that you made yourself available, provided good feedback on my work, gave me a good amount of autonomy in terms of research and career development, and facilitated collaborations with other research groups across different disciplines. This helped me become a confident and independent research scientist.

Funding Acknowledgements

This material is based upon work primarily supported by the National Science Foundation under Grant No. DMR-1905986 and by the National Science Foundation’s MRSEC program (Grant No. DMR-1720139) at the Materials Research Center of Northwestern University. The author was supported by the National Science Foundation Graduate Research Fellowship (Grant No. DGE-184216).

List of Abbreviations

2D - Two Dimensional

CrI_3 - Chromium Iodide

DFT - Density Functional Theory

DP - D'yakonov-Perel

EY - Elliot-Yafet

Gr - Graphene

FET - Field Effect Transistor

hBN - Hexagonal Born Nitride

InSe- Indium Selenide

OISO - Optically-induced Spin Orientation

PL - Photoluminescence

SOC - Spin-orbit Coupling

TMD - Transition Metal Dichalcogenide

TR - Transient Reflection

TRKR - Time-resolved Kerr rotation

TRPL - Time-resolved Photoluminescence

TABLE OF CONTENTS

LIST OF FIGURES

LIST OF TABLES

CHAPTER 1

INTRODUCTION

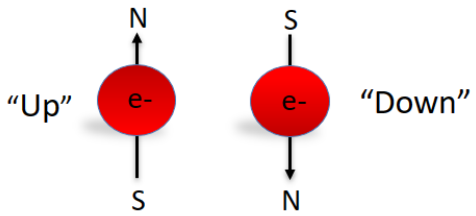

Figure 1.1: Illustration of the two spin states of an electron, 'up' and 'down'. The spin and charge degrees of freedom are essential properties of an electron that can be utilized in spintronics.

Scientific progress has been advanced through the utilization of "probes" and "knobs". A good probe gives a nondestructive evaluation of a system whereas a good knob gives dynamic control of a system's properties. For the physical sciences, "knobs" and "probes" can be electrical, magnetic, optical, chemical, or structural in nature. The available types of probes and knobs determine what can be done with a system and ultimately its potential function. An example of such is a spin system, which has applications in information processing and has both classical and quantum regimes. Therefore, the tools at our disposal to evaluate and control these systems are critical to contemporary research. Spin gains its enticing qualities from a simple principle, magnetic moments pointing "up" or "down". The transition between spin states can be energetically favorable, thus permitting efficient spin transfer and spin flip-flop. Typically, spin is coupled to a magnetic stimuli, yet in a number of spin systems, polarized optical fields have proven to be powerful tools [1]. These tools are used to conduct in-depth investigations (probe) and manipulate dynamically (knob), spin phenomena in low-dimensional solid-state materials.

1.1 Optically Induced Spin Orientation in Semiconductors and Spintronic Applications

The continuous demand for high-speed computing and high-density storage has driven the hunt for speedy and efficient control over spins in solid-state systems. Understanding the underlying physics in solid-state spin systems can enhance our ability to achieve these goals [2]. In particular, semiconductors are advantageous platforms to conduct studies on magnetic phenomena, as they have interesting coupling effects between spin and other degrees of freedom [3]. They are also compatible with current successful technologies such as complementary metal-oxide-semiconductor, which has made our current technological age possible [4].

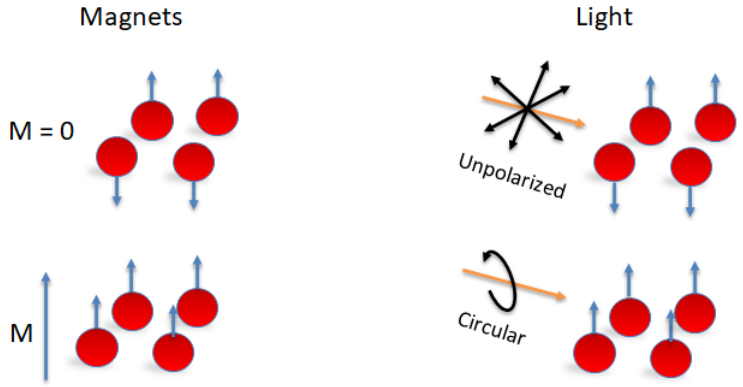

Figure 1.2: Artistic representation of controlling electron spin in solid state systems. Magnets (left image) and light (right image) are two different 'knobs' that can be used to manipulate spin.

Often, the carrier of interest in these materials are electrons, because they tend to be mobile and tunable. The two fundamental intrinsic properties of an electron are charge and spin, which are influenced by electric and magnetic fields respectively. Thereby, offering two different methods to interact with this particle. Manipulating charge of an electron is the basis of electronics, while spintronics aims to control electrons in a system through spin. The standard approach for spin control involves ferromagnetic materials which can be switched between magnetic states by currents,

external fields, or both. Although permanent magnets are preferred, since they can be integrated into current semiconducting technologies, they are typically static and slow. On the other hand, all-optical control of spin in materials, enabled by polarization-dependent optical selection rules, present opportunities for fast, nondestructive, and magnet free control over spin information [5]. Optically induced spin orientation (OISO), a key ingredient for spin injection, has been capitalized in low-dimensional III-V and II-VI semiconductors for spintronic applications. These materials have pioneered spin transport [6], spin memory [7], and spin coherence [8]. Three properties that are quintessential for transferring, storing, and manipulating spin information effectively.

Even though semiconducting materials like GaAs have many applications and can be fabricated as low-dimensional platforms, they do posses limitations. This manifests as constraints in fabrication. For example, lattice matching imposes constraints on heterostructures that can be engineered, as materials with very different crystal structures do not couple well if combined [9]. Traditional semiconductors also tend to form structures in three dimensions, making it easier for unpaired bonds to exist on the surface. These dangling bonds not only make surface physics more unruly in these systems, they make thin films of these materials into quasi two-dimensional (2D) structures [10]. Fortunately, within the last two decades, a new class of materials emerged with true 2D nature and the ability to optically orient spin.

1.2 Two Dimensional Materials for Novel Optical Spin Applications

The discovery of atomically thin graphene (Gr) [11] jump started the entire field of 2D van der Waals materials. These materials are 2D in the truest sense, since they are sheets of atoms bounded by weak forces (van der Waals) in the out-of-plane direction and strong forces (covalent) in the in-plane direction. This creates systems that are mostly surface and very flexible. Plus, these crystal compositions can lead to exotic band structures. A variety of 2D systems exist with exemplary

electronic, optical, and magnetic properties [12]–[14].

Due to similar hexagonal crystal structures, it is also possible to conduct layer-by-layer engineering in 2D heterostructures. This engineering approach can be utilized by combining 2D systems that compliment one another. For example, in WSe_2/Gr heterostructures, the paring of large spin-orbit coupling for valley-spin manipulation (WSe2) and high conductance for electronics (graphene) has shown novel influence over valley-spin dynamics [15]. Thus, layer-by-layer engineering presents a promising approach to build 2D systems with enhanced control and detection of spin phenomena [3], [12]. This then motivates searching for comparable or more novel 2D analogs to traditional semiconductors, materials that have already produced a wealth of spintronic research [5].

Several 2D semiconductors have properties appealing for low-dimensional spin-based devices, such as high electron mobility and charge carrier densities that are tunable by gating [16]. Gr based devices, for example, have demonstrated spin transport and spin precession over long channels [17], and has been predicted to have optically generated spin polarization without an external field [18]. Unfortunately, Gr is limited in its scope for OISO as it is plagued by weak spin-orbit coupling (SOC) [19].

The canonical example of 2D materials with nontrivial optical and spin properties, are Transition Metal Dichalcogenides (TMDs). Strong SOC creates the conditions for control of pseudospin states through optical selection rules, reproducing many optical features of spin materials. Excitons and other carriers can be optically excited by polarized light into 'valleys', which are direct band gap transitions separated in k-space for monolayer TMDs. The optical access to these valley polarized states mimic selection rules required for OISO [20]–[22]. The application of valleys creates a parallel to spintronics, 'valleytronics', where valley-based devices have demonstrated "valley Hall effect" [23] and strong spin-valley locking [24], which are favorable for the transfer

and long-term storage of information. Another notable property that has been studied in TMDs, is strong light-matter interactions that occur when monolayers are place into optical cavities. This was experimentally investigated by LaMountain *et. al* using the optical Stark effect [25]. This work showed the rich potential for valley-selective control over polaritons (light states) in TMDs. These exciton-polariton states have been shown extensively in traditional semiconductors [26]–[29]. Thus, LaMountain *et. al* have helped further demonstrate the relevant analogue between valley and spin.

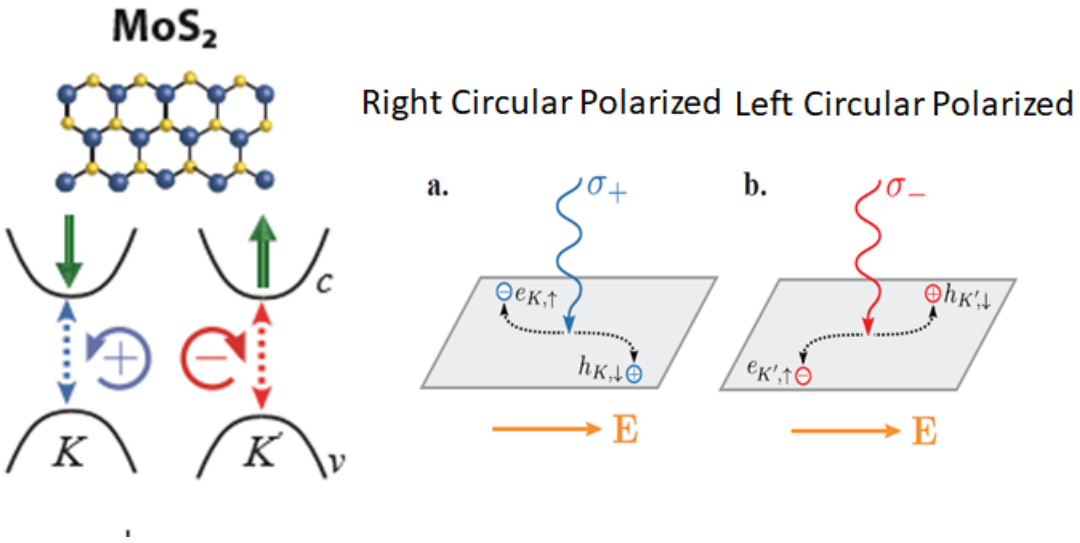

Figure 1.3: On the left is an illustration of direct band gaps at K-valleys for monolayer MoS_2. The right depicts "valleytronics" in action.

Yet, even with analogues properties to traditional spin systems, TMDs are far from being optimal for electronic or spin-based devices. TMD mobilities are small and spin-valley locking can impede the ability to freely manipulate psuedospins without very large fields [30], [31]. In contrast, III-V semiconductors such as GaAs, in both bulk and confined regimes, have good spintronic performance due to highly mobile electrons [32] that can be freely manipulated in reasonable mag-

netic fields [6]. Ultimately, making these traditional materials more viable platforms for quantum information applications [8], [33] than TMDs. This reality motivates a relevant and contemporary question: is there a 2D material with comparable (or better) optical, electronic, and spin properties to that of traditional semiconductors?

1.3 Thesis Work: Controlling Optical Spin Properties in 2D InSe

Group III-VI monochalcogenides, such as GaSe and InSe, have garnered renewed recognition over the last few years. Largely due to the discovery of beneficial electronic and magnetic properties that exist in thin layers [34]–[38]. This general class of semiconductors are a unique platform for optical spin-based devices because they merge layer-by-layer engineering with optical control of spin, a feature utilized in traditional semiconductors for decades [5].

From the broader class of III-VI monochalcogenides, InSe has obtained considerable attention due to its several remarkable optoelectronic properties. At low temperature, a few-layer InSe device has electron mobility as high as 10^4 $\mathrm{cm^2V^{-1}s^{-1}}$ and the quantum hall effect has been experimentally observed [38]. Similar to TMDs, InSe has a layer-dependent band gap and tightly bound excitons ($\sim$ 10 meV) that can be optically excited and then emissive upon recombining near the band edge [37]–[40]. InSe differs to TMDs by having a direct band gap near the Γ point [38], [41], [42], therefore avoiding spin-valley locking [24]. It has also been predicted that InSe possesses spin-dependent optical selection rules near the Γ point from monolayer to multilayer [41], [42]. These sets of electronic, optical, and magnetic properties imply that InSe has potential for 2D engineering of layered heterostructures while being a distinct electronic and spin landscape from TMDs.

Seminal demonstrations of OISO have been reported in GaSe [43], [44]. However, direct experimental observations of OISO in InSe, a system with higher electron mobility and better

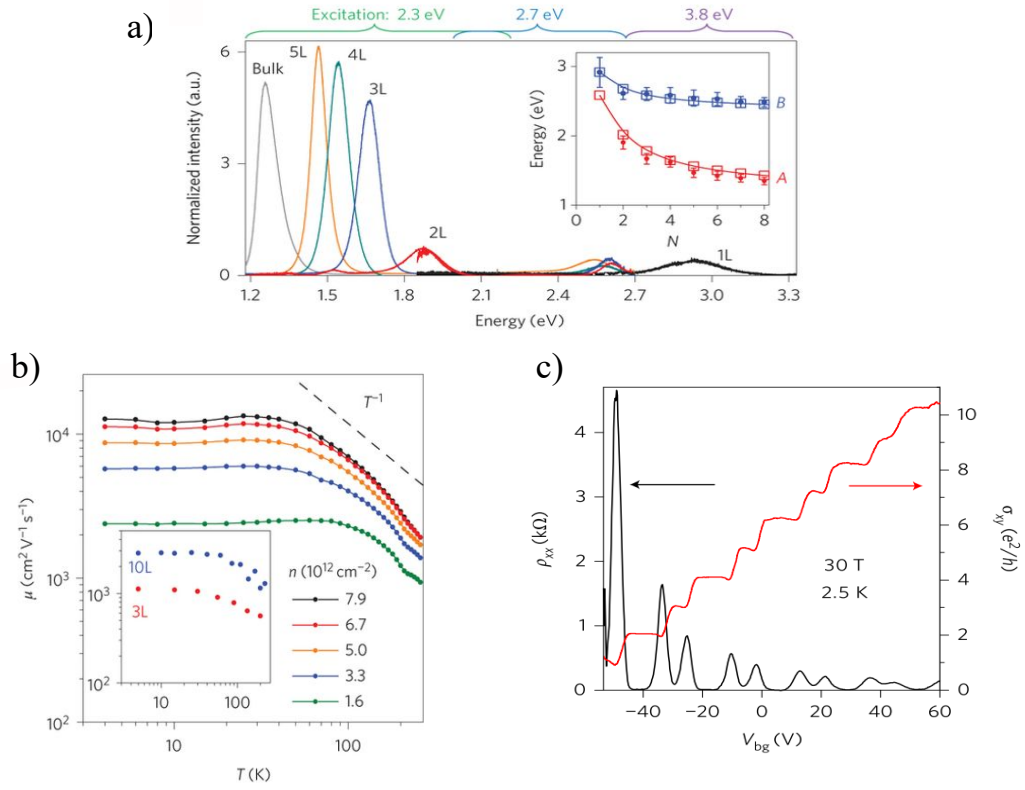

Figure 1.4: a) contains photoluminescence of InSe for different thicknesses. Thinner layers are blue shifted while thicker are red shifted. The inset shows the relationship between layer number and emissions of optical transitions. b) temperature dependence of electron mobility for 6 layer. The inset contains mobility for 3 and 10 layers. c) shows the quantum hall effect. Figures reproduced with permission from Ref. [38].

photodetection on/off ratios [45], [46] than GaSe, has been lacking from the literature. Recently, Nelson *et. al* has shown the first extensive exploration of layer-dependent OISO and excitonic g-factor in InSe [47]. Due to these experimental results, new opportunities have presented themselves for controlling optical spin properties in 2D InSe.

This dissertation reports the author's contribution to the foundational understanding of optical spin properties in InSe, thereby helping assess its potential as a future platform for 2D optical spin-based devices. Ultimately, this work argues that InSe could be a viable candidate for 2D spintronics

and motivates future exploration of not only its individual optical and magnetic properties, but also exploration of layer-by-layer engineering with InSe and 2D magnetic materials, which is largely unexplored experimentally. Future exploration of an InSe and CrI_3 (2D magnet) structure may reveal novel control over optical spin phenomena by layer-by-layer engineering that is distinct from both TMDs or traditional semiconductors.

This thesis is divided into six chapters, five of which succeed this introductory chapter. Chapter two focuses on the theory, experimental techniques, and sample characteristics relevant to optical spin properties of III-VI monochalcogenides. The theoretical work of Ref. [42] is summarized to highlight key predictions for OISO in InSe. Chapter two also gives a short overview of the magneto-optical techniques used to study optical spin properties in semiconductors. Similar techniques have been conducted on passivated InSe in this work. Chapter three presents the work in Ref. [47], which shows decisively that exctionic spins in InSe can be optically oriented. It also investigates the layer-dependent optical spin properties in this system. The discoveries in this work are building blocks for investigations presented in chapters four and five.

Chapter four investigates the emission polarization of a rudimentary few-layer InSe device by tuning a electrostatic gate. This work shows that polarized photoluminescence can be controlled not through excitonic spin relaxation, but by excitonic recombination dynamics. Presenting a means to tune the read-out of spin polarization, which could find applications in optical spin-based devices. Chapter five is an exploration of hole-doped InSe being paired with 2D magnetic materials. This chapter motivates future experimental work that is promising due to predictions of induced ferromagnetism for hole-dope InSe and predictions for optical control of magnetism in a InSe/CrI_3 heterostructure. Basic measurements and proposed experiments are discussed in the later part of this chapter. And finally, Chapter six concludes this thesis. It summarizes key findings and discusses opportunities for future research with 2D InSe.

CHAPTER 2

OPTICAL SPIN PROPERTIES IN III-VI MONOCHALCOGENIDES

Group III-VI monochalcogenides have been studied for decades, however, it is only more recently, after extensive work on novel van der Waals semiconductors, such as TMDs, that the study of monolayer and few-layer thicknesses has been pursued in these systems. Recent discoveries involving these materials' layer-dependent electronic, optical, and magnetic properties have been reported in the literature. These properties show that monochalcogenides are a distinct landscape from TMDs, thus highlighting their potential for future optical, electronic, and spin based devices. This chapter will focus on the optical spin properties in monochalcogenides by first presenting a brief description on band structure and resulting optical spin properties, followed by a detailed description of optical orientation of spin in InSe, and concludes with the discussion of the methodologies and experimental systems that are used throughout the entire dissertation to conduct optical spin studies.

2.1 Band Structure and General Optical Spin Properties

The crystal structure of monolayer MX (M = Ga or In, X = Se, S, Te) is formed by four covalent bonded atoms (X - M - M - X) forming an upper and a lower sublayer that are related by in-plane mirror reflection symmetry. The two sublayers are tightly bound to each other by adjacent metal atoms, thereby creating a buckled honeycomb lattice (Figure 2.1a) [34]. A depiction of the first Brillouin zone can be seen in Figure 2.1c, which shows three different types of zone center states that are equidistant from the origin. These also can be illustrated with a nearly free electron band structure and corresponding symmetry groups in Figure 2.1d [34].

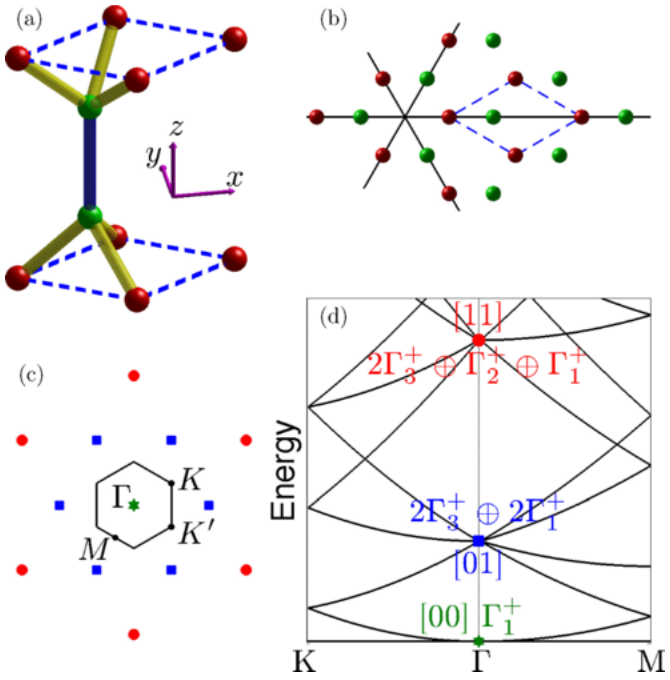

Figure 2.1: a) is a three-dimensional unit cell illustration of III-VI monochalcogenide with metal and chalcogenide atoms and (b) is a two-dimensional illustration of the same unit cell. Reciprocal lattice points and reduced Brilluion zone are shown in (c). (d) shows the nearly-free electron band structure along K-Γ-M with labels of the irreducible representation of Γ point groups, more detail can be found in Ref. [34]. Figure reproduced with permission from Ref. [34].

A first principal band structure study shows band gaps between 2.0 - 3.3 eV for monolayers GaS, GaSe, GaTe, InS, InSe, and InTe (Figure 2.2) [48]. In the monolayer limit, III-VI monochalcogenides tend to have quasi-indirect band gaps since the primary valence band takes on the shape of a caldera. This shape causes the valence band maxima to be slightly off from the Γ point [34], [48]. Further complexity is obtained by considering the perturbation by SOC effects, which has been studied extensively for GaSe and InSe [34], [35], [41], [42]. Atomic SOC causes the splitting of spin states and band mixing [34], [41], [42], while SOC generated by crystal symmetry can lead to additional spin splitting and affects spin relaxation [34], [35], [49].

The complexity of these systems deepens when considering an N (layer number) greater than

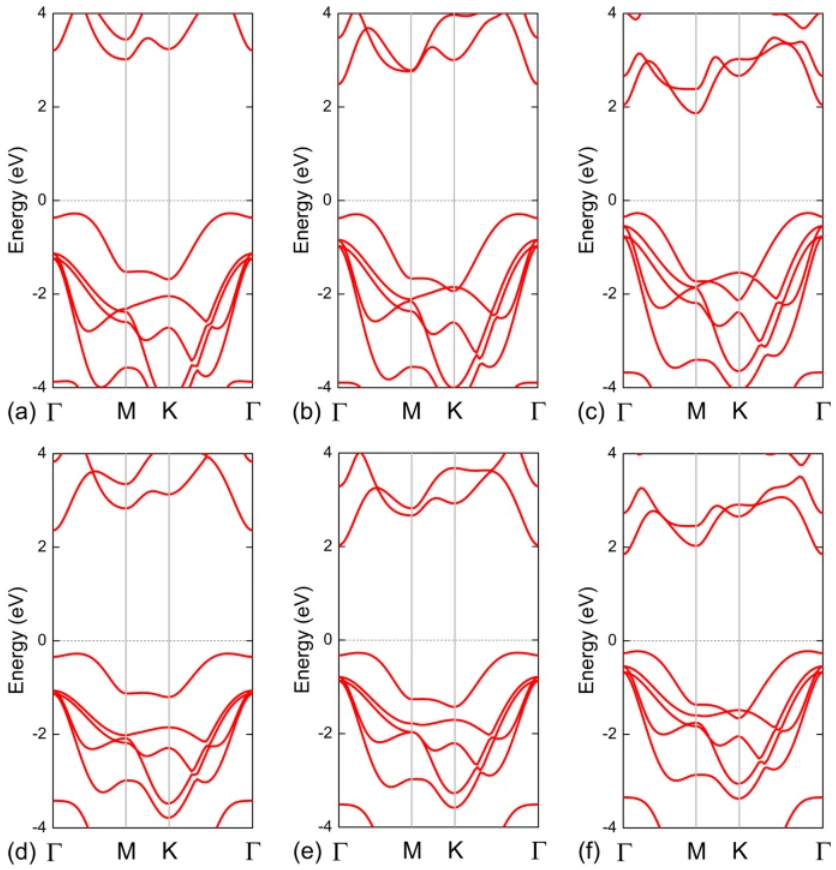

Figure 2.2: Monolayer band structures of GaS (a), GaSe (b), GaTe (c), InS (d), InSe (e) and InTe (f). The dashed line at zero denotes the Fermi level. Figure from open-access article written by Ref. [48].

one. Stacking order of layers and number of layers can modify the band gap [35], [38], [41], [42], change the primary valence band shape [35], [41], [42], induce ferroelectricity [50], [51], and tune spin relaxation [34], [35], [49]. Other effects, such as ferromagnetism are predicted due to extensive hole doping [52]–[55]. Overall, the optical spin phenomena resulting from band structure in III-VI monochalcogenides are interesting and much has yet to be explored in detail. The following section focuses on the theoretical description of spin orientation with light in these materials, particularly in InSe. The presence of strong polarized optical transitions is essential for

optical spin devices, hence the active research on these properties in III-VI materials.

2.2 Theory: Optically-induced Spin Orientation

Polarized optical selection rules in semiconductors have been well studied for traditional semiconductors [5] and TMDS [56]. In addition, a few experimental [43], [44] and theoretical [34], [57] studies have been conducted on OISO in GaSe. However, because these past works have focused on OISO in either just monolayer (theory) [34], crystals (experiment and theory) [43], [57], or nanoslabs (experiment) [44], they lack an in-depth exploration of the layer dependence. Furthermore, the electron mobility of GaSe is four orders of magnitude smaller than the electron mobility in InSe [45]. These factors then motivate the study of OISO in monolayer and few-layer InSe.

2.2.1 Nearly-free Electron Toy Model

Focusing on a simple band description of monolayer InSe, there are 6 bands (no SOC) near the Γ point that can be examined for optical transitions (Figure 2.3 left). The primary optical transition is dictated by wave functions that are nominally a s-symmetry conduction band (c) and p_z orbital top valence band (v), which have been calculated to have no significant coupling between spin and out-of-plane linearly polarized optical fields (A line transition) [42]. Orbitals with p_x and p_y symmetry make up two-fold degenerate lower valence bands (v_1 and v_2). The v_1 band has a non-polarized optical transition coupled with in-plane circularly-polarized optical fields (B line transition) [42]. However, atomic SOC disturbs this simple description (Figure 2.3 right) by breaking the degeneracy of v_1 and v_2, thus creating total angular momentum states of $J_z = \pm\frac{3}{2}$ and $J_z = \pm\frac{1}{2}$. The v_1 band with $J_z = \pm\frac{1}{2}$ then mixes with v, thereby allowing spin-polarized B line transitions by free carriers near the band gap. There is no significant mixing between v_2 and c, and band mixing does not occur between c and v_1 or between v and v_2 [42].

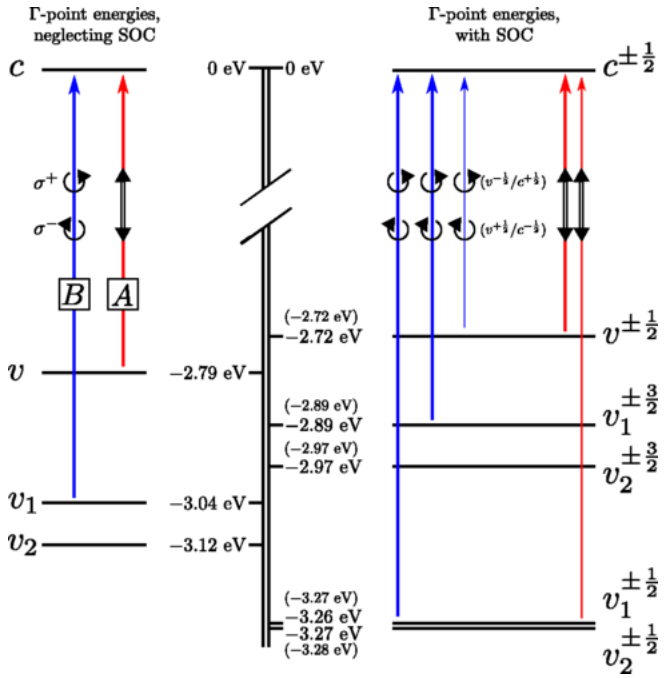

Figure 2.3: Left depicts optical transitions near the Γ point without SOC. The lower valence bands are each two-fold degenerate, thus giving a total of 6 bands in this model. The right depicts polarized optical transitions due to the inclusion of SOC which breaks the degeneracy of the lower valence bands. This system has a total of 12 bands. Figure reproduced with permission from Ref. [42].

In order to capture these optical transitions in a fully parameterized theoretical framework, Ref. [42] constructed a $\boldsymbol{k}\cdot\boldsymbol{p}$ perturbation theory Hamiltonian for monolayer InSe, which includes the basis of atomic orbitals with off-diagonal couplings arising from momentum matrix elements and SOC. Therefore a 12-band model can be written as [42]

$$\hat{H} = \begin{pmatrix} H_c I_s & \epsilon_z d_z I_s & \frac{e\beta_1}{cm_e} I_s \otimes \boldsymbol{A} & \lambda_{c,v_2}\hat{\boldsymbol{s}} \\ \epsilon_z d_z I_s & H_v I_s & \lambda_{v,v_1}\hat{\boldsymbol{s}} & \frac{e\beta_2}{cm_e} I_s \otimes \boldsymbol{A} \\ \frac{e\beta_1}{cm_e} I_s \otimes \boldsymbol{A^T} & \lambda_{v,v_1}\hat{\boldsymbol{s}^T} & I_s \otimes \boldsymbol{H}_{v_1} + \lambda_{v_1} s_z \otimes \sigma_y & 0 \\ \lambda_{c,v_2}\hat{\boldsymbol{s}^T} & \frac{e\beta_2}{cm_e} I_s \otimes \boldsymbol{A} & 0 & I_s \otimes \boldsymbol{H}_{v_2} + \lambda_{v_2} s_z \otimes \sigma_y \end{pmatrix} \tag{2.1}$$

ϵ_z is the electric field of the incoming photon, d_z is the out-of-plane dipole moment, e is the charge of electron, m_e is the mass of an electron, c is the speed of light, $\beta_{1(2)}$ is the magnitude of the interband matrix element of the moment operator, the $\lambda_{v_{1(2)}}$ are intraband SOC constants for band $v_{1(2)}$, and $\boldsymbol{A} = (A_x, A_y)$ is the vector potential of polarized light. I_s is the identity matrix in spin space and $s_{x,y,z}$ are spin operators. $\hat{\boldsymbol{s}} = (s_x, s_y)$ ($\hat{\boldsymbol{s}}^{\boldsymbol{T}}$ is the transpose) is the abbreviated spin vector which allows for the compact form shown in eq. 2.1. The eigenvalues of the matrix are the energies of the respective bands as a function of $\boldsymbol{k}$, the electron wave vector measured from the Γ point [41], [42]. The lowest energy conduction band with s-symmetry is described by,

$$H_c \approx \hbar^2 k^2 / 2m_c \tag{2.2}$$

while the highest valence energy band with p_z-symmetry is described by,

$$H_v(K) \approx E_v + E_2 k^2 + E_4 k^4 \tag{2.3}$$

The parameters E_2 and E_4 help describe the shape of the primary valence band [41]. The valence bands $v_{1(2)}$, which represent the orbitals with $p_{x(y)}$ symmetry, can be described as

$$H_{v_{1(2)}} \approx \left[E_{v_{1(2)}} + \frac{\hbar^2 k^2}{2m_{1(2)}} \right] I_\sigma + \frac{\hbar^2 (k_x^2 - k_y^2)}{2m'_{1(2)}} \sigma_z + \frac{2\hbar^2 k_x k_y}{2m'_{1(2)}} \sigma_x \tag{2.4}$$

I_σ is an identity matrix and $\sigma_{x,y,z}$ are the Pauli matrices.

The parameters in this model are extracted from density functional theory (DFT) by fitting eq. 2.1. This fitted model then can be used to evaluate optical oscillator strength for a transition by calculating the absorption coefficient. For monolayer, the A line transition has an absorption coefficient of 1.5% while the B line transitions has an absorption coefficient of 10% [42].

To examine the the layer dependence of these optical transitions, the monolayer Hamiltonian of eq. 2.1 can be "stacked" using a hopping model to give a multilayer Hamiltonian [42],

$$\hat{H}^N = \sum_{n}^{N} \sum_{\alpha,\alpha',\mu,\mu'} \hat{H}_{\alpha\mu,\alpha'\mu'} a^{\dagger}_{n\alpha\mu} a_{n\alpha'\mu'} + \sum_{n}^{N-1} \sum_{\alpha,\mu} \delta_{\alpha} (a^{\dagger}_{n\alpha\mu} a_{n\alpha\mu} + a^{\dagger}_{(n+1)\alpha\mu} a_{(n+1)\alpha\mu}) \\ + \sum_{n}^{N-1} \sum_{\mu} [t_c a^{\dagger}_{(n+1)c\mu} a_{nc\mu} + t_v a^{\dagger}_{(n+1)v\mu} a_{(nv\mu} + t_{cv} (a^{\dagger}_{(n+1)v\mu} a_{nc\mu} - a^{\dagger}_{(n+1)c\mu} a_{nv\mu}) + H.c] \tag{2.5}$$

where N is the number of layers, n the index of a N-layer crystal, α is a band, and μ is spin state

Table 2.1: Calculated band gaps ($\hbar\omega$) and absorption coefficients for A line (g_A) and B line (g_B) transitions for different thicknesses. This table was modified and reproduced with permission from Ref. [42].

N	$\hbar\omega$ (eV)	g_A (%)	g_B (%)
1	2.72	1.5	10.3
2	2.00	0.5	8.3
3	1.67	0.3	8.8
4	1.50	0.3	9.0
5	1.40	0.3	9.1

($\pm\frac{1}{2}$). $a^{(\dagger)}_{n\alpha\mu}$ is the annihilation (creation) operator for electrons denoted with indexes for a specific layer, band, and spin state. The matrix elements of the Hamiltonian ($\hat{H}_{\alpha\mu\alpha'\mu'}$) in eq. 2.1 are also indexed in eq. 2.5. The parameters t_c, t_v, t_{cv} are interlayer hoppings, while δ_v and δ_c are on-site energy shifts due to interlayer potentials. Using this model, Ref. [42] roughly calculated absorption coefficients for different layers which can be seen in Table 2.1.

2.2.2 Polarized Light Coupling to Excitonic Spin

The theoretical framework by Ref. [42] models the properties of a nearly-free electron, yet there is ample evidence that the photoluminescence of III-VI monochalcogenides is dominated by excitons.

In fact, in studies of OISO in GaSe, this is explicitly recognized and understood [43], [44], [57]. In InSe, it has been shown that exciton binding energies are relatively large ($\sim$ 10 meV) [39], [40], excitons have long emissive lifetimes ($\sim$ 1 ns) [39], and transition selection rules contribute to band edge excitons [58], [59]. Thus, the more complete narrative of OISO in InSe contains the

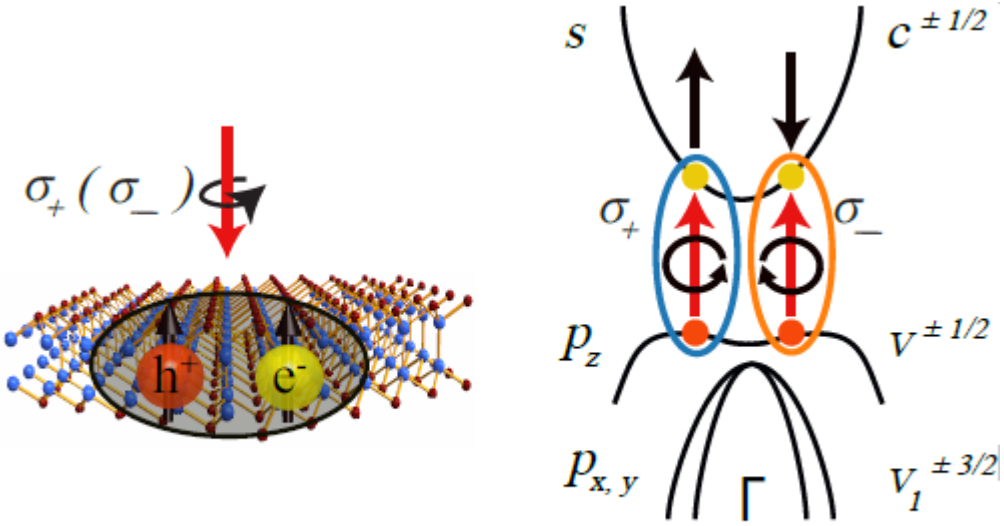

Figure 2.4: Illustration of a monolayer InSe crystal (left) and monolayer InSe band diagram (right). Monolayer and few-layer InSe have been predicted to have polarization dependent optical selection rules. These thicknesses have also been shown to have strong excitonic binding energies. Excitons would then likely effect any investigations into optical spin properties of InSe. Figure reproduced with permission from Ref. [47].

coupling of polarized light to excitonic spin (Figure 2.4). Thus, when implementing the toy model for InSe [42], optical spin properties of both electron and holes must be taken into account.

2.3 Magneto-optical Techniques to Study Optical Spin Dynamics in Semiconductors

In vacuum, light is not susceptible to a magnetic stimuli. Yet, in 1846, Michael Faraday published his observation of linearly polarized light rotating as it propagated through medium with a parallel

magnetic field [60]. In 1923, Robert W. Wood and Alexander Ellett published observations on luminescence depolarization for Mercury atoms in a transverse magnetic field [61]. The former would be called the Faraday effect and the latter the Hanle effect (it is named after W. Hanle because he is credited with giving a good explanation for the observation) [62].

Building off of these previous studies and work done by Alfred Kastler, who helped formalize the basic principle of optically-induced spin polarization in gases [63], in the late 1960s, R.R Parson demonstrated optically-induced spin orientation in GaSb, a III-V semiconductor [64]. This was done by using a very simple measurement, pumping with circular polarized light and measuring the circular luminescence. In 1971, another seminal work by Claudine Hermann and Georeges Lampel measured spin precession of an electron in GaSb using polarized light and magnetic fields. These two initial studies on GaSb galvanized the field of optical orientation, or OISO, in semiconductors.

When considering some of the key works of the past $\sim$200 years, it is clear that there is long history of using polarized light to examine the magneto-optical properties of different systems. In particular, in the last several decades, these principles have been applied to semiconductors as a means to orient, precess, inject, and detect spin in these systems. By harnessing the power of light, magneto-optical techniques can be used to study and control optical spin properties in low-dimensional systems like InSe.

2.3.1 Steady State Measurements

Perhaps, the simplest and most efficient way of studying OISO in semiconductors is steady-state polarized photoluminescence (PL) measurements. Typically, this is preformed by using a continuous wave (cw), in-plane circularly polarized light source that has a photon energy close to energy separation of a band gap. This will create a net non-equilibrium spin orientation in a semiconduct-

ing system with appropriate spin polarized optical transitions. As the system relaxes, there will be a preferential spin direction which will manifests as an intensity difference between the two circularly helicities ($I_{+(-)}$) in the PL. Allowing a direct read-out of spin polarization by calculating the degree of circular polarization, $P = (I_+ - I_-)/(I_+ + I_-)$. The steady-state rate equation that describes the P for a semiconductor is [5]

$$P = \frac{P_0}{1 + \tau_r/\tau_s}, \tag{2.6}$$

where P_0 is the degree of circular polarization at the time of excitation. And τ_r and τ_s, are the recombination and spin lifetimes respectively [5]. This polarization can be furthered studied in a magnetic field. In fact, for fields applied out-of-plane with respect to the sample, the Zeeman effect will split spin levels. This leads to an imbalance in read-out polarization, even with linearly polarized light, a result that can used to investigate how well a magnetic field couples to the spins of carriers in a material [5].

Note, the ratio of recombination lifetime to spin lifetimes dictates the ability to observe optical orientation in a semiconducting system. As the ratio increases, the amount of P decreases. Therein lies the limitation of this measurement, if $\tau_s \ll \tau_r$, this measurement method becomes ill-suited for studying optical spin properties in a semiconducting system.

2.3.2 Time-resolved Measurements

Time-resolve studies using pulsed lasers can circumvent the limitations of steady-state measurements by allowing a direct measurement of carrier dynamics in a system. Time-resolved photoluminescence (TRPL) and transient reflection (TR) are two time-resolved methods that are commonly employed to probe carrier recombination dynamics in semiconductors. The first requires a

pulsed laser and electronics that sync, in time, the incident pulse to observed decay of PL, while the second requires two pulsed beams, a pump and probe, where the change in the probe intensity, with time delay between the two beams, gives information on carrier lifetimes.

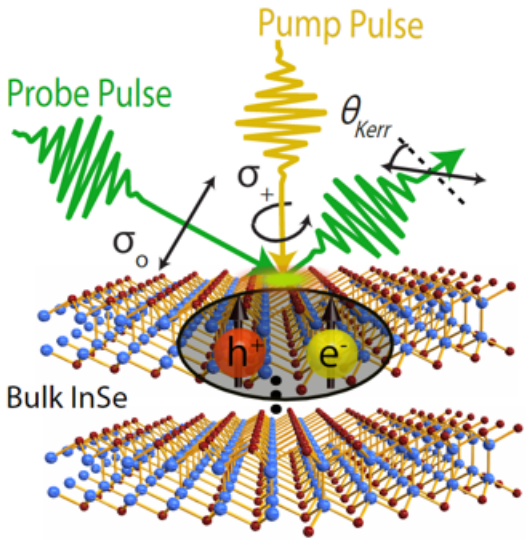

Figure 2.5: Illustration of time-resolved Kerr rotation on bulk InSe. The yellow light pulse is the pump pulse, which is circularly polarized, and the green light pulse is the probe pulse, which is linearly polarized. These two pulses are separated in time, therefore allowing the extraction of time dynamics for a spin system through the rotation of the linearly polarized probe. Reproduced with permission of Ref. [47].

Now, in order to study spin dynamics, polarized TRPL requires a similar setup (Chapter 2.5) to a stead-state polarized PL measurement, while a spin-sensitive pump-probe method requires a different setup than TR (also in Chapter 2.5). One of the most sensitive methods to measure spin dynamics in semiconductors is time-resolved Kerr rotation (TRKR). An illustration of this techniques is shown in Figure 2.5. A circularly polarized pulse optically pumps a non-equilibrium spin imbalance (yellow). As the spin population relaxes to equilibrium, a linearly polarized probe pulse (green), with a time delay relative to the pump, monitors the relaxation through the Kerr rotation angle θ_{K} of its linear polarization axis. Kerr rotation is similar to Faraday rotation. The

difference between the two lies in whether the probing beam is reflected (Kerr) or transmitted (Faraday). TRKR has been used to study spin properties in III-V semiconductors [65]–[68] and TMDs [24], [69]–[72], thus is an effective tool for magneto-optical studies.

2.4 InSe Sample Preparation and Polytype Characterization

An exfoliated few-layer InSe sample is very air sensitive because Se defects on the surface react with oxygen and water. This can lead to local deformations and a cascading effect that causes a rapid oxidization of the surface [73]. This process is believed to occur in three steps (Figure 2.6 right): (I) oxygen binding to a defect in the lattice, (II) oxygen dissociates form the lattice leaving a dangling bond, and (III) the dissociated oxygen can interact with water in the atmosphere [74]. This process is accelerated when InSe is exposed to intense light in ambient conditions [73], [74]. Therefore, InSe sample preparation requires an inert environment such as a N_2 glovebox. As an example of how quickly this decay can occur, Figure 2.6 (left) shows photoluminescence decay of 5-layer (5L) InSe under three different conditions (ambient, vacuum at room temperature, and vacuum at low temperature). InSe's emission decays rapidly in ambient while degradation is much slower for the other two environmental conditions. The surface sensitivity of InSe motivates taking steps to reduce the oxidation rate, which in turn would stabilize the optical properties of thin samples.

To protect thin InSe from degradation, a common technique is used, dry encapsulation [75]. This method uses 2D materials such as hexagonal Born Nitride (hBN) [38] or Gr [76] as top and bottom layers to keep air and moisture out. Other viable methods to protect InSe from decaying have been demonstrated by the Hersam group at Northwestern University. Examples include, surfacant-free, low boiling point, deoxygenated cosolvent system for optoelectronic device processing [77] and aluminium encapsulation using atomic layer deposition [78]. Due to their exper-

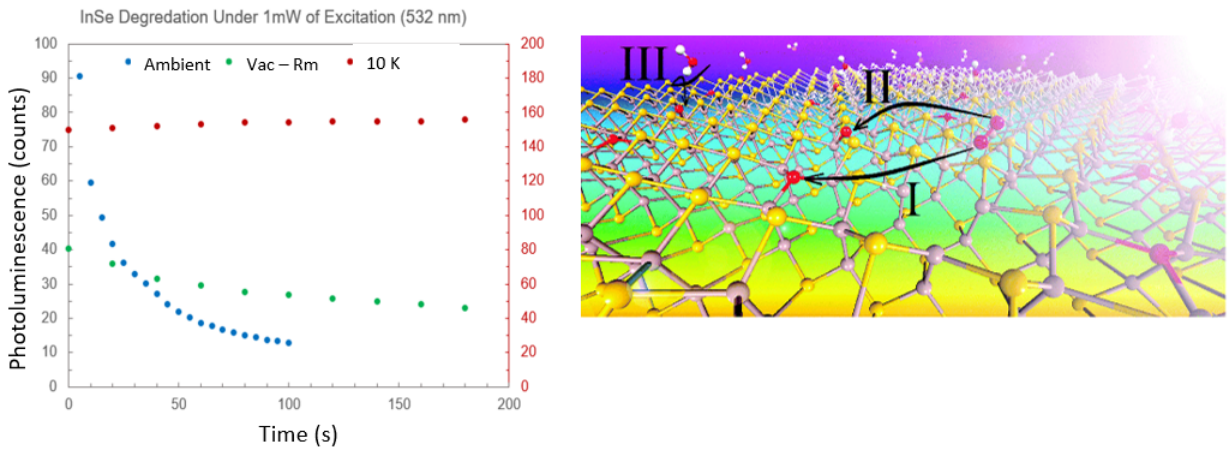

Figure 2.6: Left image shows photoluminescence decay over time for few-layer InSe under 532 nm, 1 mW excitation light source. Blue is in air, green is in vacuum, and red is in vacuum at 10 K. The right image illustrates the three chemical processes that lead to rapid degradation of InSe under light illumination: (I) oxidation, (II) dissociation, and (III) interaction with water. The right image is reproduced with the permission of Ref [74].

tise in InSe sample preparation, the Hersam group fabricated the viable thin samples and devices measured in work presented in later chapters. In this dissertation, thin InSe samples were dry encapsulated with hBN, and for gated devices (Chapter 4.2 and Chapter 5.3), Gr was also included to improve electrical contact between the sample and gold contacts.

Another important characteristic of InSe that must be considered, is polytism. As mentioned before (Chapter 2.1), stacking order of III-VI monochalcogenides can induce a number of novel effects such as ferroelectricity [50], [51] and spin splitting [35]. Since common polytpes (ϵ, γ, β) are very similar in structure, distinguishing a particular stacking order can be difficult. In order to identify polytypes, multiple experimental methods are typically required, such as Raman spectroscopy [79]–[84] and second harmonic generation (SHG) [79], [80].

Figure 2.7 shows SHG and Raman (inset) measurements of different InSe thicknesses. Because SHG is a non-linear process, it occurs in non-centorsymmetric systems. Observing this effect in

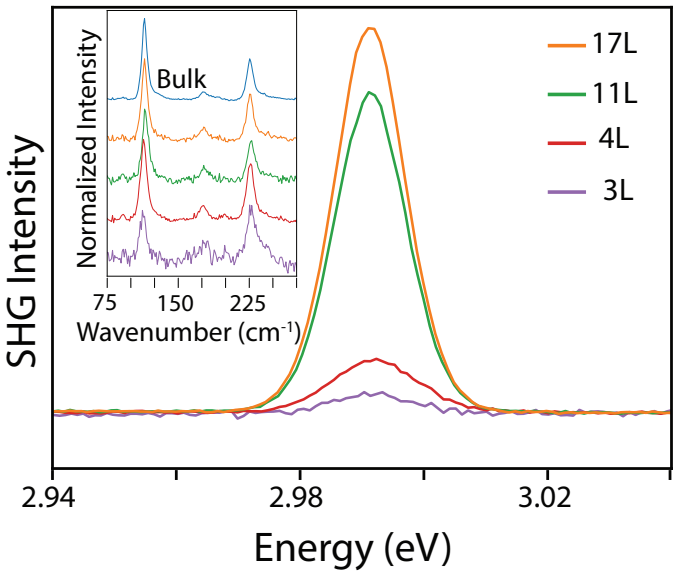

Figure 2.7: InSe of odd and even layer numbers show SHG. A pulsed laser centered at 1.49 eV (830 nm) was used to generate the SHG signal. The inset shows Raman for different thicknesses (3L to Bulk).

odd and even thicknesses provides evidence that spin splitting, due to crystal symmetry, will occur for any layer number (discussed further in Chapter 3). By comparing SHG and Raman to the literature [79]–[84], it has been determined that samples measured were ϵ-InSe.

2.5 Implemented Magneto-optical Techniques to Study Optical Spin Dynamics in InSe

In work presented in this thesis, steady-state PL, steady-state polarized PL, TRPL, polarized TRPL, TR, and TRKR were the main methodologies used to investigate carrier dynamics in InSe. A combination of these techniques were used in chapters three through five. With these tools, it is possible to obtain a wealth of information about InSe systems in order to better understand their fundamental optical spin properties. The experimental apparatuses that employ at least one of these optical measurement can be seen in the Figure 2.8. All measurements were done at low temperature in magneto-optical cryostats with high magnetic fields.

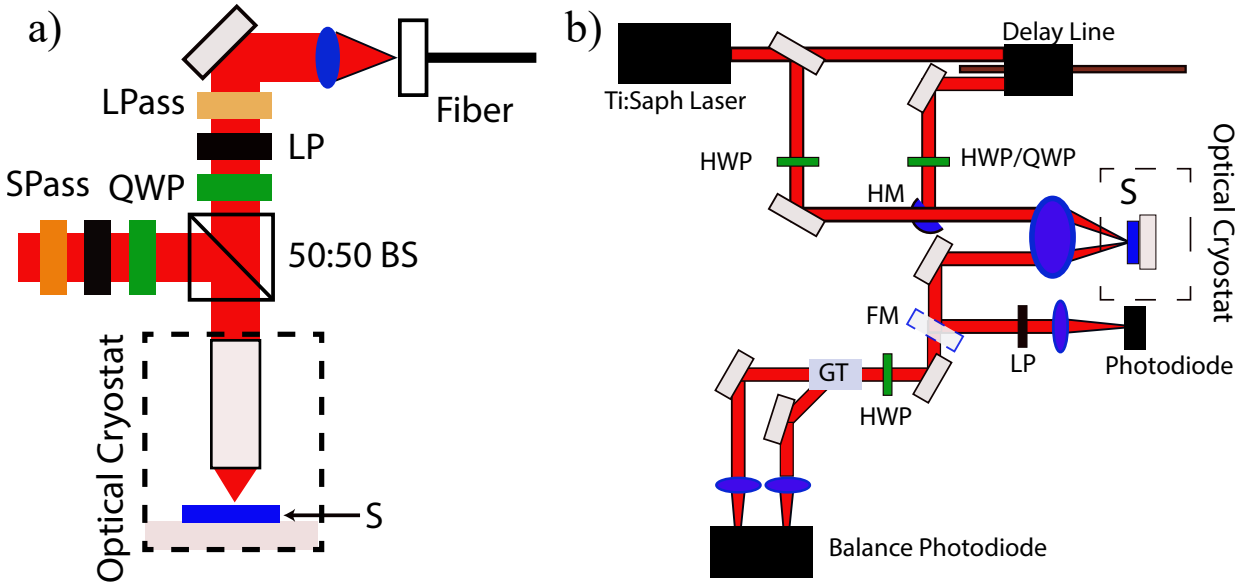

Figure 2.8: a) is the polarized PL setup. A shortpass (SPass) and longpass (LPass) are put on the input and output, respectively, to reduce pump laser noise. On the collection side, the fiber can lead to a spectrometer or single photon counter. The pump-probe time-resolved setup b) has a FM (flip mirror) that can be used to switch between TR (photodiode) and TRKR (balanced photodiode) measurements. S is shorthand for sample.

The general optics setup for the polarized PL can be seen in Figure 2.8a. On the input, there is a shortpass filter (SPass), a linear polarizer (LP), and a quarter-wave plate (QWP). A circular or linear polarized beam then passes through a 50:50 beamsplitter (BS), where 50% is directed into an objective inside of an attoDRY2100 magneto-optical cryostat (1.7 K base temperature, 9 T superconducting magenet). The beam reflected from the sample (S) then passes through circular polarized collection optics (a QWP and LP) and is filtered with a longpass filter (LPass) before being focused onto a fiber that leads to a 750 mm spectrometer with a CCD camera (Andor). A tunable cw light source was used for optical excitation (Chapter 3).

All time-resolved measurements were done in the beta version of Quantum Design's OptiCool (Figure 2.9). This system has a temperature range of 1.5 - 350 K and a magnetic field that reaches 7 T. For optical access, there are seven side windows and one top window. The sample stage is 6 cm

in radius while the space between the inner edges of the superconducting magnet is 9 cm, which gives ample room for custom pieces (Figure 2.9c). The characteristics of this system allow for a variety of magneto-optical experimental configurations. Therefore, pump-probe measurements and TRPL measurements were conducted using this versatile system. A tunable 76 MHz Ti:Sapphire laser (700 - 980 nm) was used for all time-resolved measurements, either as the main laser source or as a pump for a tunable Optical Parametric Oscillator (OPO), a visible (580 - 700 nm) pulsed laser cavity (used in work shown in Chapter 5.3).

When conducting TRPL or polarized TRPL measurements, a similar setup to the steady-state polarized PL measurement (Figure 2.8a) was used in the OptiCool. Using the low-working distance top window option from Quantum Design (Figure 2.9b), a 100X long-working distance objective could be used to achieve spot sizes of about ~ 4 μm. For TRPL measurements, the QWPs for both input and collection were set so that light passing through them would be linear. Instead of collecting light into a fiber that lead to a spectrometer, light was collected through a fiber that lead to a Micro Photon Devices (MPD) single photon counter. This was connected to a time-correlated single photon counting module, HydraHarp 400, which was fed the repetition rate of Ti:Sapphire laser (76 MHz) in order to trigger photon counts for time-resolved measurements.

For the pump-probe time-resolved measurements scheme (Figure 2.8b), a 50:50 plate beam-splitter is used to create a pump arm and a probe arm. The time separation between pump and probe beam is controlled by a mechanical delay line. A wave plate is used to adjust polarization of the pump before incident on a half mirror (HM). The HM allows the pump to be aligned parallel to the probe beam but spatially separated by 1-inch. The distance from the outside window of the OptiCool cryostat to the center is roughly $\sim$15 cm. A two inch lens with focal length of 15 cm is used to focus the beams onto a sample which is about 3 - 4 cm from the center of the cryostat. The field here deviates less than 1% from the set value. In this Voigt geometry, pump and probe

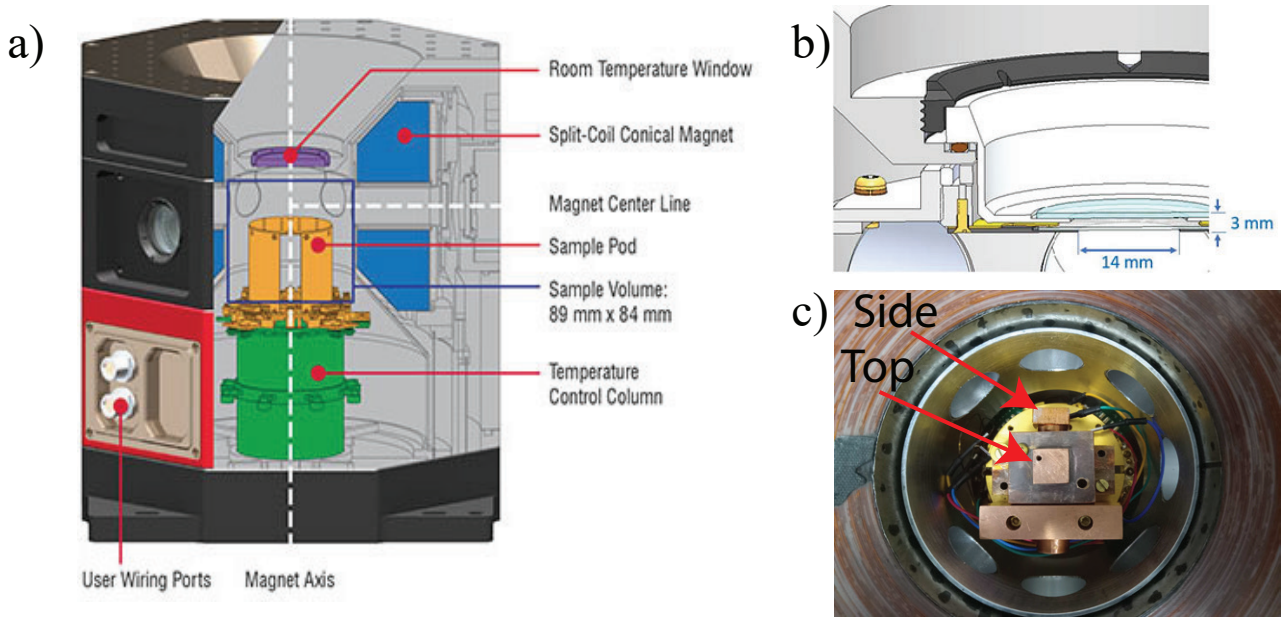

Figure 2.9: Quantum Design's OptiCool has several features useful for variety of experiments a) and also has additional add-ons such as the low-working distance window b). This window can be used to replace the standard top window. Customized parts for side window access and top window access can be seen in c). This also allows for samples to be measured perpendicular (side mount) or in parallel (top mount) with the magnetic field (7 T).

beams have typical beam sizes of 65 μm and 30 μm, respectively. Therefore samples with lateral dimensions of at least 60 μm by 60 μm allow for optimal signal.

After the beams are reflected off the sample, they can be directed to a single photodiode or balanced phototdiodes using a flip mounted mirror (FM). The single photodiode is used for TR, while the balanced photodiodes are used for TRKR. For TR, a half-wave plate (HWP) is used to cross-polarize the pump with respect to the probe. Upon collection, a linear polarizer (LP) is oriented to filter out any pump scatter before the remaining light enters the single photodiode. For TRKR, a QWP is used to set the pump to one of the circular helicities. After reflection, the FM is flipped down and the beams travel through a HWP and Glan-Thompson (GT) polarizer. For both measurement techniques, the pump is chopped at 100 kHz while the probe is demodulated with a

lockin amplifier. To reduce noise in TRKR measurement, the probe is also chopped at 1 kHz and the 100 kHz demodulation goes into a second demodulator at 1 kHz to filter out unintended signal from pump scatter.

CHAPTER 3
LAYER-DEPENDENT OPTICALLY-INDUCED SPIN POLARIZATION IN INDIUM SELENIDE

Even with OISO measurements of GaSe and predictions of OISO in InSe, direct observation of light coupling to spin in InSe is lacking in the literature. Recently, Nelson *et. al* conducted a comprehensive study on layer dependence of OISO in InSe and have extracted key physical properties such as the magnetic moment [47]. This chapter focuses on these studies. This work was possible due to the combined efforts of the Stern group (low temperature magneto-optical experiments), the Hersam group (fabrication and materials), and Argonne National Lab scientists (materials computational theory). The results presented in this chapter are used as foundational pieces in which future chapters build on.

3.1 Experiment: Optically-induced Spin Orientation in Indium Selenide

Figure 3.1b illustrates a simple picture of three mechanisms that can be observed in steady-state polarized PL for a semiconducting system with two excitable spin states in the primary conduction band. In the absence of a magnetic field, linearly polarized light (σ_o) can excite a carrier population. As this population relaxes, each carrier has an equal chance of settling in either spin state, as these states are degenerate in energy. This leads to no net spin imbalance (No Polz) and manifests as equal amounts of circularly polarized emission ($\sigma_{+(-)}$). When a magnetic field is applied, the spin levels are split due to the Zeeman effect, causing the spin levels to be separated in energy (Zeeman). When this occurs, more carriers will relax into the lower energy spin state. This creates a difference in intensity between emitted PL of opposite circular helicity. However, neither of these

two situation show orientation of spin being driven by the coupling between polarized light and spin. If a net spin imbalance is created by incident circular polarized light when no magnetic field is present, and the difference in intensity between circular emissions can be observed after initial fast relaxation, then spins are being preferentially oriented into one spin state. In this third case (OISO), the circularly polarized light would be the only cause of the observed spin imbalance. Thus, it would provide definitive proof of OISO existing in a system.

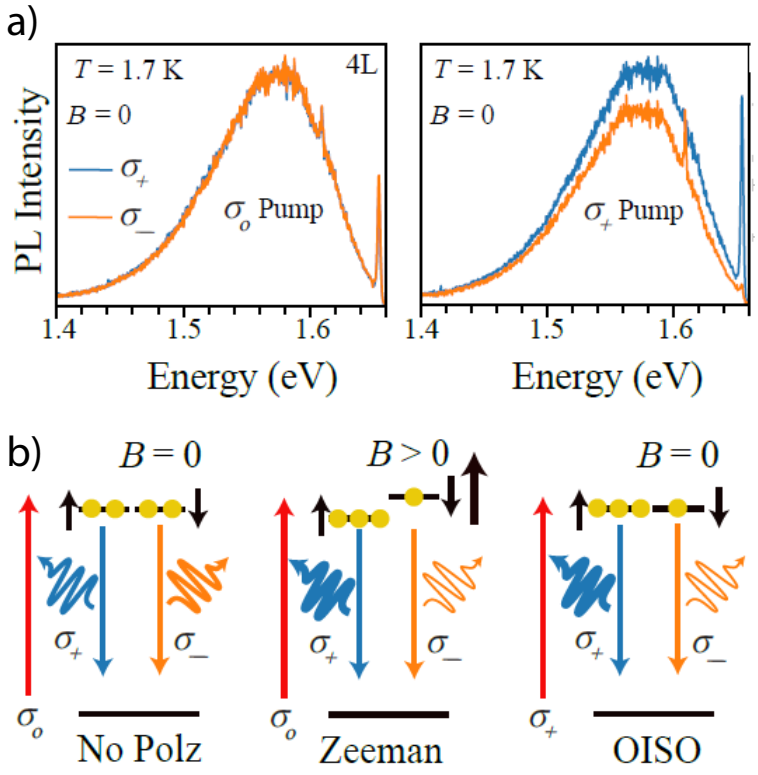

Figure 3.1: a) measured intensity of polarized PL for a linear pump (left) and circular pump (right) at low-temperature without a magnetic field for a 4L InSe flake. The sharp peaks are residuals, after filtering, of the pump laser at 1.67 eV. b) illustrates three mechanisms that describe potential measured outcomes in a steady-state polarized PL measurement. Figure reproduced with permission from Ref. [47].

In Figure 3.1a, experimental verification of polarized-dependent optical selection rules for the

primary band gap in InSe are shown for 4L. Without a magnetic field and a linearly polarized pump, there is no difference in emitted intensity (No Polz). Yet, when the incident light is circularly polarized (σ_+), there is a clear difference in intensity between both emitted helicities (OISO). This is direct experimental observation of OISO in few-layer InSe.

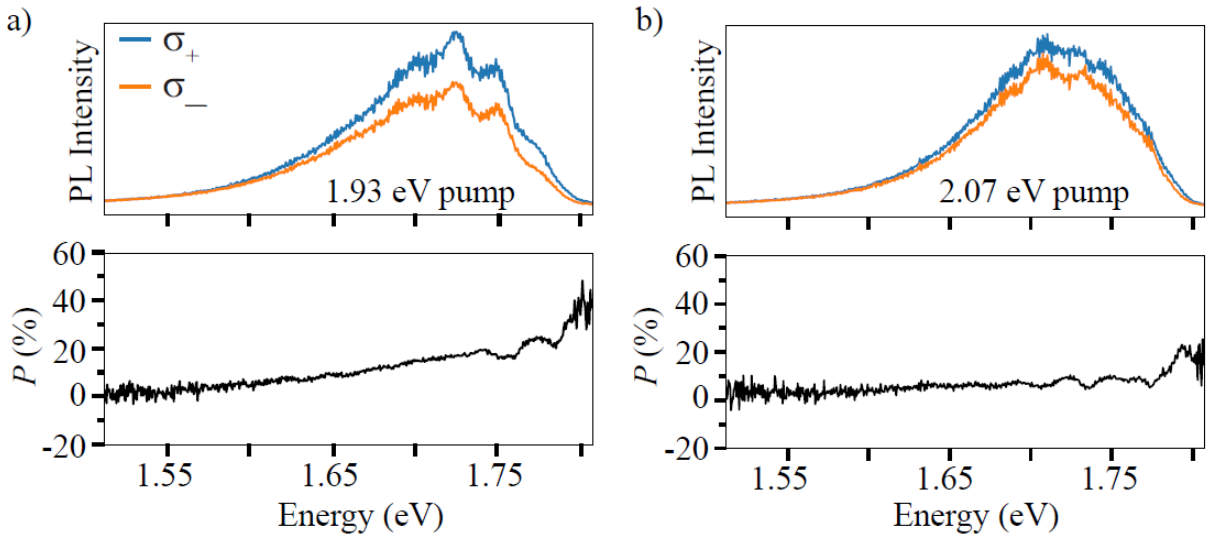

Figure 3.2: Plots of polarization (P) vs PL emission energy is shown for pump excitation 1.93 eV a) and 2.07 eV b). Below each of the PL plots, a plot that tracks polarization as a function of emission energy is shown. These are measurements are taken on a 3L InSe flake.

Note, steady-state polarized PL reveals a energy dependence of the polarization (P) for the PL spectrum (Figure 3.2a and 3.2b), with a reduced polarization at the low-energy tail. The cause of this spectral dependence for polarized PL is not well understood. One possible origin for this change in P with PL photon energy, is the caldera shape of the valence band in InSe. It is predicted that few-layer III-VI monochalcogenidess can have $\sim$ 10 - 100 meV separation between the primary valence band minimum (Γ point) and maximum (slightly off from Γ point) [85]. Angle-resolved photoemission spectroscopy (ARPES) experiments have shown that for monolayer and bilayer InSe, grown by molecular beam epitaxy, the valence band maximum and minimum have an energy separation of $\sim$ 100 meV [86]. This is on the same order of magnitude as the width of

the PL (Figure 3.1, 3.2a, and 3.2b) suggesting that the reduced polarization in the low-energy tail could be due to scattering in the valence band. More investigation is needed to make any stronger claims and beyond the scope of the thesis.

3.2 Layer-Dependent Spin Relaxation

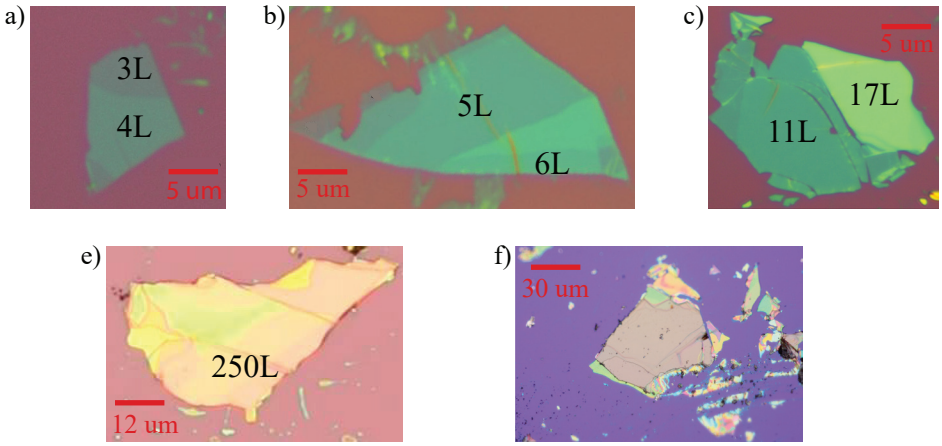

Figure 3.3: Images of unencapsulated InSe flakes for clarity. a) - e), measured using the polarized PL measurement schemes while f) was measured using TRKR and TR.

To further explore OISO in InSe, steady-state polarized PL measurements were conducted for different thickness ranging from 3L to bulk (Figure 3.3). Exfoliated InSe flakes less than 20L were encapsulated in hBN to protect them from degradation in air (mentioned in Chapter 2.4). Because InSe has a layer-dependent band gap (inset of Figure 3.5) a tunable cw laser was used to conduct near-resonance polarized PL measurements. The energy of the pump laser was less than 200 meV from resonance, much less than spacing between valence bands. This allows for the pumping of only the lowest energy exciton (primary band gap). When pump laser energy is increased far from

the resonance of the lowest energy exciton ($>$ 200 meV), the spin polarized emission decreases for few-layer InSe (Figure 3.4). This may be due to increased scattering of hot spin carriers [87].

In Figure 3.5a, the calculated degree of polarization, P, is calculated using $P = (I_+ - I_-)/(I_+ + I_-)$. The intensity for each helicity is integrated over the PL spectrum for different layer numbers ranging from 3L to 250L. As layer number increases, the amount of P decreases. By examining the roles in which P_o, τ_r, and τ_s play in eq. 2.6, it is possible to understand qualitatively the trend (P_{SOC}) in Figure 3.5a.

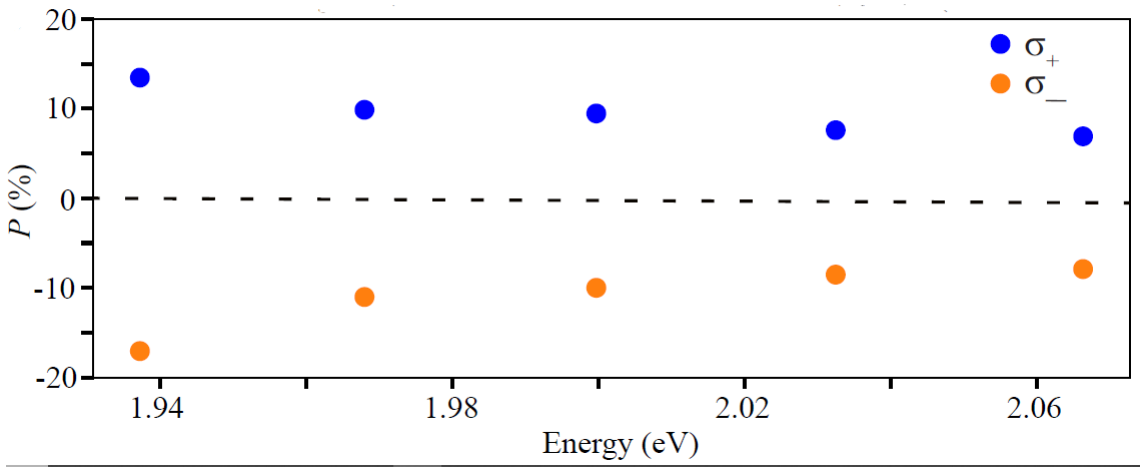

Figure 3.4: P vs Photon energy for 3L. As pump energy moves further away from resonance, P decreases. This is likely due to the lost of spin polarization as hot electrons scatter [87].

As InSe becomes thinner, the primary valence band becomes more caldera-like. Even so, this does not seem to impact polarized-dependent optical transitions near-Γ (look at B line transitions in Table 2.1). Thus, it can be assumed that P_o is constant with thickness, as the initial excitation is most likely not dependent on layer number. By conducting TRPL on 3L InSe and TR on bulk InSe, a τ_r on the order of $\sim$1 ns has been shown for both thicknesses (Figure 3.6). This is further corroborated by recombination lifetime measurements found in the literature [39], [44]. These results show that recombination lifetime does not have much layer-dependence. This then points

to the last parameter in this model, τ_s, as being the driver for the observed change in optical spin polarization.

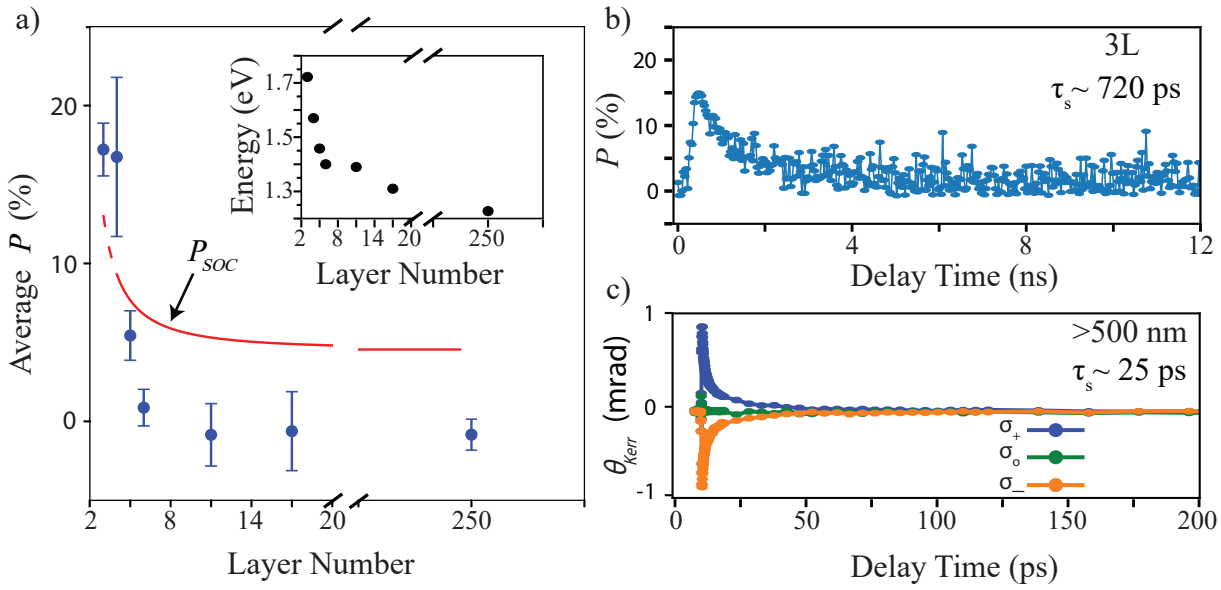

Figure 3.5: a) Average P was calculated for different thicknesses of InSe. The inset shows PL peak intensity for different thicknesses. b) and c) show polarized TRPL and TRKR for 3L and bulk InSe flakes. c) also shows opposite spin polarization for corresponding circular pumps. Figure a) reproduced with permission from Ref. [47].

There has been extensive work on examining spin relaxation mechanisms in III-VI monochalcogenides [34], [35], [44], [49], [88]. The Dresselhaus effect (breaking of centrosymmetry) and the Rashba effect (breaking of mirror plane symmetry) which are generated from symmetry-dependent SOC, can affect the D'yakonov-Perel (DP) spin relaxation mechanism. To model spin relaxation with layer number, Ref [49] has developed a theoretical model where α, the strength of SOC, can be described as:

$$\alpha(\epsilon_z, N) = \alpha_D + \alpha_R \approx \alpha_\infty \left(1 - \frac{\chi}{(N + 2.84)^2}\right) \pm \epsilon_z \eta(N), \tag{3.1}$$

On the left side of the equation, α_D describes the Dresselhaus effect while α_R describes the Rashba effect. The α_D contains the constants $\alpha_\infty = 34.5$ meVÅ and $\chi = 14.9$, which account for the SOC strength at the conduction band edge for a 3D bulk InSe and the nonlinear dependence of bulk SOC, respectively. The contents of α_R are $\eta(N)$ and ϵ_z(electric field). $\eta(N)$ is a slope relating α to ϵ_z. N is layer number.

Spin precision in a SOC field (Ω) for DP effect can be written as $\Omega = \alpha k_f$, where k_f is the Fermi momentum [49]. And assuming the systems measured are in the motional narrowing regime, where the scattering momentum (τ_p) is very fast ($\sim$ 1 ps), the relationship between spin lifetime and spin precession can be described as $1/\tau_s = \Omega^2 \tau_p$. By plugging eq. 3.1 into the DP relationship of Ω to τ_s, the expression is now:

$$1/\tau_s(\epsilon_z, N) \approx \tau_p k_f^2 \left(\alpha_\infty \left(1 - \frac{\chi}{(N + 2.84)^2} \right) \pm \epsilon_z \eta(N) \right)^2, \tag{3.2}$$

This can be further simplified, as there is no applied electric field, thus the expression for the Rashba effect can be dropped ($\epsilon_z = 0$). Other assumptions that can be made include a constant temperature, k_f, and τ_p. All samples were measured at low-temperature (1.7 K) and derived from the same crystal. This leaves the Dresselhaus term and a constant A that contains k_f and τ_p. Eq. 3.2 then can be written as:

$$1/\tau_s(N) \approx A\alpha_D^2(N), \tag{3.3}$$

This than can be inserted into eq 2.6:

$$P(N) = \frac{P_0}{1 + \tau_r A \alpha_D^2(N)}, \tag{3.4}$$

This formulation is then fitted to the the layer-dependent OISO data using P_o and A as the only

free fit parameters (Figure 3.5). This model is not quantitatively accurate, however, it does qualitatively capture the swiftly decreasing P with increasing N. This occurs due to $1/\tau_s$ increasing with thickness, which matches experimental trends found in literature [49].

On the other hand, this model is limited in its scope as it does not account for excitons or for spin-spin scattering, Elliot-Yafet (EY) spin relaxation. This model is designed for nearly-free electrons, thus complexities of electron-hole interactions are ignored. And although predictions expect EY to be negligible [35], experimental work has argued that EY dominates in thicker samples at low-temperature [44]. Future work should incorporate these physical phenomena to better understand the complex dynamics involved in optical spin polarization.

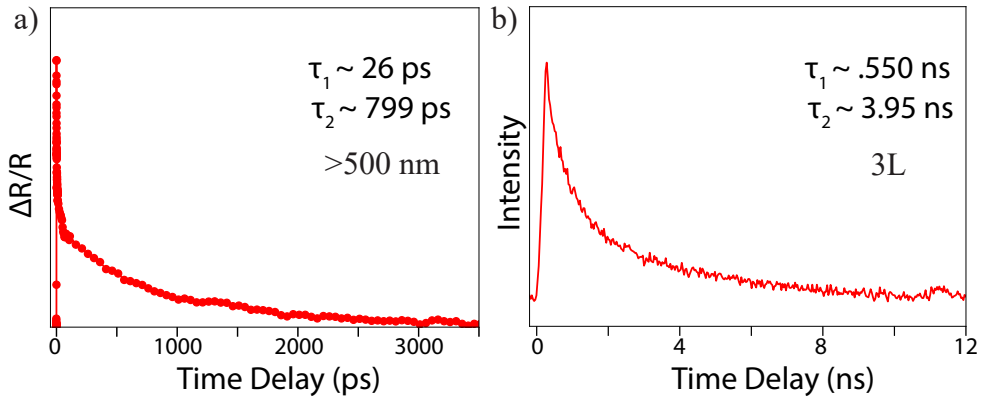

Figure 3.6: TR a) and TRPL b) measurements were conducted in the OptiCool (Figure 2.9) for very thick and very thin InSe flakes.

Knowing that spin lifetimes decrease rapidly with increasing thickness, relative to the recombination lifetimes, it would be informative to confirm directly the difference in spin lifetimes between thinner and thicker layers. Because, If $\tau_s \ll \tau_r$, then it would explain why spin polarization cannot be measured in steady-state polarized PL measurements for thick InSe. Time-resolved studies show that spin polarization in GaSe persists in nanoslabs with thicknesses greater than 100 nm [44]. Thus, polarized TRPL measurements were conducted for 4L InSe flake and TRKR was conducted

for $\geq$ 500 nm InSe flake (Figures 3.5b and 3.5c). Note, for the TRKR measurement on bulk, using opposite circular polarizations for incident pump leads to a θ_K of opposite signs. This is clear indication of OISO in bulk InSe. For a linear pump, the signal is quenched due to no net spin polarization.

From spin sensitive time-resolved measurements, it is evident that 3L InSe has a τ_s that is an order of magnitude larger than that of bulk InSe. Comparing these spin lifetimes to recombination lifetimes (Figure 3.6), it is clear that the ratio τ_r/τ_s is much smaller for 3L than for bulk. This provides additional confirmation for P decreasing with increasing layer number (eq. 2.6), and supports the trend of the qualitative model (eq. 3.3), which accounts for decreasing spin lifetimes due to an increase in spin relaxation.

3.3 Excitonic g-factor

A natural probe of spin dynamics in a material is an applied magnetic field. Conducting the same polarized PL measurement as shown in Figure 2.8a with the attoDry's 9T magnetic field (pointing out-of-plane of the sample), a P dependence with magnetic field (B) for different incident polarizations can be seen for 3L InSe flake in Figure 3.7a. All three excitation polarization follow a linear trend for P vs. B. The slopes of each of these trends are similar, which can be explained as arising from the relaxation and thermal equilibration in the Zeeman-split spin levels (Figure 3.1b). The offsets of both circular pumps are constant at $\sim 16\%$ separation and have opposite sign, thus, once again, demonstrating clearly OISO. The σ_o response is only caused by the Zeeman effect, while the $\sigma_{+(-)}$ responses are due to both OISO and the Zeeman effect.

Due to the Zeeman splitting, the magnitude of the effective out-of-plane g-factor, ($|g^*_\perp|$), can be estimated from the linear trends in P with changing B. Assuming the system is in thermal equilibrium, where excited carriers, before emission, relax into spin states split by an applied

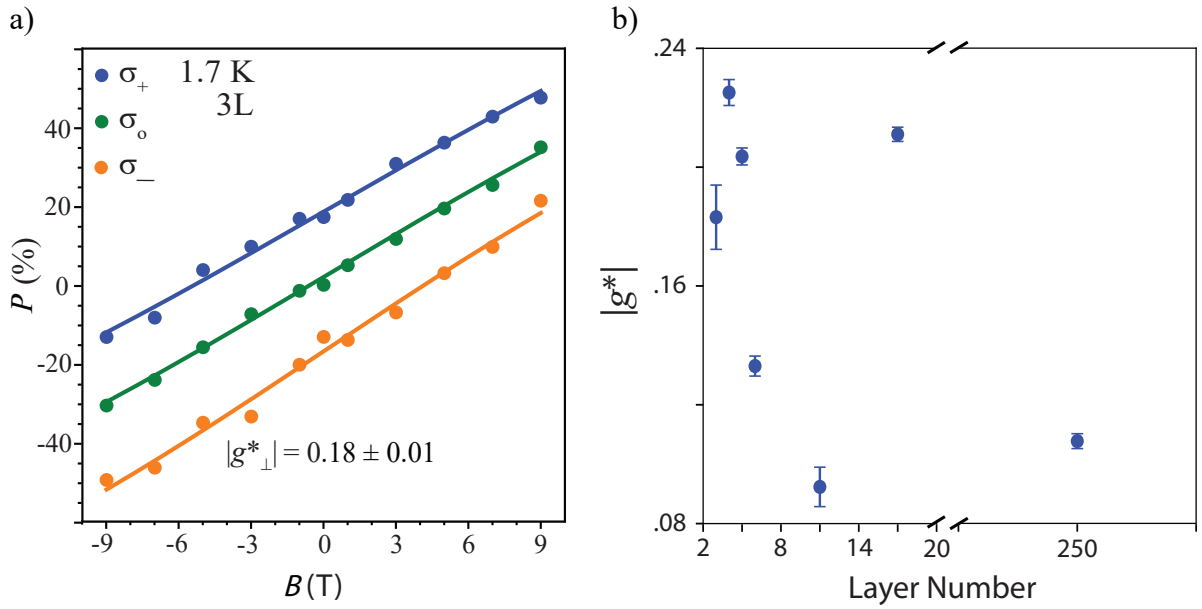

Figure 3.7: a) shows the change in polarization (P) with respect to a magnetic field (B). The three trends represent three difference incident polarizations. These trends are fitted to extract the excitonic effective g-factor in 3L InSe flake. The effective g-factor for different thicknesses are shown in b). All values are roughly on the order of $\sim .1$. Figure reproduced with permission from Ref. [47].

magnetic field, Boltzmann statistics can be used to describe net spin polarization:

$$P = \tanh\left[\frac{\mu_B |g^*_\perp| B}{2k_b T}\right], \tag{3.5}$$

where μ_B is Bohr's magneton, k_b is Boltzmann's constant, and T is temperature. At small fields, P is linear and the slope is related to $|g^*_\perp|$. A $|g^*_\perp| = 0.18 \pm 0.01$ is extracted by fitting eq. 3.5 to the three linear trends and calculating the average and standard deviation. In Figure 3.7b, the extracted values for other thicknesses (3L - 250L) are shown. All values are on the order $\sim .1$. Variation in the g-factor here is due to defects or surface morphology caused by exfoliation or stacking of layers (samples are encapsulated in hBN). Since these are single-sample measurements of g-factor, the error bars underestimate the true variation of the g-factor for different thicknesses. Even so, all

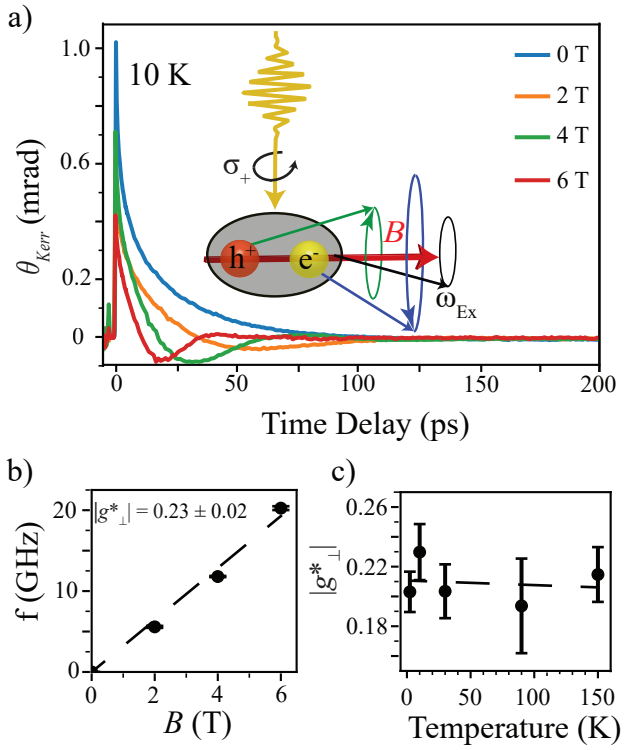

Figure 3.8: a) Oscillation of excitonic spin can be observed in Kerr signal at different field values. Extracted Larmor frequencies at 10K are shown in b). g-factor shows little variation with temperature c). Figure reproduced with permission from Ref. [47].

values sit between .24 and .08 making them relatively consistent.

Further experimental proof that a $|g^*_\perp|$ is on the order of $\sim$ .1 can be found in spin precesion measurements. By applying a transverse magnetic field when conducting TRKR studies (in the OptiCool), spin precession was observed in a bulk InSe flake. With increasing magnetic field, the oscillations within short lifetimes ($\sim$ 25 ps) can be observed in TRKR signal (Fig. 3.8a). This is most clearly shown at 6 T. Due to the few oscillations for accessible fields in the OptiCool (Fig. 2.9), a phenomenological model for procession of spins as they relax is used to describe the data:

$$\theta_K \propto e^{-t/\tau_s} \cos\left[(2\pi f)t\right] \tag{3.6}$$

where here f is the Larmor frequency. The frequency can be written as:

$$f = \frac{\mu_B |g_\perp^*| B}{4\pi} \tag{3.7}$$

This formulation of the frequency dependence, allows for the extraction of the g-factor.

Using eq. 3.6, frequency can be extracted from precession data (Fig. 3.8a). When fitting f vs B with eq. 3.7 (Fig. 3.8b), it was measured that $|g_\perp^*|$ = .23 $\pm$ .02. This g-factor value is similar to what was extracted from the Zeeman model for steady-state polarized PL measurements.

Spin precession measurements are preformed at different temperatures to check for temperature dependence of the g-factor. At each temperature point, the photon energy is changed to maximize θ_K signal (Figure 3.9). $|g_\perp^*|$ is mostly unchanged below 150 K (Fig. 3.8c).

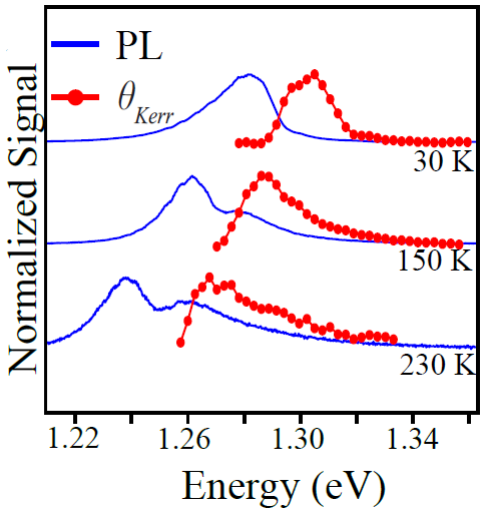

Figure 3.9: θ_k vs photon energy compared to PL at different temperatures. A time slice at 3 ps was used for TRKR measurements [47]. Figure reproduced with permission from Ref. [47].

The g-factor measured in these magneto-optical experiments do not agree with g-factor values found in theoretical [34] or experimental [38] studies for III-VI monochalcogenides. Predictions by Li and Appelbaum estimate that $|g_\perp^*| < 2$ for GaSe and Bandurin *et al.* estimates, from transport

measurements, a g-factor close to 2 for InSe. Both considered the case for nearly-free electrons, which does not apply for optical properties in InSe. Excitons in InSe have large binding energies ($\sim$ 10 meV) [39], [40] and long emissive lifetimes ($\sim$ 1 ns) [39]. Meaning that at room and low-temperatures, magneto-optical properties should be dominated by excitons. Therefore, analysis must take into account excitonic effects if a full explanation for the observed g-factor and its insensitivity to layer number is to be achieved.

3.3.1 Toy Model to Calculate Effective g-factor

In a real crystal, in addition to the Zeeman splitting for the spin of an electron, the Zeeman splitting for the orbital momentum can be sizable in an applied magnetic field [89]. The orbital momentum operator $\boldsymbol{L} = \hbar^{-1}[\boldsymbol{r} \times \boldsymbol{p}]$, where $\boldsymbol{p} = -i\hbar\nabla$, describes the angular momentum of an electron as it orbits an atom. In $\boldsymbol{k} \cdot \boldsymbol{p}$, $\boldsymbol{L}$ can be used to evaluate the orbital g-factor for the conduction and valence bands [90]:

$$\frac{g_n^*}{g_0} - 1 = \frac{1}{im_0} \sum_u \frac{\langle n|\boldsymbol{p_x}|u\rangle\langle u|\boldsymbol{p_y}|n\rangle - \langle n|\boldsymbol{p_y}|u\rangle\langle u|\boldsymbol{p_x}|n\rangle}{E_n - E_u} \tag{3.8}$$

where g_0 = 2, m_0 is the free electron (hole) mass, n is the band in which the effective g-factor is calculated, E_n is the energy of band n, and u denotes a band at energy E_u. $\boldsymbol{p_x}$ and $\boldsymbol{p_y}$ are the x and y components of the momentum operator. For simplicity, eq. 3.8 can be written as [89]:

$$g_{\mathrm{c,v}}^* = 2 + g_{\mathrm{c,v}}^{\mathrm{orb}} \tag{3.9}$$

where c and v represent the conduction and valence band respectively.

The fully-parameterized toy model (eq. 2.1) discussed in Chapter 2.2, was recently formulated by Ref. [42] using $\boldsymbol{k} \cdot \boldsymbol{p}$ to describe the polarized optical selection rules in monolayer InSe. By

using a hopping model (eq. 2.5), this framework can be expanded to multi-layers by ”stacking” monolayer Hamiltonians. As the number of layers increase, interlayer hopping between each layer of InSe splits each band into N subbands. Lower bands experience little splitting while the primary band experiences more splitting, moving the primary valence band further from the next highest valence band. Ultimately, leading to changes in overall band energies and optical spin coupling dynamics in the system [42]. Thus, by using the solutions to the N layer Hamiltonian for the toy model, at the Γ point with appropriate moment matrix elements, one can calculate the orbital g-factor for the conduction and valence band using eq. 3.8 for different thicknesses. Calculations were performed using the *Quantum Notation* package for *Mathematica* (more details can be found in Appendix A). For comparison, the toy model gives $|g_{\mathrm{c}}^{\mathrm{orb}}| \approx .5$ for monolayer, while $|g_{\mathrm{c}}^{\mathrm{orb}}| = .3$ was calculated for monolayer GaSe by Ref. [34]. These values are of similar magnitude.

Figure 3.10 shows the layer dependent $|g_{\mathrm{c,v}}^{*}|$ for InSe. Only magnitudes of the effective g-factor are considered, as measurements conducted in this work cannot determine sign. To calculate the

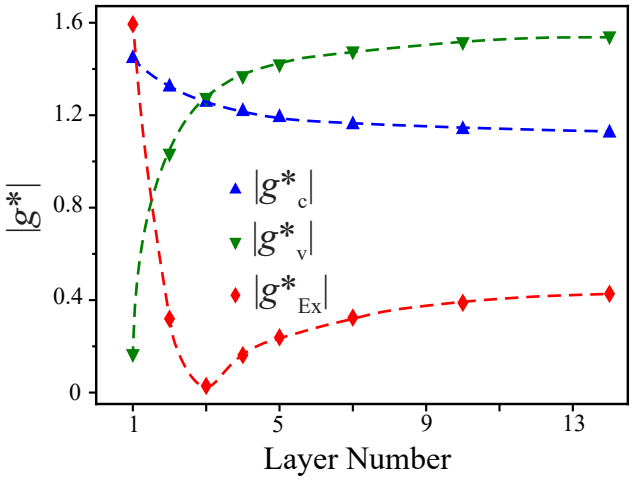

Figure 3.10: $|g^{*}|$ is calculated for electrons ($|g_{\mathrm{c}}^{*}|$), holes ($|g_{\mathrm{v}}^{*}|$), and excitons ($|g_{\mathrm{Ex}}^{*}|$). These were calculated using the toy band model described in Chapter 2.2.1. The dashed lines are for guiding the eye. Figure reproduced with permission from Ref. [47].

excitonic g-factor ($|g^*_{\mathrm{Ex}}|$) a simple formula can be used:

$$g^*_{\mathrm{Ex}} = g_{\mathrm{c}}^{\mathrm{orb}} - g_{\mathrm{v}}^{\mathrm{orb}} \tag{3.10}$$

Between 3L and 14L, the $|g^*_{\mathrm{Ex}}|$ sits between 0 and .4 (Figure 3.10). These values obtained are close to the experimental values extracted in both magneto-optical experiments (steady-state and time-resolved). Demonstrating that the $\boldsymbol{k} \cdot \boldsymbol{p}$ model agrees quite well with experiments.

3.3.2 Density Function Theory to Calculate Effective g-factor

The $\boldsymbol{k} \cdot \boldsymbol{p}$ model is a simple model lacking in-depth details present in real materials and does not explicitly account for excitonic effects. Also, although the parameters used in the toy model are extracted from Density Functional Theory (DFT) calculations for monolayer InSe, the hopping model is a approximation of interactions between layers. Therefore, to provide additional evidence and support for this toy model, a collaboration with DFT experts at Argonne National lab was pursued. Their expertise with III-VI monochalcogenides was ideal, as DFT calculations of band structures in these systems can be very tricky. Band structure results can vary for InSe depending on methodologies [34], [35], [41]. The goal of this collaboration was to model band structures of InSe and then directly calculate the g-factor rather than use a toy model that took fitted parameters from DFT.

Through this collaboration, calculations of the excitonic g-factor for monolayer and bilayer InSe were conducted using *ab-initio* DFT methods that have been recently applied to estimate g-factors in TMDs [91]–[94]. AB stacking (Figure 3.11) was considered for bilayer as it has been shown to be more favorable [95]. To calculate the effective g-factor for band n at wave vector k,

this formulation can be used [91], [96]:

$$g_n(\boldsymbol{k}) = g_0 s_n + 2L_n(\boldsymbol{k}) \tag{3.11}$$

where g_0, s_n and $L_n(\boldsymbol{k})$ represent free electron value of 2, the spin projection, and orbital angular momentum, respectively. For its z-component, the orbital angular momentum is written as [97], [98]:

$$L_n(\boldsymbol{k}) = \frac{2m_0}{\hbar^2} \sum_{m \neq n} \mathrm{Im}[\xi^{(x)}_{nm}(\boldsymbol{k}) \xi^{(y)}_{mn}(\boldsymbol{k})](E_{n\boldsymbol{k}} - E_{m\boldsymbol{k}}). \tag{3.12}$$

$E_{n\boldsymbol{k}}$ and $\boldsymbol{\xi}_{nm}(\boldsymbol{k}) = i\langle u_{n\boldsymbol{k}} | \partial/\partial \boldsymbol{k} | u_{m\boldsymbol{k}} \rangle$ indicate the eigenvalue of band n at wave vector $\boldsymbol{k}$ and the interband matrix of the coordinate operator, respectively. $u_{n\boldsymbol{k}}$ is the periodic part of the Bloch wavefunction which can be obtained numerically in the DFT scheme.

Table 3.1: PBE band gap and excitonic g-factor for a monolayer and bilayer InSe. Table reproduced with permission from Ref. [47].

	band gap (eV)		$\lvert g^*_{Ex} \rvert$			
	Direct	Indirect	$\Gamma \to \Gamma$	$M' \to \Gamma$	$M \to M$	$K \to K$
Monolayer	2.0	1.9	1.3	2.7	1.6	0.2
Bilayer	1.5	1.4	0.1	0.9	0.0	0.3

Using the Generalized Gradient Approximation exchange-correlation functional with Perdew-Burke-Ernzerhof (PBE) parametrization [99] as implemented in the Quantum Espresso package [100], DFT calculations were conducted. Plane-wave basis had a 400-RY kinetic energy cut-off for the energy-consistent norm-conserving Burkatzki, Filippi, and Dolg (BFD) pseudopotentials [101], [102] for In and Se, and $10 \times 10 \times 1$ k grids used for both mono- and bilayer InSe. for bilayer, interactions of van der Waals interlayers were implemented by the dispersion of Grimme (DFT-D3) [103]. Interlayer distance of AB-stacked bilayer InSe is estimated to be 3.2 Å by this method. The calculated band structures are shown in Figure 3.11. The maximum of

the caldera shaped valence band is denoted by M' which is in between the symmetry points Γ and M. Computed band gaps and exciton g-facotrs are organized in Table 3.1.

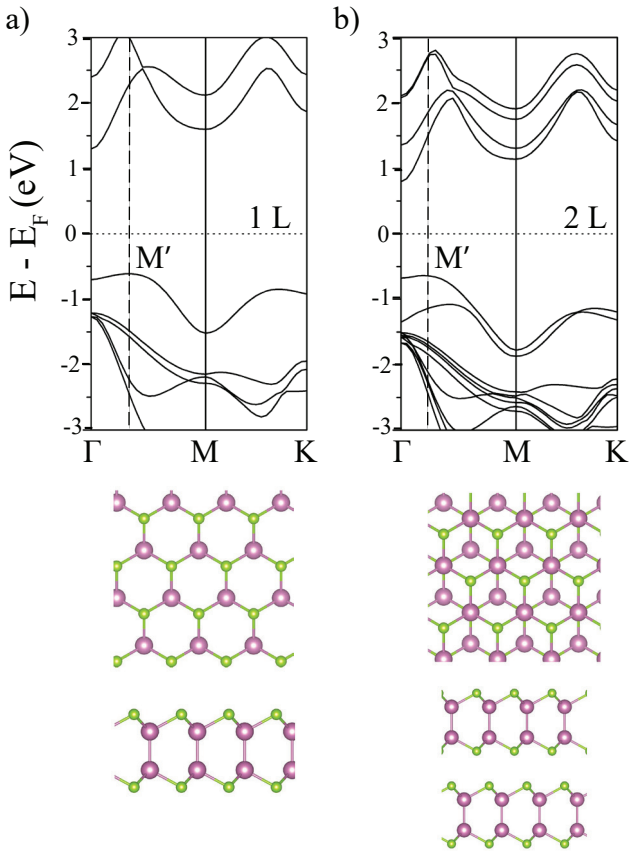

Figure 3.11: PBE band structrues for monolayer a) and bilayer b). Top and side view of a) monolayer and b) bilayer InSe can seen a below DFT plots. Purple and green spheres represent In and Se atoms, respectively. Figure reproduced with permission from Ref. [47].

For the primary band gap transition, $\Gamma \rightarrow \Gamma$, the $|g^*_{Ex}|$ for monolayer and bilayer are 1.3 and 0.1, respectively. When compared to the values calculated from the toy model, 1.6 and .4, it is evident that these results are similar. This is further confirmation of experimental observations and reinforces the utility of the toy model. In addition, of particular noteworthiness, as layer number increases from 1L to 2L, there is a rapid decrease in the excitonic g-factor, a trend exhibited in both

theoretical approaches. Unfortunately, due to limitations in experimental apparatuses, monolayer and bilayer are not explored in this body of work.

In conclusion, even though the toy model and the DFT model do not explicitly incorporate excitonic effects in their band structures, they still offer satisfactory analysis of excitonic spin properties in InSe. Further theoretical work is needed to better describe the quantitative spin dynamics in InSe, since deeper valence bands are also predicted to have spin polarized optical selection rules.

CHAPTER 4

ELECTRICAL TUNING OF POLARIZED EMISSION IN INDIUM SELENIDE

The previous chapter provides evidence for layer-dependent spin polarization in InSe, which is driven by DP spin relaxation that manifests itself through the Dresselhaus effect. This discovery highlights the ability to control excitonic optical spin properties in InSe though thickness. Even so, manipulation of optical spin properties in InSe with other external stimuli, such as electric fields, would offer greater utility and show its promise for real devices. In the literature [49], [104], [105], it has been shown that the Rasbha effect, the breaking of mirror-plane symmetry with out-of-plane electric fields, can tune spin lifetimes in InSe. Yet, these studies solely focused on electronic behavior. Thus, the next logical step is to test if the Rashba effect can tune the optical spin properties of excitons in InSe.

In this chapter, a 4L InSe sample, that was constructed into a lateral field effect transistor (FET) device is studied by polarized PL measurements at different gate voltages. Surprisingly, the tuning of the measured polarized PL is not driven by the tunability of excitonic spin dynamics, but by the tunability of excitonic recombination dynamics. This observation reveals that the Rashba effect does not play a significant role in excitonic spin dynamics, therefore other physical phenomena must be considered to explain the tunability of optical spin polarization in InSe. Although unexpected, this work advances the study of optical spin properties in InSe by investigating the fundamental optical spin characteristics in a InSe device. This work is but a drop in the bucket, yet provides valuable insight into the potential of InSe for future optical spin-based devices.

4.1 Motivation

In chapter three, it is evident that symmetry-dependent SOC can be tuned with thickness. The tunability of SOC due to symmetry breaking is the heart of the emerging field of spin-orbitronics, which aims to harness SOC to control spin dynamics in spin-based devices [106]. Tuning SOC with the Dresselhaus effect is not very efficient, since thickness would need to be constantly modified. However, tuning SOC with the Rashba effect offers the opportunity for effective control of spin dynamics with electric fields. This method has more direct applications to building a usable spintronic devices, as electrical gates can easily be integrated into low-dimensional systems. In some spintronic systems, where both symmetry breaking effects exist, it is possible to suppress spin relaxation in a strong SOC field by tuning the Rashba effect to have a similar magnitude as the Dresselhaus effect. When this occurs, interesting spin textures can form, which are less sensitive to spin scattering [106]. Thus, the overall potential of tuning spin dynamics with the Rashba effect motivates its investigation in III-VI monochalcogenides.

To study Rashba SOC, Ref. [104] fabricated a four terminal multilayer InSe device with an electrical back gate (Figure 4.1a). In this work, they conducted magneto-conductance measurements in order to extract the Rashba SOC strength as a function of applied gate. The values obtained are on par with Rashba SOC strength found in GaSe and WSe_2 [104]. Even though this work showed tunability of SOC in InSe, it did not investigate the interplay between the Dresselhaus effect and the Rashba effect. Ref. [49] performed more in-depth studies on the symmetry-dependent SOC effects and derived an expression to model both symmetry breaking terms (shown in eq 3.1). In this work, it is shown that predictions match closely to experiments for thin InSe.

When taking these two works, Ref. [104] and [49], into consideration, it becomes evident that Rashba SOC can play a significant role in InSe. Yet, the role it could play for optical spin

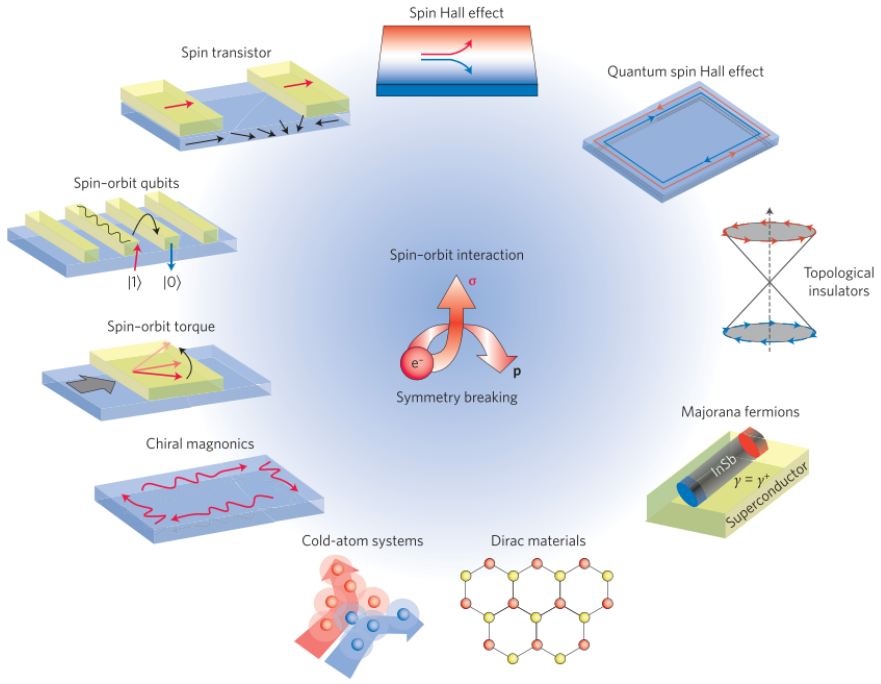

Figure 4.1: This figure highlights the various sub-fields that aim to use SOC as a means to manipulate spin in a system. [106]

properties is not illuminated by these studies, as they both focus on electrical properties. This motivates exploration of another potential 'knob' for tuning optical spin properties in InSe.

To understand the effect, if any, that the Rashba SOC could have on optical spin properties in InSe, collaboration with the Hersam group was essential here as well. This group has ample experience designing functional devices from air-sensitive layered materials. Using the dry encapsulation method [75], they constructed a two-terminal InSe device on SiO_2/Si substrate. A back gate could be applied due to the insulating SiO_2 barrier between the sample and Si. This configuration of the sample, a lateral FET, allows for both doping and basic checks of electrical properties. With such a device, magneto-optical studies can be conducted on InSe. These measurements can reveal excitonic recombination and spin dynamics. In other words, these tools enable an investigation of excitonic response to an applied out-of-plane electric field. Such a study is crucial, as

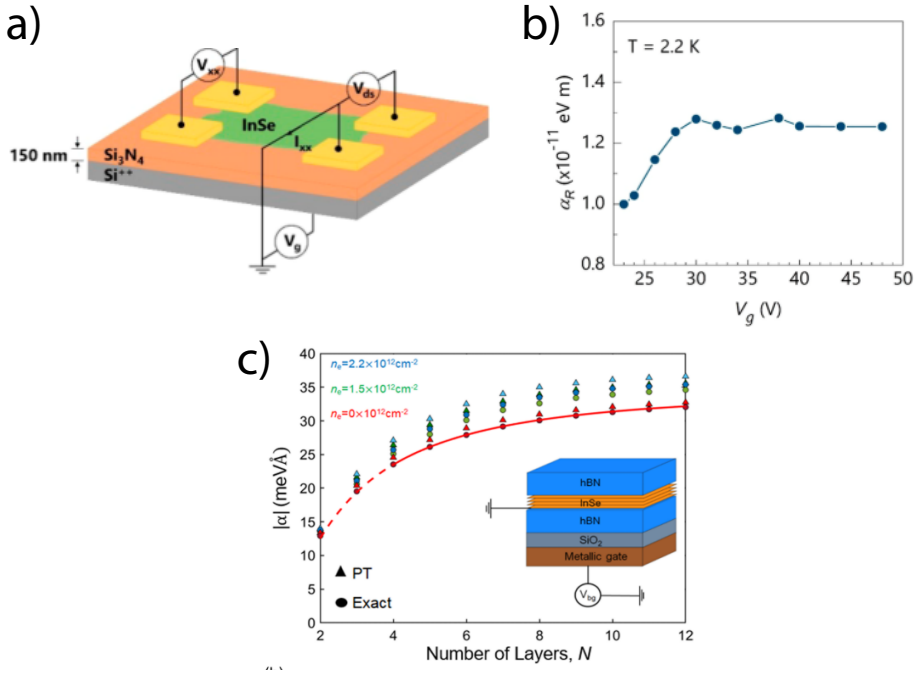

Figure 4.2: a) is a schematic of multilayer InSe device and b) is the strength of Rashba SOC with electrical gate [104]. c) Shows theoretical calculations SOC from both the Dresselhaus and Rashba effect for thin InSe. The inset illustrates the structure that is modeled [49]. Figures a) and b) are reproduced with permission from Ref. [104]. Figure c) is reproduced with permission from Ref. [49].

learning more about the fundamental properties of this carrier will aid in the control of optical spin properties in InSe.

4.2 4L InSe FET Device and Gated Steady-state PL

A 4L InSe flake was exfoliated, encapsulated in hBN, and constructed into a lateral FET device (inset Figure 4.3). The black outlines Gr used to create good electrical contact between the gold and the flake, the green outlines hBN used for encapsulation, and the red outlines 4L InSe flake. Figure 4.3 shows the transfer curves for the device under illumination (1.68 eV) and without il-

lumination. The difference between the 'turn on' for the two curves is $\sim$ 10 V, but they follow the same trend after the gate voltage reaches -10 V. Due to the 450 uW laser, a photocurrent is generated in the 'Laser on' curve giving it additional measured current at lower gate voltages. This photogenerated current is $\sim 10^{-3}\mu$A at $\sim$ -30 V. Overall, the transfer curves follow a general behavior that is consistent with other studies on n-type InSe [38], [107], [108]

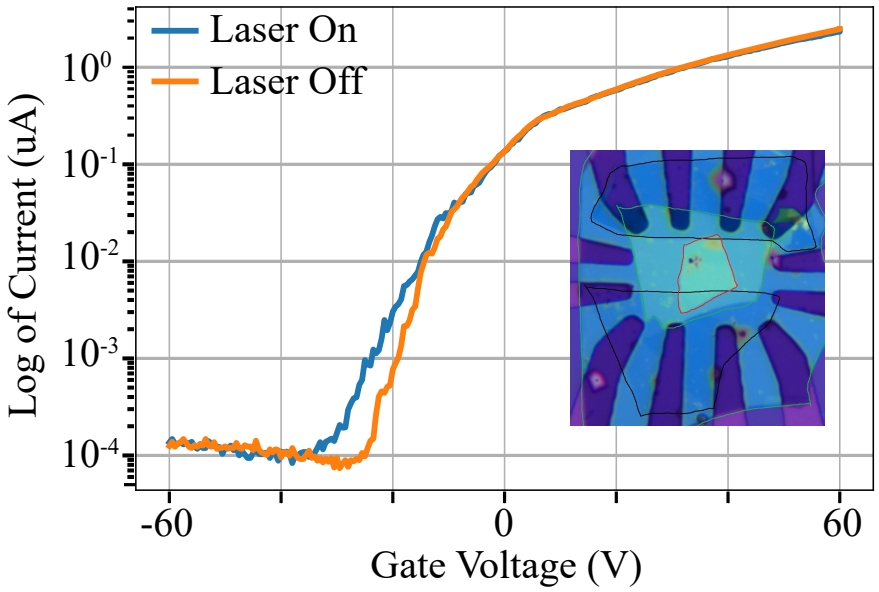

Figure 4.3: Transfer curves for 4L lateral FET device when a 450 μW, 1.68 eV laser is on and off the device. Applied source-drain voltage is 500 mV. Inset is a picture of 4L FET device. The black outlines Gr used to connect the gold contacts to the flake; the green outlines hBN; and the red outlines InSe flake. These measurements were done at 1.7 K in attoDry2100 which has electrical capabilities.

Using the 4L device, gated steady-state PL measurements were conducted and are shown in Figure 4.4. There is a substantial change in the PL as the gate voltage goes from -60 V to 60 V. For high negative bias, PL intensity increases and the PL spectrum becomes narrow, whereas for high positive bias, PL intensity decreases and the PL spectrum becomes wider. The change in center wavelength is roughly $\sim$ 30 meV. Note, that as gate voltages goes in the positive direction,

above $\sim$ -35 V (Figure 4.3), electron carrier density increases. The reason the system becomes less optically active with higher doping is most likely due to scattering processes [109].

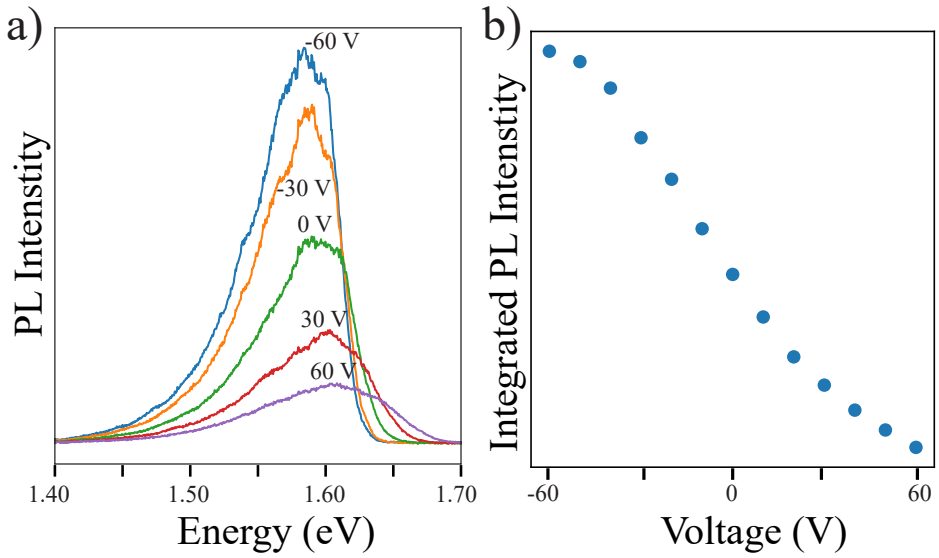

Figure 4.4: a) PL spectrum of 4L InSe flake at four different gate voltages using a pump laser of 2.13 eV. Figure b) is the integrated PL with voltage, which takes on an S-like shape. These measurements were done at 1.7 K in attoDry2100 which has electrical capabilities.

4.3 Gated Steady-state Polarized PL and Time-resolved Polarized PL

To study the effects of gate on polarized PL, a similar setup as shown in Figure 2.8a was used in Quantum Designs' OptiCool . This was done by using the low-working distance top window (Figure 2.9b) and a 100X long working distance objective. The OptiCool is equipped with electrical capabilities, allowing for low temperature gated PL studies. Steady-state polarized PL measurements are shown in Figure 4.5a. Along with change in overall PL shape, the degree of circular polarization (P) changes from $\sim 2\%$ to $\sim 7\%$ as the gate goes from negative to positive.

To measure time-resolved dynamics, a pulsed laser, single photon detector, and PicoQuant's

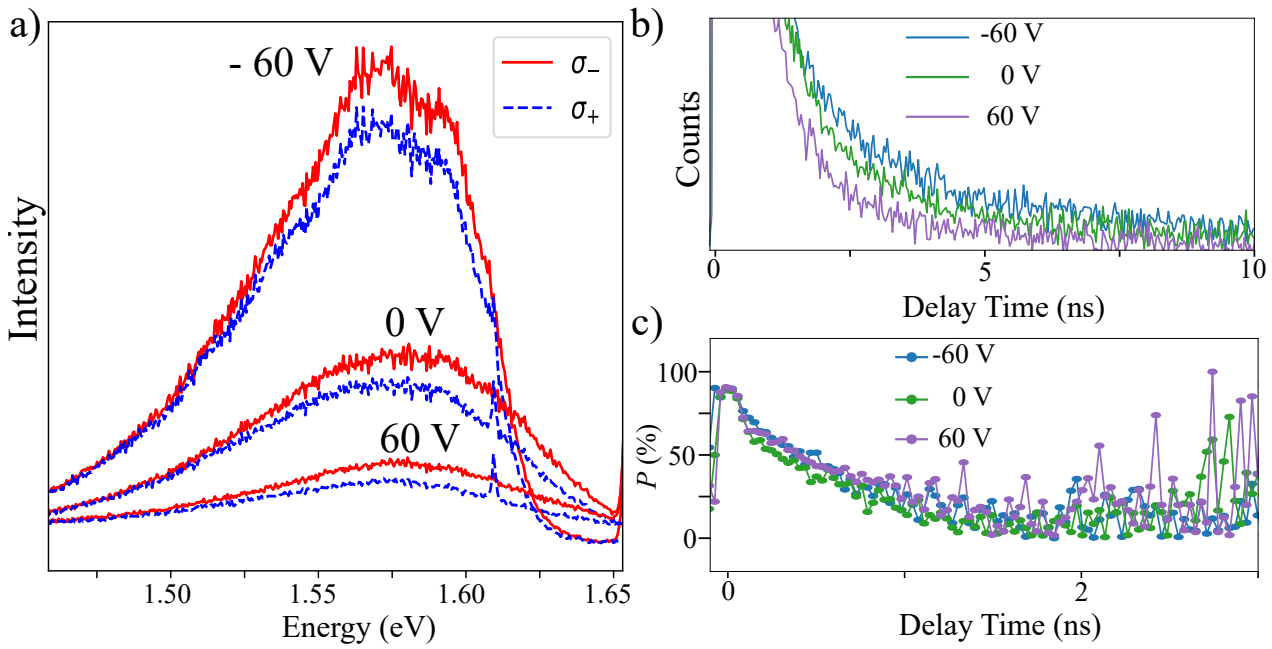

Figure 4.5: a) Polarized PL for three different gate voltages using a pump laser centered at 1.68 eV. Polarization is $\sim 2\%$ for -60 V, $\sim 4\%$ for 0 V, and $\sim 7\%$ for 60 V. TRPL b) and polarized TRPL c) are shown at different gate voltages. b) focuses on the long decay of the recombination as it is clearly changing with gate. All measurements were done at 2 K in the OptiCool.

event timer hardware (HydraHarp 400) were used. This setup allows for direct measurement of radiative recombination and spin relaxation dynamics at different gate voltages. Radiative recombination lifetimes for excitons are expected to change with gate as [110]

$$R = Bnp, \tag{4.1}$$

where R is the radiative recombination rate (the inverse of radiative recombination lifetime), B is the radiative recombination probability, n is electron concentration, and p is hole concentration. As concentration increases, the radiative lifetimes should decrease. When looking at steady-state PL measurements (Figure 4.4), this expectation is seen as brighter PL and dimmer PL, as lifetimes can

correspond to PL brightness. To support this conclusion, TRPL indicates that the recombination lifetime increases for a negative gate voltage and decreases for a positive gate voltage (Figure 4.5b). Thereby corresponding bright and dim steady-state PL to lower carrier density and higher carrier density, respectively. On the other hand, spin lifetimes measured by polarized TRPL are insensitive to gate voltage. Based on the literature [49], [104], [105], electron spin lifetimes change due to the Rashba effect for few-layer and thick InSe. Yet, measurements presented here suggest that the spin polarization read-out of excitons, from steady-state polarized PL, is driven by recombination dynamics. This requires a revaluation of the mechanism for the measured P. The implications of these results and description of key physical phenomena are covered in the Discussion section.

4.4 Discussion

By plotting P versus gate voltage for measured 'Data' (orange circles), a S-like trend can be observed in Figure 4.6a. The typical theoretical framework for understanding the steady-state P is describe by eq. 2.6. Assuming the initial polarization (P_0) does not change much with gate voltage as the center PL energy only drifts $\sim$ 30 meV, the driving parameters in this equation are the radiative recombination and spin lifetimes. In Figure 4.6b, the extracted values for fast radiative lifetimes (τ_1), excitonic radiative recombination lifetimes (τ_2), and spin lifetimes (τ_s) can be seen. Both τ_1 and τ_s are constant with gate voltage within accuracy of TRPL and polarized TRPL measurements. The excitonic recombination, on the other hand, also takes on an S-like trend with gate voltage.

Plugging the extracted lifetimes into eq 2.6, and having only P_0 as a fitting parameter, the resulting model can be plotted (Figure 4.6a, green triangles). This model, however, poorly predicts the observed experimental values except near 0 V. Indicating that the model is not accounting for some additional effect caused by the changing of carrier concentration in the system. When fitting

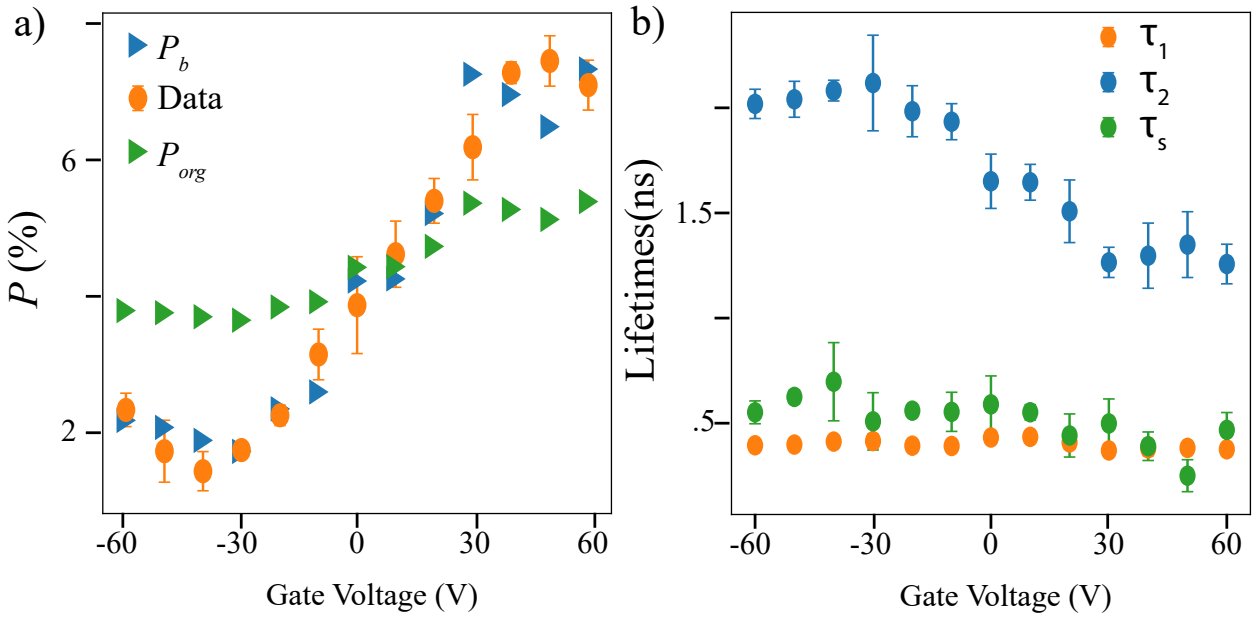

Figure 4.6: a) orange circles (data) are P calculated with integrated intensity from steady-state polarized PL measurements. Green triangles were calculated by plugging extracted lifetimes into eq. 2.6. Blue triangles (P_b) were calculated using eq. 4.2. Lifetimes for fast recombination (τ_1), exciton recombination (τ_2), and spin lifetimes (τ_s) can be seen in b). These values were extracted from TRPL and polarized TRPL measurements.

the model

$$P_b = \frac{P_0}{1 + \tau_2/\tau_s} \pm b, \tag{4.2}$$

where b is additional fitting parameter, a better agreement between measurement and theory can be seen. Having a two parameter fit is likely taking into account polarization effects occurring from a changing carrier density that is not accounted for in the ratio τ_2/τ_s. In Ref. [5], they show a derivation of steady-state P equation that contains doping levels of a semiconductor, before simplification [5]

$$P = \frac{P_0 - n_o p_o/(np)}{1 + 1/(\tau_s R p)}, \tag{4.3}$$

the index 'o' denotes concentrations at equilibrium. Although eq. 4.2 does not have the exact form

or dependence as eq. 4.3, it does hint that the approximations made to acquire eq 2.6 from eq. 4.3 (see reference [5] for more detail) do not hold for InSe with applied gate bias.

The change in the PL spectrum with gate voltage, hence the change in radiative recombination lifetimes with gate voltage, is not a factor that has been extensively investigated in InSe. With the limited measurements here and recent model for excitonic dynamics in a III-VI semiconductor [111], it is possible to understand, at least in concept, what is potentially happening in this system.

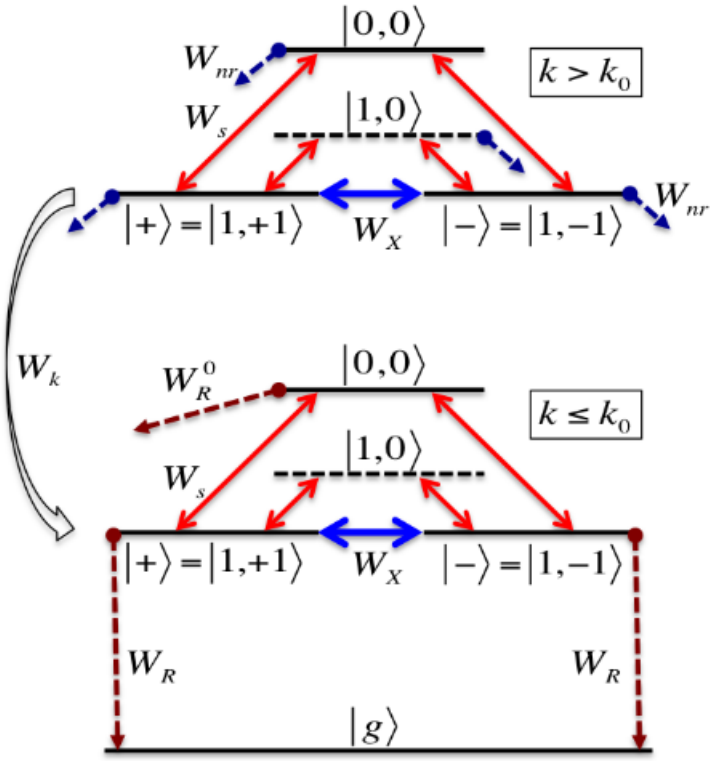

Figure 4.7: Schematic of excitonic dynamics. Figure is reproduced with permission from Ref. [111].

Figure 4.7 depicts an excitonic dynamical model originally formulated for GaSe. This particu-

lar model is modified from the original excitonic dynamics model derived by Ref. [112]. Excitonic states are labeled as $|\pm\rangle \equiv |1, \pm 1\rangle$, $|1, 0\rangle$, and $|0, 0\rangle$. These states represent spin polarized states, an optically inactive state, and the A line transition state (Figure 2.3), respectively. Exciton spin-flip is denoted by the rate W_X and electron/hole spin-flip, which is indistinguishable in these measurements, is labeled by W_s. Carriers with momentum (k) larger than the photon momentum (k_0) enter non-radiative high-momentum states ($k > k_0$) which decay at a rate of W_{nr}. Excitons can be scattered by acoustic phonons at a rate of W_k. This scattering is spin-conserving, thereby allowing excitons to enter low-momentum states ($k \leq k_0$). Radiative recombination rates W_R and W_R^0 represent the measured PL decay, with W_R^0 being a very small contribution due to weakly coupled A line transition.

This excitonic dynamics model (Figure 4.7) is a useful description that will be extrapolated here for InSe, which has similar optical selection rules as GaSe [43], [57], to create a conceptual explanation for PL behavior observed at different gate biases. At zero gate bias, the estimated width of the PL spectrum is $\sim$ 100 meV which could be the result of the caldera shape valence band [85], [86]. This implies that there is decent momentum spread of excited excitons in the system as these particles could be excited across the primary valence band. When the gate bias voltage becomes more negative, the number of charge carriers decreases (Figure 4.3), and the resulting PL spectrum is more narrow and bright (Figure 4.4). Implying a smaller spread in excitonic momentum and less scattering. Vice versa is true for more positive gate voltages. Thus, the width and intensity of the PL may be indicative of whether more excitons are entering radiative or nonradiative states. A more negative bias would then generate more radiative excitons while a more positive bias would would generate more nonradiative excitons.

Ref. [111], estimated nonradiative recombination rates and scattering rates to be $W_{nr} < 10^{-4}$ ps^{-1} and $W_k = 1$ ps^{-1}. The rate of phonon scattering is larger than the nonradiative recom-

bination for the case considered in Ref [111] for GaSe, which would allow for more carriers to enter the radiative state. Even though the excitonic dynamic model does not explicitly consider types of nonradiatve decays, it can be insightful to discuss this physical dynamic. Beyond just surface recombination [113], the two prominent nonradiative recombination processes, that also have doping dependence, in semiconductors are the Shockley-Read recombination process and the Auger recombination process [109]. The Shockley-Read recombination is driven by the capture of electrons or holes by recombination centers in the band gap, which are created by defects or impurities in a crystal. The Auger recombination is a three body process where the recombination of an electron-hole pair gives energy to a electron or hole that then scatters with the lattice. At carrier densities that cause the Fermi-level to sit deep into the conduction or valence band, Auger recombination tends to dominate [114]. Also, Auger coefficients, related to the probability of these processes occurring, can change with carrier density [115]. Thus, an increase in electron carrier density in InSe could not only be increasing the number of excitons in higher momentum states, but also the probability of excitons to nonradiatively decay. Although it is not possible to directly measure Shockley-Read or Auger recombination in the current setup, it does highlight features that may offer another channel for particles to recombine.

By considering how carrier concentration affects radiative lifetimes, nonradiative lifetimes, and excitonic momentum states, it is possible to see that a medley of physical phenomena influence PL dynamics in InSe. This work reveals an intriguing landscape that is yet to be fully unpacked and explored. This is left for future work as the studies that could be conducted to investigate these phenomena in-depth are beyond the scope of this dissertation.

In summary, even though gated PL measurements demonstrate that exciton spin lifetimes are not very susceptible to the Rashba effect, it is still possible to tune the optical spin polarization with recombination dynamics. Suggesting the feasibility of controlling the read-out of optical

polarization in an InSe device. The ability to turn it ’off’ and ’on’, showcases the potential of InSe for a optical spin-based device that resembles the functionality of a logic device.

CHAPTER 5

III-VI MONOCHALCOGENIDES PAIRED WITH 2D MAGNETIC MATERIALS

The previous two chapters discuss how layer number (Chapter 3) and electrical gating (Chapter 4) can change optical spin polarization by affecting excitonic spin dynamics and recombination dynamics, respectively. These two adjustable parameters, in conjunction with polarized light, act as 'knobs' that offer unprecedented control over optical spin phenomena in InSe. Even so, work presented in previous chapters do not fully capitalize on the 2D nature of InSe. This 2D nature presents opportunities to engineer, layer-by-layer, exotic heterostructures with unique and advantageous capabilities. It would be exciting to pair InSe, a material with high electron mobility and measurable optical spin phenomenon, with a 2D material that is complimentary. There are studies combing hBN, Gr, and InSe to create robust devices with good electrical performance [116], [117], but experimental work with more intriguing and novel materials are lacking. This is despite promising predictions of optical spin control in InSe heterostructures with 2D magnets [118], [119]. Since the discovery of sustained magnetism in monolayer and few-layer CrI_3 [120], 2D magnets have attracted much attention and a plethora of studies have been conducted [14], [121]–[123]. Pairing InSe with 2D magnetic materials presents new possibilities and an exciting direction for spintornic research with 2D van der Waals systems.

Therefore, this chapter of the dissertation describes a new direction for research on optical spin properties in InSe. Due to the novelty of 2D magnets such as CrI_3 and predictions of interesting coupling between InSe and CrI_3, it is promising to study the juxtaposition of InSe with CrI_3. This combination could allow for novel control over optical spin properties in a InSe heterostructure. First, this chapter will cover background information for 2D magnets, in particular CrI_3. Next, it

will discuss predictions of induced magnetism in InSe. And lastly, the final two sections will cover preliminary studies and proposed future studies for InSe/CrI_3 heterostructures.

5.1 2D van der Waals Magnets

The landscape of van der Waals materials has rapidly expanded over the last two decades. It includes metals, semi-metals, semiconductors, insulators, superconductors, and topological insulators. The prospect of designing extraordinary layered structures and devices with these various building blocks is exhilarating [12], [124]! Yet, until recently, a 'Lego' piece had been missing, magnetic van der Waals materials. Although predictions of 2D magnetism have existed since the 1960s [125], [126] and have inspired experimental investigation in ultra thin magnetic films, experimental studies of 'true' 2D magnetic systems did not occur until the late 2010s [127].

Recently, almost two decades after the discovery of atomically thin Gr [11], which reinvigorated materials research, CrI_3 was successfully exfoliated down to a monolayer and its layer-dependent magnetic properties were experimentally confirmed [120]. Since then, the number of 2D van der Waals magnets have grown considerably [14], [122]. With such a large selection of 2D magnetic materials to choose from, it is no longer a dream to test fundamental physics models such as the Ising model, Heisenberg model, XY model, etc. [121] in a true 2D system. These layered magnets are also susceptibility to external fields (Figure 5.1) and can interact with other van der Waals materials such as TMDs [14], [121], [123]. When considered together, this diverse set of features highlight riveting physical phenomena and offer modalities in which to control magnetism in 2D magnets. Out of this larger class of van der Waals materials, transition metal trihalides have been examined extensively. A summary of these 2D magnets is given in the next section.

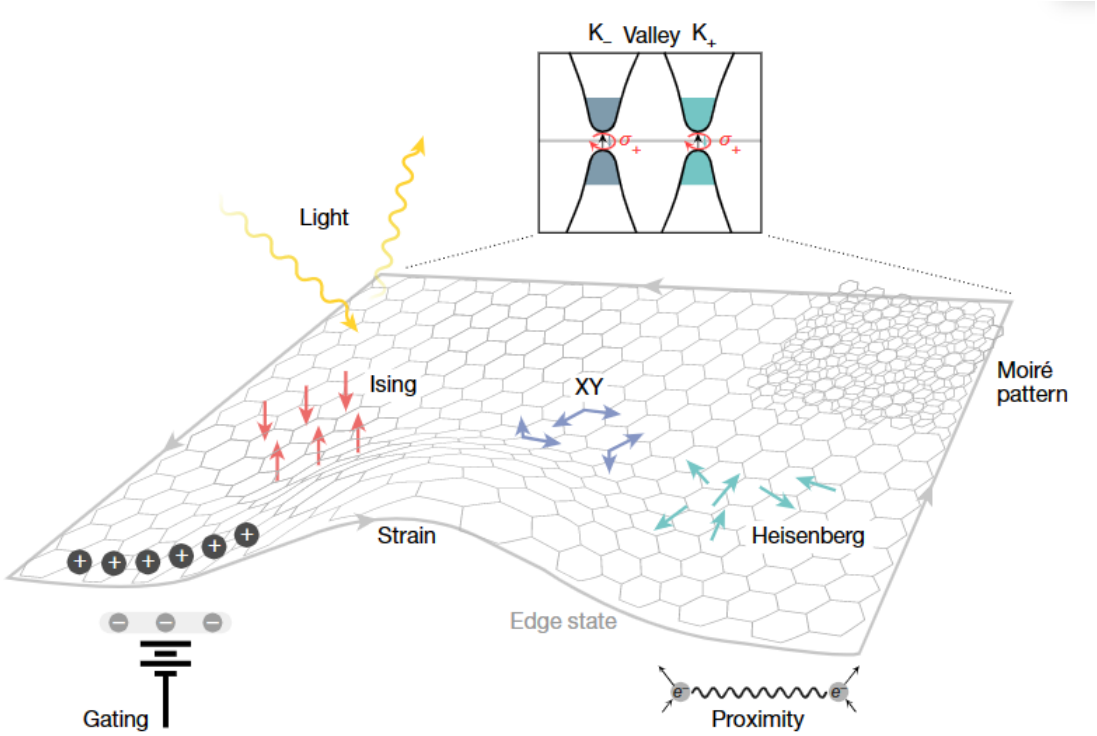

Figure 5.1: There are a number of physical phenomena that can be explored with magnetic van der Waals materials. This includes magnetism models, the effect of external stimuli (electrical, magnetic, strain, optical, stacking), and interactions with other layered materials such as TMDs. Figure reproduced with permission from Ref. [121].

5.1.1 Transition Metal Trihalides

Transition metal trihalides, or MX_3 (M = V, Cr, Mn, Fe, Co, Ni, Ru; X = Cl, Br, I), are composed of transition metals cations, which typically have partially filled 3d electronic shells, and halide anions, which have large radii. This configuration is favorable for local magnetic moments and produces ordered magnetism [14], [122]. The crystal structure takes on the form of a honeycomb lattice with weak interlayer van der Waals interactions (Figure 5.2a). Due to interlayer orbital hybridization being sensitive to stacking order, the interlayer exchange interaction can create conditions favorable to ferromagnetic ordering (Rhombohedral stacking) or antiferromagnetic ordering

(Monoclinic stacking) [128]. An illustration of these stacking orders can be seen in Figure 5.2b.

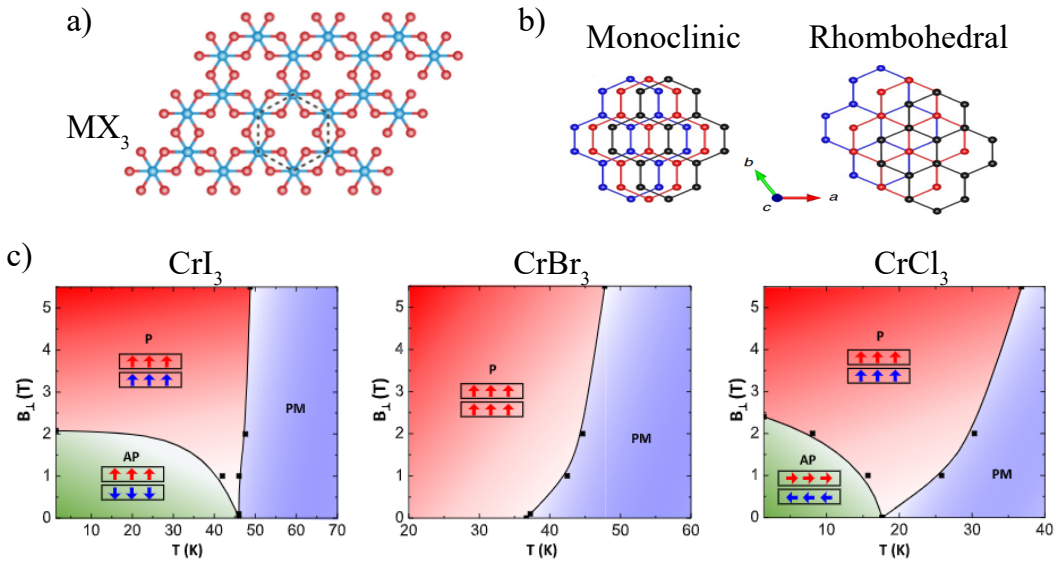

Figure 5.2: a) illustration of crystal structure of MX_3 materials [129]. b) illustration of monoclinic and rhombohedral stacking orders [128]. c) shows a phase diagram for CrI_3, $CrBr_3$ and $CrCl_3$ [130]. All figures are reproduced with permissions of each reference.

The number of MX_3 materials is large (more than 20) [14], but there has been significant focus on chromium halides (CrX_3), as one of the seminal papers [120] that garnered renewed enthusiasm for 2D magnets was done on CrI_3. Figure 5.2c shows field ($B_\perp$) vs. temperature (T) phase diagrams for CrI_3, $CrBr_3$, and $CrCl_3$. CrI_3 and $CrCl_3$ have ferromagnetic and antiferromagnetic phases whereas $CrBr_3$ only has a ferromagnetic phase. Out-of-plane ferromagnetism exist for all three while in the antiferromagnetic phase, $CrCl_3$ has in-plane magnetism and CrI_3 has out-of-plane magnetism. Due to SOC and the exchange interaction, Curie temperatures for the three materials are 17 K ($CrCl_3$), 37 K ($CrBr_3$), and 45 K (CrI_3) [130]. It has also been shown that CrI_3 and $CrCl_3$ can be modeled by the XY model and the Ising model while $CrBr_3$ has a mixture of both the Ising model and the Heisenberg model [131].

CrX_3 are semiconducting materials that have been studied through both electrical and optical

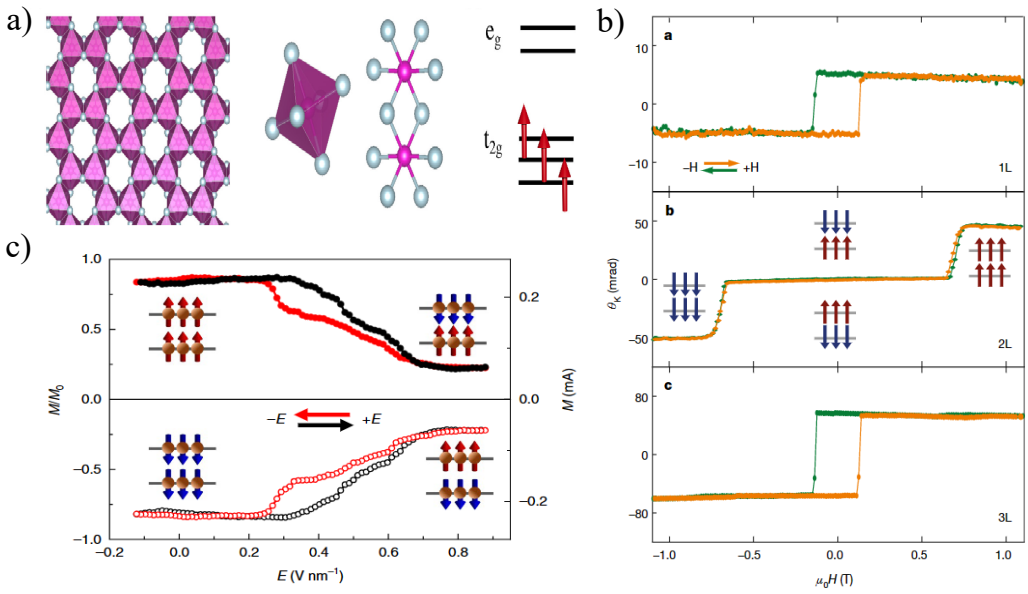

Figure 5.3: a) octahedral structure of CrI_3 with labeled double degenerate (e_g) and triple degenerate (t_{2g}) d orbital states [132]. b) magneto-optical Kerr effect (MOKE) measurement of monolayer CrI_3 (top), bilayer CrI_3 (middle) and trilayer CrI_3 (bottom) [120]. c) the change in magnetization of bilayer CrI_3 with electrostatic field [133]. All figures are reproduced with permission of respective references.

experiments [14], [121]. To highlight some of these characteristics, CrI_3 will be discussed in further detail. Monolayer CrI_3 is composed of Cr^{3+} ions which give an electronic configuration under edge sharing octahedral crystal fields coordinated by six nonmagnetic I^- (Figure 5.3a) [132]. In this structure, Cr^{3+} ions prefer a spin state of 3/2 with 3d orbital electrons that occupy the lowest energy triplet state. The competing effects of exchange interactions with Cr-Cr sites and near 90° Cr-I-Cr bonds, drives the long-range ferromagnetic ordering which can be measured in optical measurements [132]. Using the magneto-optical Kerr effect (MOKE), a steady-state measurement where Kerr angle changes with magnetic field, it was first shown that CrI_3 was a 2D magnet down to the monolayer (Figure 5.3b top). In the bilayer case, interlayer interactions can create antiferromagnetism as spins in only one layer will flip with changing field (Figure 5.3b middle). And

ferromagnetism returns in the trilayer (Figure 5.3b bottom). It has also been shown that CrI_3 magnetism can be controlled with doping (Figure 5.3c), demonstrating further potential applications for spin-based devices. All-in-all, CrX_3 are promising materials for 2D spintronics, thus motivating pairing them with other 2D materials to potentially build next generation 2D spin-based devices.

5.1.2 Magneto-optical Properties in Chromium Trihalide and TMD Heterostructures

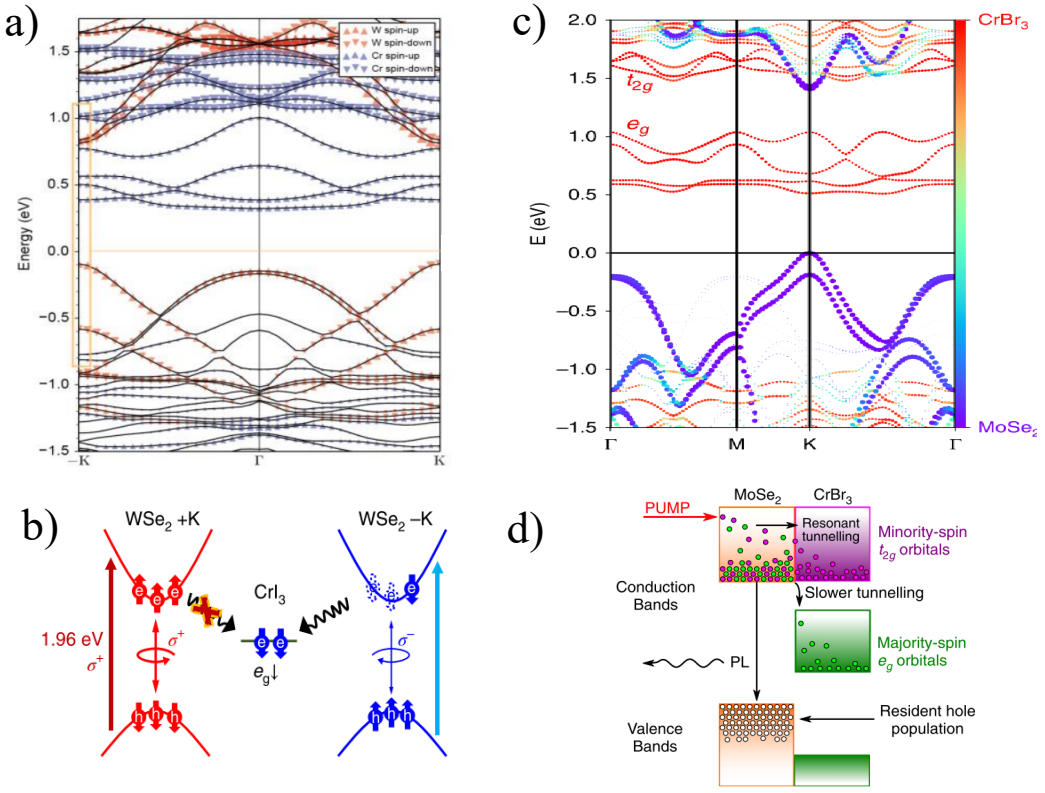

Figure 5.4: a) and b) are the DFT band structure [134] and schematic of charge transfer [135] for WSe_3/CrI_3. c) and d) are the DFT band structure and schematic of charge transfer for $MoSe_2/CrBr_3$ [136]. a) is reproduced with permission from Ref. [134]. b) is reproduced with permission from Ref. [135]. c) and d) are reproduced with permission from Ref. [136].

After discovering 2D magnetism and exploring its fundamental physics, the next intriguing research pursuit is 'stacking' them on other van der Waals materials to create novel heterostructures.

For possible application in magneto-optical devices, the most likely candidates to pair these 2D magnets with are TMDs. The reason for this lies in the band structure alignment between CrX_3 and TMDs. Figures 5.4a and 5.4c show DFT band structures for WSe_2/CrI_3 and $MoSe_2/CrBr_3$, respectively.

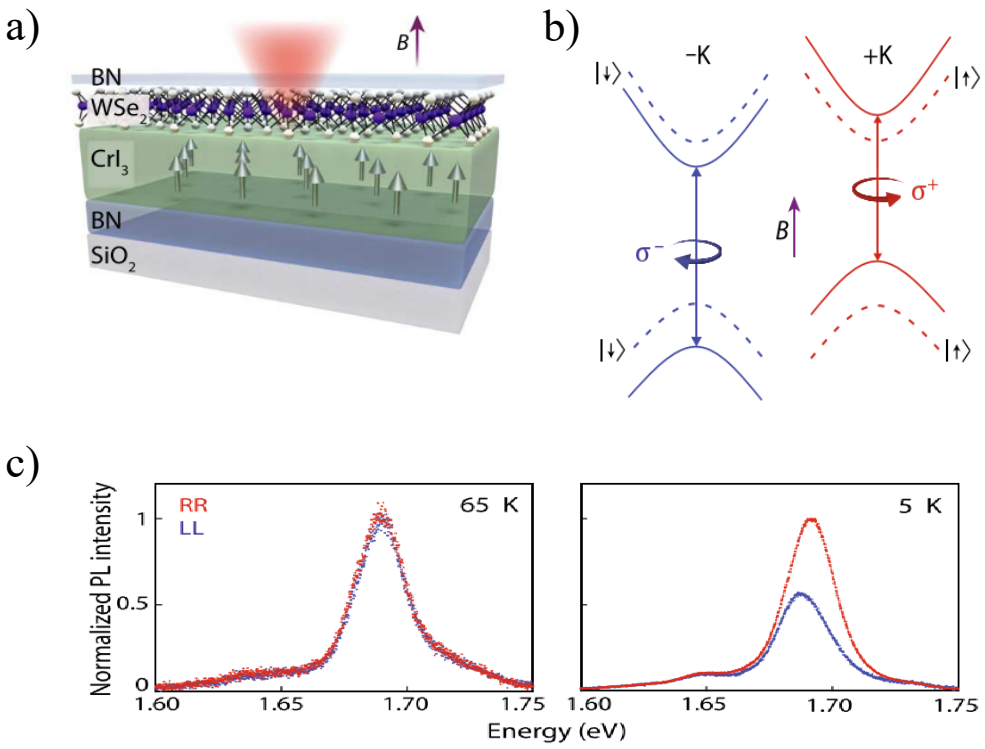

Figure 5.5: a) Illustration of WSe_2/CrI_3 encapsulated in hBN. b) Schematic of shifted K-valley and K'-valley due to effective magnetic field from CrI_3. c) shows the polarized emission above and below the Curie temperature for CrI_3 (45 K). Figures are reproduced with permission from Ref. [134].

Due to a staggering gap (Type-II) [137], charge transfer occurs, aiding in the imbalance between the two valley states when light is used to excite the system (Figures 5.4b and 5.4d). When the magnetic field of the CrX_3 aligns with the photoexcited spin in the TMD, this allows for selective charge transfer to occur. The aligned spin carriers then nonradiatively decay [134]–[136].

To measure this induced spin imbalance between the K-valleys generated by the proximity effect, Ref. [134] measured the polarized PL emission from a WSe_2/bulk CrI_3 heterostructure encapsulated in hBN (Figure 5.5a). The effective magnetic field was estimated to be 13 T, thus causing a sizable splitting between K-valleys (Figure 5.5b). As a result, below the Curie temperature of CrI_3, there is clear difference in polarized PL emission from the two valley states (represented by the collection of opposite helicities of circularly polarized light) even when no magnetic field is applied (Figure 5.5c).

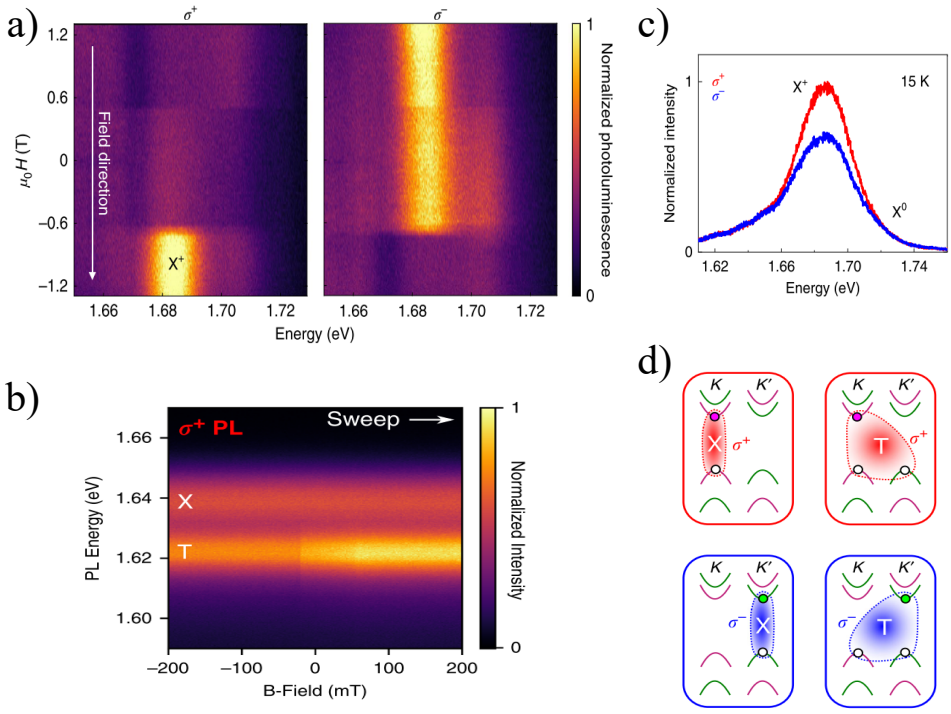

Figure 5.6: Heat map shows changes in PL intensity with field for a) WSe_2/CrI_3 [135] and b) $MoSe_2/CrBr_3$ [136]. c) shows polarized PL for WSe_2/CrI_3 with no applied magnetic field. The trion is polarized in PL whereas the exciton is not [135]. d) illustrates exciton and trions formation in K-valleys [136]. a) and c) are reproduced with permission from Ref. [135]. b) and d) are reproduced with permission from Ref. [136].

In TMDs, excitons and trions are common photoexcited carriers that can emit from recombin-

ing in the optically active K-valleys (Figure 5.6d) [136]. Thus when examining the magneto-optical characteristic of TMD/CrX_3 heterostructures, understanding how these carriers behave under a effective magnetic field induced by the proximity effect is important.

When measuring the polarized PL emission from WSe_2/CrI_3 (Figures 5.6a and 5.6c) and $MoSe_2/CrBr_3$ (Figure 5.6b) heterostructures, it is obvious that excitonic carriers are insensitive to effective magnetic fields generated by the 2D magnets. The trion peaks, on the other hand, clearly change with a varied applied magnetic field. This result could be explained by decay lifetimes. Likely, the nonradiative decay is slower than the radiative lifetime of the exciton but faster than the radiative lifetime of the trion [135], [136].

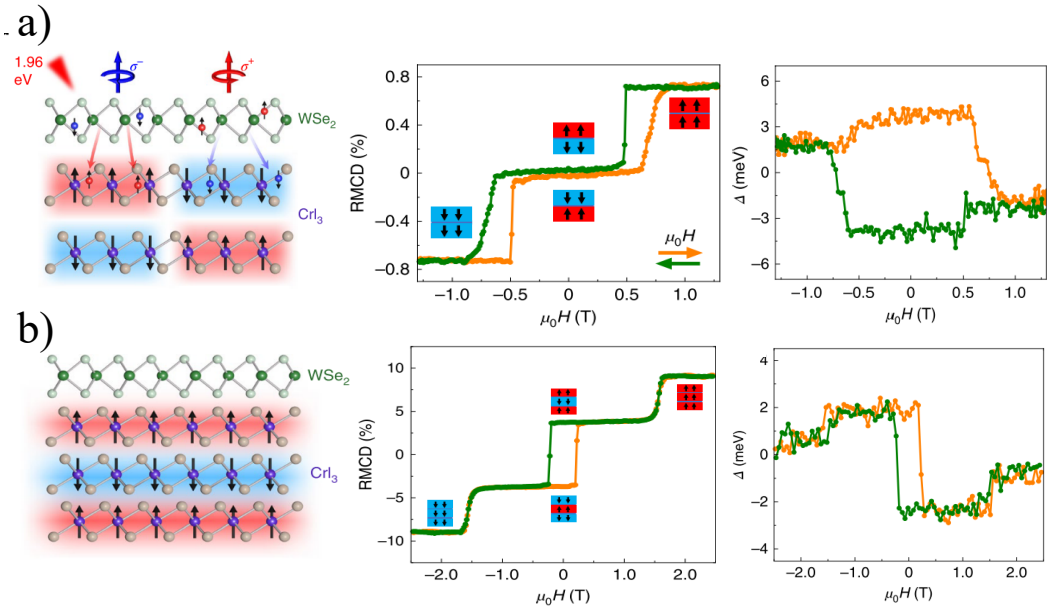

Figure 5.7: a) and b) are illustrations, RMCD plots, and valley Zeeman splitting for WSe_2/CrI_3 with bilyaer CrI_3 and trilayer CrI_3, respectively. Figures are reproduced with permission from Ref. [135].

Ref [135] further investigates magneto-optical properties of WSe_2/CrI_3 by conducting reflective magneto-circular dichorism (RMCD) measurements with bilayer and trilayer CrI_3 (Figure 5.7).

RMDC plots in Figures 5.7a and 5.7b show that bilayer CrI_3 is antiferromagnetic and trilayer CrI_3 is ferromagnetic, which is expected [120]. The effect that the bilyaer and trilayer have on valley splitting, which is shown in middle image of Figure 5.7a and 5.7b, is starkly different. The strength of valley splitting in the antiferromangetic configuration is stronger than in the ferromagnetic configuration. This is due to very different band edge energies of the two magnetic configurations [135].

The study of TMD/CrX_3 has revealed interesting interlayer dynamics between a 2D valley materials and 2D magnets. It has also shown the possibility of combing complimentary 2D materials to create unique magneto-optical devices, motivating new investigations into other types of heterostructures with 2D magnets.

5.2 Predictions: III-VI Monochalcogenides and Magnetism

As mentioned in the Chapter one, the ability to have all optical control of spins allows for rapid and efficient manipulation of spin states that could have immense utility in optical-spin based devices [5]. Thus, building a device with robust optical and magnetic components paves the way for future 2D spintronic systems. The first section addresses theoretical predictions of magnetism in hole-doped III-VI monochalcogenides while the second addresses theoretical predictions of MX/CrI_3 heterostructures.

5.2.1 P-type III-VI Monochalcogenides and Ferromagnetism

Refs. [52]–[54] conducted theoretical studies on tunable magneto-optical effects in hole-doped III-VI monochalcogendies. This phenomena is driven by the Stoner mechanism, which describes spontaneous magnetism in a solid [52]. This occurs in III-VI monochalcogendies due to the top most valence band taking on the shape of a caldera. This band structure give rises to a van Hove

singularity in the density of states. It is predicted that if the Fermi level reaches this singularity, magnetism can be induced in the system [52]–[54]. Figure 5.8a shows four DFT plots that depict valence band spin splitting at different hole-dopings for monolayer GaSe. n is the hole-doped concentration and n_m is critical hole concentration that leads to a large spin magnetic moment.

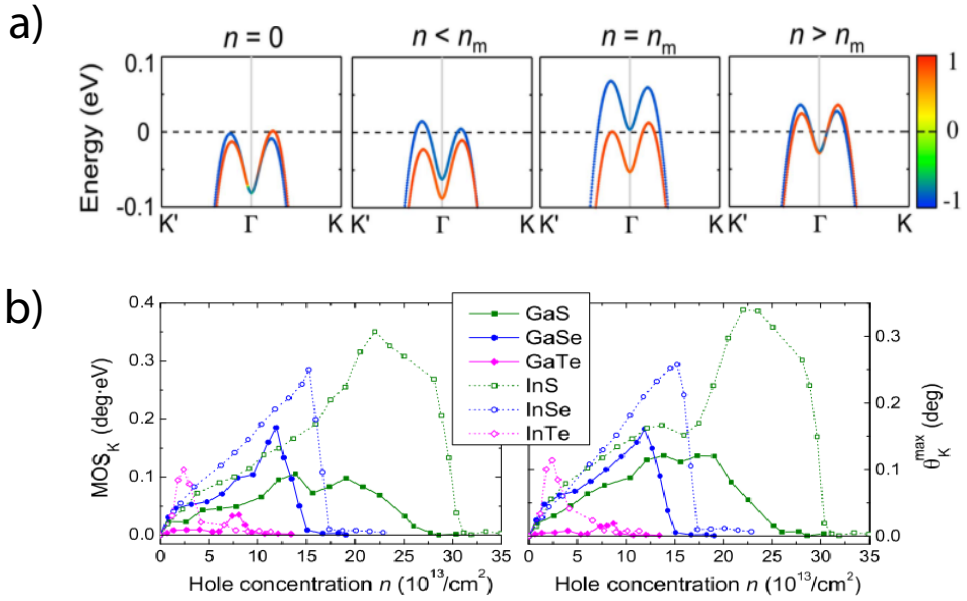

Figure 5.8: a) shows DFT of spin states in the top most valence band for monolayer GaSe. As concentration approaches the critical concentration (n_m), the magnitude of the separation between the two spin states is largest. In b), the theoretical calculations for the strength of the Kerr effect and maximum Kerr angle [53] is shown. Figures reproduced with permission from Ref. [53].

The ability to induce magnetism in III-VI monochalcogenides through doping could ideally be achieved through defects and tuned with electrostatic gating [138]. To measure ferromagnetic behavior, Kerr rotation measurements such as MOKE could be performed (Figure 5.8b). Thus, making it viable to test tunable magnetism in InSe. More importantly, hole-doped InSe may find more value in combination with 2D magnets.

5.2.2 III-VI Monochalcogenide and Chromium Iodide Heterostructure

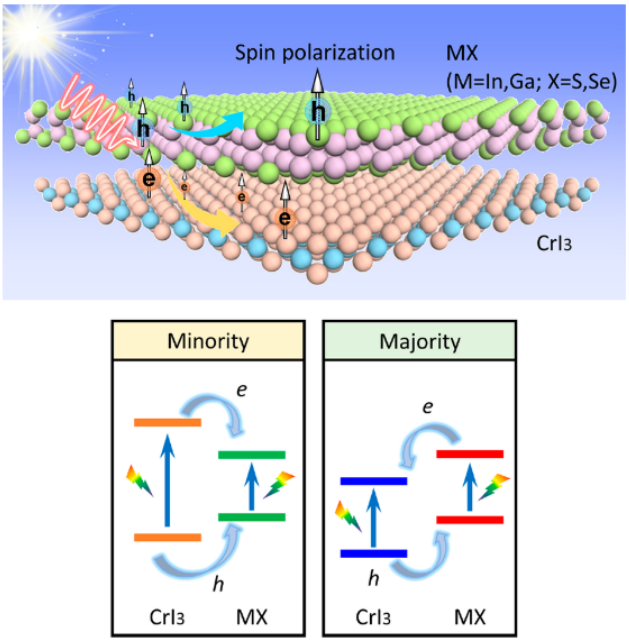

Figure 5.9: The top image is an illustration of MX monolayer and CrI_3 monolayer heterostructure where hole doping occurs in the MX layer due to photoexcitation. The bottom schematic shows the majority and minority spin channels for the predicted type-II band alignment [119]. Figures reproduced with permission from Ref. [119].

In recent work, Ref. [119] considers the pairing of III-VI monochalcogenides with CrI_3. It explores the interplay between strong light-matter coupling and magnetism in a heterostructure composed of these materials. An illustration of a MX/CrI_3 heterostructure is shown in Figure 5.9. Without photoexcitation, CrI_3 induces a small magnetic moment on each chalcogenide atom in MX monolayer. This occurs due to the charge transfer allowed by the type-II band alignment and is complimented by strong orbital hybridization between chalcogenide and iodide atoms. The interplay of these factors suggest that the magnetic moment in MX monolayers should be attributed to the exchange interaction between chalcogenide and iodide atoms. As a result, a minority and

majority spin channel exist at the von Hove singularity [119].

Generation of spin-polarized carriers can occur under optical illumination, causing hole doping into the majority spin channel of the MX monolayer, thereby creating larger spin splitting than without photoexcitation. A consequence that manifests from the separation of holes and electrons by light into the MX and CrI_3 respectively. Thus, photoexcitation can be used to further hole-dope a p-type MX layer. The minority spin channel is homogeneous with or without illumination, contributing equal amounts of electrons and holes to both systems [119]. Since only the majority spin channel is turned ”on”, light can be used as a ’knob’ for magnetism in this 2D structure.

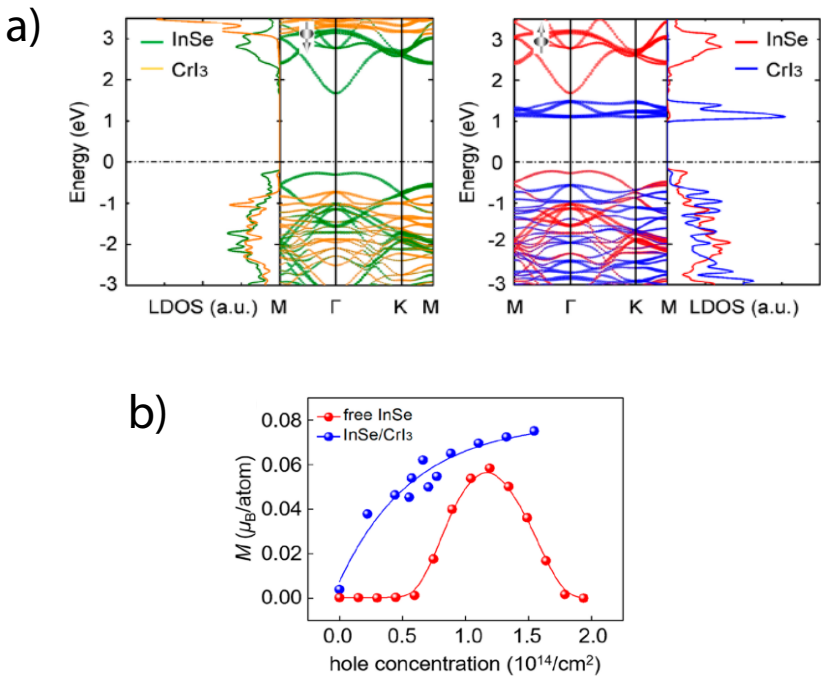

Figure 5.10: a) shows the overlapping DFT band structures for minority (left) and majority (right) channels of monolayer InSe and monolayer CrI_3. The magnetic moment strength as a function of hole concentration for free InSe and InSe/CrI_3 is shown in b). The potential for dynamic magneto-optical control is evident for the heterostructure [119]. Figures reproduced with permission from Ref. [119].

A InSe/CrI_3 heterostucture with predicted qualities are possible due to CrI_3 majority and minority spin channel have energy gaps of 1.61 eV and 4.77 eV, respectively, while monolayer InSe can have band gaps that can range from $\sim$ 2.14 - 3.32 eV. The alignment of these bands can be seen in DFT band structures shown in Figures 5.10a left (minority) and 5.10a right (majority). These predictions should be achievable in experiments. Calculations of magnetic moment generated by hole-doping (Figure 5.10b) show that a smaller hole doping is needed for a sizable magnetization in InSe/CrI_3 than in bare InSe. This is promising, since it could be possible to couple a p-type InSe with CrI_3, therefore providing two knobs to control the hole concentration, light and electrostatic gating. These predictions are enticing and motivate conducting experimental studies to verify these magneto-optical phenomena in a InSe/CrI_3 heterostructure.

5.3 Preliminary Work

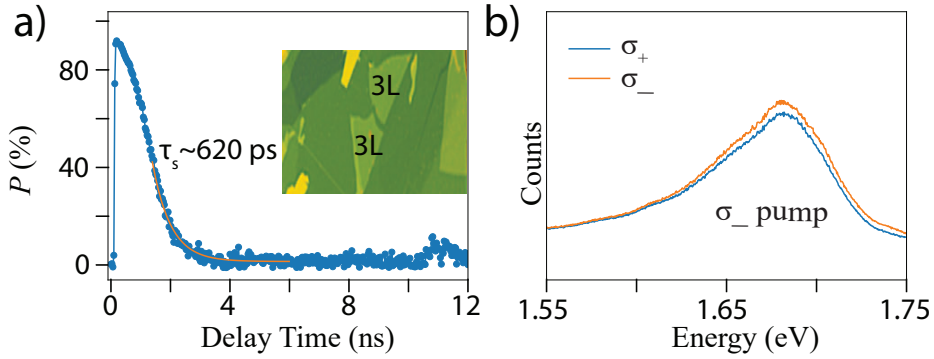

Figure 5.11: a) polarized TRPL for Zn-doped InSe using 1.82 eV laser at 120 μW. The inset is hBN encapsulated 3L InSe. b) shows stead-state polarized PL which behaves as expected.

In the work presented in chapters three and four, n-type InSe was used. However, in light of recent predictions on the novel magneto-optical properties for p-type InSe [52]–[54], this section begins the exploration in a new direction. In the inset of Figure 5.11a, is a hBN encapsulated Zn-doped InSe sample. The Zn-doping makes InSe into a p-type semiconductor. Once again, sam-

ple fabrication was conducted by the Hersam group. In Figures 5.11a and 5.11b, OISO has been observed and similar time dynamics to that of n-type have been measured. These initial measurements confirm that p-type InSe also demonstrates strong coupling between light and excitonic spin similar to what was experimentally demonstrated for n-type InSe in chapter three. These initial characterizations are important as they help motivate future magneto-optical studies with p-type InSe, but this work is still in progress. Therefore it would be premature to make any definitive conclusions about spin dynamics in this system.

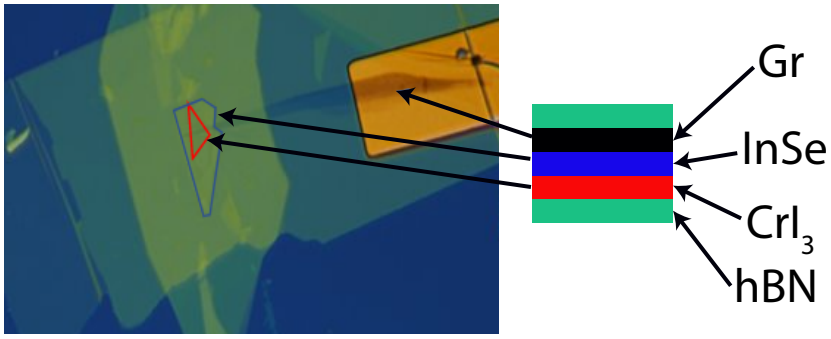

Figure 5.12: The left image is a microscope image of InSe/CrI_3 encapsulated in hBN. The right image is a side-view illustration of the heterostructure. Red is 3L CrI_3, blue is 3L p-type InSe, black is few-layer Gr, and green is hBN. The Gr is used to make good electrical contact with the 3L InSe.

Even so, the next step is clear; pair few-layer p-type InSe with few-layer CrI_3. Recent work with TMDs/CrX_3 [135], [136] and theoretically predictions for MX/CrI_3 [119] provide ample support to pursue this direction. A fully constructed InSe/CrI_3 device can be seen in the left image of Figure 5.12. This was fabricated by the Hersam group to have optimal band gaps between 3L InSe and 3L CrI_3. This should create a type-II band alignment. This heterostructure also contains Gr for a top contact, so that InSe can be electrically gated. By using a gate and photoexcitation, it may be possible to have considerable tuning of the hole concentration, which should affect spin dynamics.

5.4 Future Work

To study optical spin properties in a InSe/CrI_3 heterostructure, the same magneto-optical techniques used in chapters three and four can be applied. Steady-state polarized PL methodology and setup, as described in Chapters 2.3 and 2.5, can be used for a quick check to verify coupling between InSe and CrI_3. It can also be used to quickly check other thickness configurations. Measurement schemes such as polarized TRPL and MOKE, can be used for further exploration of magneto-optical properties in this structure. Polarized TRPL is already described in chapters 2.3 and 2.5. The MOKE setup is shown in Figure 5.13. The basic principal of this method is similar to TRKR except that it is a steady-state measurement and there is only one laser beam. The varied stimuli can be any knob that varies Kerr angle . In traditional polar MOKE, a varied static magnetic field is applied out-of-plane to the sample. The Kerr angle manifests as a response to the real part of the index of refraction changing.

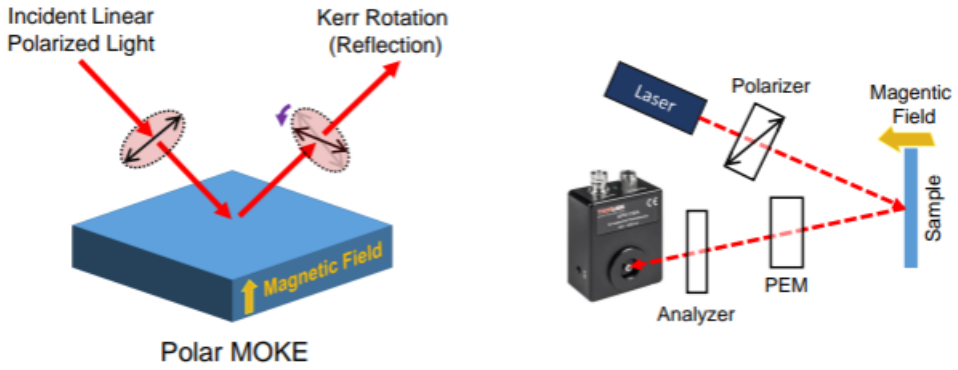

Figure 5.13: Schematic of MOKE setup that could be used to conduct experiments on a InSe/CrI_3 heterostructure. The off angle incident is for visual clarity. In reality, polar MOKE measurements are typically done with a laser at normal incident to the surface. The incident light is linearly polarized at the input, and the reflected beam is passed through a photoelastic modulator (PEM) and analyzer. The intensity signal is then measured by a sensitive photodetector. At the correct frequency of the PEM chopping, the Kerr angle can be extracted from the detected beam. This image was produced by Ref. [139].

Using both polarized TRPL and MOKE, investigations into time dynamics of excitons and sample magnetization, respectively, can be conducted on a InSe/CrI_3 structure. The change of these two characteristics can be tracked by varying incident light intensity and gate voltage [53], [119], as these are two knobs that could potentially be used to tune magneto-optical properties in the heterostructure. MOKE, in particular, can also be used to cross check with theoretical predictions, which estimate the trend of Kerr rotation with increasing hole concentrations.

If interesting physics does not occur in the system portrayed in Figure 5.12, quick and reasonable changes can be made, such as using thinner InSe. A bilayer or monolayer would have increased chances of having a type-II band alignment with CrI_3 [119]. Probing these thickness could be possible by further collaboration with chemistry and material science groups at Northwestern that have lasers with appropriate wavelengths. Overall, this direction is an endeavour that could bear excellent fruits.

CHAPTER 6
CONCLUSION

In this dissertation, thickness and electrical gating are knobs that, in tandem with polarized light (probe and knob), can be used to dynamically control optical spin properties in InSe. The experimental verification of OISO and investigation of g-factor, are perhaps some of the first in-depth layer-dependent studies of fundamental optical spin phenomena in InSe [47], or III-VI monochalcogenides in general. These studies also reveled the prevalence of excitons in the optical orientation process. When these carriers are accounted for, they complicate optical spin dynamics in InSe. For an InSe device with electrical gating capabilities, the optical read-out of spin polarization could be controlled. These studies suggest that the Rashba effect does not drive the change in optical polarization, but scattering caused by increased carrier concentration. In turn, this result reveals that the change in recombination dynamics drives tunability of excitonic optical spin polarization. A detailed description of the physics revealed by these two knobs, thickness and electrical gate, are discussed in chapters three and four respectively. These chapters present pioneering work that contribute to the fundamental understanding of optical spin characteristics in layered InSe. Even though this thesis still leaves some questions unanswered, it provides stepping stones, or building blocks, that will be quintessential for future work on InSe. In fact, in chapter five, this dissertation also lays out a path forward, the next lucrative steps that could fully realize the potential of InSe for 2D spintronics.

6.1 Summary of Key Findings

There are four key findings for InSe in this work; (1) OISO persists from few-layer to multilayer, (2) spin dynamics can be tuned by thickness, (3) excitonic g-factor is $\sim$.2, and (4) applied gate voltages change recombination lifetimes but not spin lifetimes. The first three points are revealed in chapter two, while the last is in chapter three. These four characteristics are foundational to the understanding of how optical spin dynamics in InSe can be controlled.

Based on promising properties such as high electron mobility, nonlinear band gap, quantum hall effect [38], InSe is seen as an exemplary material in the III-VI monochalcogenide family. When considering predictions of polarized optical selection rules as well, InSe becomes an even more intriguing platform for potential spin physics [41], [42]. By establishing experimentally that OISO exists and that it occurs near the Γ point [47], Nelson *et. al* highlight InSe's uniqueness as a van der Waals material, further displaying its difference to TMDs and similarities to III-V and II-VI semiconductors. Also, by conducting a layer-dependent study of optical spin properties in InSe, Nelson *et. al* explicitly connect optical orientation to excitonic dynamics [47]. Definitive proof of excitonic spin dynamics in III-VI monochalcogenide GaSe is shown in the literature [43], [44], [57], but extensive examination of layer-dependence was lacking before work shown in this thesis. From few-layer to bulk InSe, steady-state polarized PL measurements show a rapid decay in P with increasing layer number. Yet, when TRKR was preformed on bulk, OISO still persisted. The explanation lies in a rate model for steady-state polarized PL. The ratio of recombination lifetime to spin lifetime drives the output polarization. When thickness is changed, the DP spin relaxation mechanism is modified by the Dresselhaus effect. Thus, spin lifetimes decrease with increasing layer number, which is reflected in P. Although the rate model, combined with a model for spin relaxation, does not quantitatively describe the P trend, it does qualitatively match

expectations. When applying a magnetic field, $\sim$.2 was measured for $|g_{\perp}^{*}|$, which is far from the expected value of a free electron. Other works predicted $\sim$2 for the effective g-factor [34], [38], but they did not consider excitonic effects. Taking a toy model developed by Ref. [42], excitonic g-factors were calculated for different thicknesses. For thicknesses greater than a bilayer, the excitonic effective g-factor sat below .5. These values are much closer to experimental values. The theoretical calculations from the toy model are supported by *ab-initio* DFT calculations.

In the attempt to harness optical spin polarization in a device, a lateral 4L InSe FET was constructed. The original motivation was found in potentially tuning spin lifetimes in InSe using the Rashba effect [49], [104], [105]. However, this was not observed in time-resolved measurements. Instead, the radiative recombination lifetime changed with electrical gate while spin lifetimes were constant. The conceptual explanation for this phenomena is likely related to the change in carrier scattering rates due to a changing electron carrier concentration. This can also be seen in steady-state PL, where the intensity and width of the emission peak significantly changes with applied gate voltage. A modified excitonic dynamics model for GaSe [111] points out higher momentum states that lead to nonradiative decay. Extrapolating this model to InSe, it can be reasoned that the combined factors of radiative recombination, nonradiative recombination, and excitonic momentum, may be contributing to the changes in PL and TRPL as the gate voltage is varied.

When reviewing these studies, the control of optical spin properties in InSe is strongly related to the manipulation of excitonic dynamics. Therefore, the four findings describe (1) coupling strength of excitonic spin to light, (2) mechanisms of excitonic spin relaxation, (3) coupling strength of excitonic spin to magnetic fields, and (4) mechanisms of excitonic recombination. Understanding these four parameters can aid in the designing of ideal setups that can unlock the potential of excitonic properties in InSe.

6.2 Opportunities for Future Research

Chapters three and four focus on completed work, while chapter five focuses on opportunities for future research. The discovery of van der Waals magnets over five years ago [120], opened a new field of study in 2D materials. It extended the already vast selection of building blocks for layer-by-layer engineering. In particular, CrI_3 has been highlighted in studies due to layer-dependent magnetism, response to external stimuli, and its coupling to valley materials [14], [121]. Recently, it was shown that WSe_2/CrI_3 can have interlayer coupling, where valleys in WSe_2 are split by the effective magnetic field generated from CrI_3, unveiling this heterostructure's potential for future valleytronic devices [135]. This then begs the question: Can we find a similar coupling effect with InSe?

There has been ample theoretical work on tunable magneto-optical effects in hole-doped III-VI monocahlcogenides [52]–[54]. Due to a von Hove singularity in the density of states for the top-most valence band, ferromagnetism can manifests for Fermi-levels that reach this singularity. Yet, the calculated hole concentrations necessary for this transitions has not been observed in real p-type InSe devices [138]. Even so, based on predictions made by Ref. [119], hole-doped InSe may still find utility in $InSe/CrI_3$ heterostructures. Theory implies that InSe could couple to CrI_3, thereby allowing light to control magnetism in this system. Photoexcited carriers generated by light would create large spin splitting between minority and majority spin channels by separating out electrons and holes into CrI_3 and InSe respectively. When reaching a certain level of hole concentration, $InSe/CrI_3$ can generate nonzero magnetic moments more easily than bare InSe [119]. With these predictions as motivation, chapter five gives a brief description of a $InSe/CrI_3$ heterostructure with gating capabilities. Future research is planned for this system.

The opportunities presented by a $InSe/CrI_3$ heterostructure are profound. This could create a

new platform for 2D spintronics. The underlying physics that could be observed is also thrilling. If this structure displays interesting optical spin coupling effects between p-type InSe and CrI_3, there are many interesting research questions that could be pursued. For example: (1) How does the excitonic recombination and spin dynamics behave in such system? (2) To what degree are the excitonic spin lifetimes tunable? (3) Can this be designed to make a rudimentary 2D spintronic device that is optically controllable? All-in-all, this new research direction is promising and could yield a novel 2D system for future spintronic applications.

REFERENCES

[1] T. Haider, "A review of magneto-optic effects and its application," 2017.

[2] E. I. Rashba, "Spintronics: Sources and challenge - Personal perspective," *Journal of Superconductivity and 11el Magnetism*, vol. 15, no. 1, pp. 13–17, 2002.

[3] Y. P. Feng, L. Shen, M. Yang, *et al.*, "Prospects of spintronics based on 2D materials," *Wiley Interdisciplinary Reviews: Computational Molecular Science*, vol. 7, no. 5, e1313, Sep. 2017.

[4] A. Makarov, T. Windbacher, V. Sverdlov, and S. Selberherr, "CMOS-compatible spintronic devices: A review," *Semiconductor Science and Technology*, vol. 31, no. 11, 2016.

[5] I. Žuti ć, J. Fabian, and S. Das Sarma, "Spintronics: Fundamentals and applications," *Rev. Mod. Phys.*, vol. 76, pp. 323–410, 2 Apr. 2004.

[6] S. A. Crooker, M. Furis, X. Lou, *et al.*, "Optical and electrical spin injection and spin transport in hybrid Fe/GaAs devices," *Journal of Applied Physics*, vol. 101, no. 8, pp. 1–6, 2007.

[7] M. Kroutvar, Y. Ducommun, D. Heiss, *et al.*, "Optically programmable electron spin memory using semiconductor quantum dots," *Nature*, vol. 432, no. 7013, pp. 81–84, Nov. 2004.

[8] A. Greilich, D. R. Yakovlev, A. Shabaev, *et al.*, "Mode locking of electron spin coherences in singly charged quantum dots," *Science*, vol. 313, no. 5785, pp. 341–345, 2006.

[9] C. Tan, J. Chen, X.-J. Wu, and H. Zhang, "Epitaxial growth of hybrid nanostructures," *Nature Reviews Materials*, vol. 3, no. 2, pp. 1–13, 2018.

[10] J. Jadwiszczak, J. Sherman, D. Lynall, *et al.*, "Mixed-dimensional 1d/2d van der waals heterojunction diodes and transistors in the atomic limit," *ACS nano*, vol. 16, no. 1, pp. 1639–1648, 2022.

[11] K. S. Novoselov, A. K. Geim, S. V. Morozov, *et al.*, "Electric field effect in atomically thin carbon films," 2004, p. 3824.

[12] A. K. Geim and I. V. Grigorieva, "Van der Waals heterostructures," *Nature*, vol. 499, no. 7459, pp. 419–425, 2013. arXiv: 1307.6718.

[13] T. LaMountain, E. J. Lenferink, Y.-J. Chen, T. K. Stanev, and N. P. Stern, "Environmental engineering of transition metal dichalcogenide optoelectronics," *Frontiers of Physics*, vol. 13, pp. 1–32, 2018.

[14] X. Jiang, Q. Liu, J. Xing, *et al.*, "Recent progress on 2d magnets: Fundamental mechanism, structural design and modification," *Applied Physics Reviews*, vol. 8, 3 Sep. 2021.

[15] Y. Li, J.-K. Qin, C.-Y. Xu, *et al.*, "Electric field tunable interlayer relaxation process and interlayer coupling in wse2/graphene heterostructures," *Advanced Functional Materials*, vol. 26, no. 24, pp. 4319–4328, 2016.

[16] W. Feng, W. Zheng, W. Cao, and P. Hu, "Back Gated Multilayer InSe Transistors with Enhanced Carrier Mobilities via the Suppression of Carrier Scattering from a Dielectric Interface," *Advanced Materials*, vol. 26, no. 38, pp. 6587–6593, 2014.

[17] W. Han, K. M. McCreary, K. Pi, *et al.*, "Spin transport and relaxation in graphene," *Journal of Magnetism and Magnetic Materials*, vol. 324, no. 4, pp. 369–381, 2012.

[18] J. Rioux and G. Burkard, "Photoinduced pure spin-current injection in graphene with Rashba spin-orbit interaction," *Physical Review B - Condensed Matter and Materials Physics*, vol. 90, no. 3, pp. 1–6, 2014. arXiv: 1405.7174.

[19] M. Gmitra, S. Konschuh, C. Ertler, C. Ambrosch-Draxl, and J. Fabian, "Band-structure topologies of graphene: Spin-orbit coupling effects from first principles," *Physical Review B - Condensed Matter and Materials Physics*, vol. 80, no. 23, pp. 1–5, 2009. arXiv: 0904.3315.

[20] H. Zeng, J. Dai, W. Yao, D. Xiao, and X. Cui, "Valley polarization in MoS 2 monolayers by optical pumping," *Nature Nanotechnology*, vol. 7, no. 8, pp. 490–493, 2012. arXiv: 1202.1592.

[21] K. F. Mak, K. He, J. Shan, and T. F. Heinz, "Control of valley polarization in monolayer MoS2 by optical helicity," *Nature Nanotechnology*, vol. 7, no. 8, pp. 494–498, 2012. eprint: 1205.1822.

[22] Z. Ye, D. Sun, and T. Heinz, "Optical manipulation of valley pseudospin," *Nature Physics*, vol. 13, no. 1, pp. 26–29, 2017.

[23] K. F. Mak, K. L. McGill, J. Park, and P. L. McEuen, "The valley hall effect in MoS2 transistors," *Science*, vol. 344, no. 6191, pp. 1489–1492, 2014. arXiv: 1403.5039.

[24] P. Dey, L. Yang, C. Robert, *et al.*, "Gate-Controlled Spin-Valley Locking of Resident Carriers in WSe2 Monolayers," *Physical Review Letters*, vol. 119, no. 13, p. 137 401, Sep. 2017. arXiv: 1704.05448.

[25] T. LaMountain, J. Nelson, E. J. Lenferink, *et al.*, "Valley-selective optical stark effect of exciton-polaritons in a monolayer semiconductor," *Nature communications*, vol. 12, no. 1, p. 4530, 2021.

[26] F. Quochi, G. Bongiovanni, A. Mura, *et al.*, "Strongly driven semiconductor microcavities: From the polariton doublet to an ac stark triplet," *Physical review letters*, vol. 80, no. 21, p. 4733, 1998.

[27] A. Hayat, C. Lange, L. A. Rozema, *et al.*, "Dynamic stark effect in strongly coupled microcavity exciton polaritons," *Physical Review Letters*, vol. 109, no. 3, p. 033 605, 2012.

[28] C. Lange, E. Cancellieri, D. Panna, *et al.*, "Ultrafast control of strong light–matter coupling," *New Journal of Physics*, vol. 20, no. 1, p. 013 032, 2018.

[29] D. Panna, N. Landau, L. Gantz, *et al.*, "Ultrafast manipulation of a strongly coupled light–matter system by a giant ac stark effect," *ACS Photonics*, vol. 6, no. 12, pp. 3076–3081, 2019.

[30] A. A. Mitioglu, P. Plochocka, Granados Del Aguila, *et al.*, "Optical Investigation of Monolayer and Bulk Tungsten Diselenide (WSe2) in High Magnetic Fields," *Nano Letters*, vol. 15, no. 7, pp. 4387–4392, 2015. arXiv: 1506.03905.

[31] G. Plechinger, P. Nagler, A. Arora, *et al.*, "Excitonic Valley Effects in Monolayer WS2 under High Magnetic Fields," *Nano Letters*, vol. 16, no. 12, pp. 7899–7904, 2016. arXiv: 1612.03004.

[32] T. T. Mnatsakanov, M. E. Levinshtein, L. I. Pomortseva, and S. N. Yurkov, "Universal Analytical Approximation of the Carrier Mobility in Semiconductors for a Wide Range of Temperatures and Doping Densities," *Semiconductors*, vol. 38, no. 1, pp. 56–60, 2004.

[33] M. Oestreich, M. Bender, J. Hubner, *et al.*, "Spin injection , spin transport and spin coherence," *Online*, vol. 285, 2002.

[34] P. Li and I. Appelbaum, "Symmetry, distorted band structure, and spin-orbit coupling of group-iii metal-monochalcogenide monolayers," *Phys. Rev. B*, vol. 92, p. 195 129, 19 Nov. 2015.

[35] D. T. Do, S. D. Mahanti, and C. W. Lai, "Spin splitting in 2D monochalcogenide semiconductors," *Scientific Reports*, vol. 5, no. 1, p. 17 044, Dec. 2015.

[36] K. Premasiri and X. P. Gao, "Tuning spin-orbit coupling in 2D materials for spintronics: A topical review," *Journal of Physics Condensed Matter*, vol. 31, no. 19, 2019.

[37] C. Song, S. Huang, C. Wang, J. Luo, and H. Yan, "The optical properties of few-layer InSe," *Journal of Applied Physics*, vol. 128, no. 6, 2020. arXiv: 2008.04691.

[38] D. A. Bandurin, A. V. Tyurnina, G. L. Yu, *et al.*, "High electron mobility, quantum Hall effect and anomalous optical response in atomically thin InSe," *Nature Nanotechnology*, vol. 12, no. 3, pp. 223–227, Mar. 2017.

[39] T. Venanzi, H. Arora, S. Winnerl, *et al.*, "Photoluminescence dynamics in few-layer inse," *Phys. Rev. Materials*, vol. 4, p. 044 001, 4 Apr. 2020.

[40] T. V. Shubina, W. Desrat, M. Moret, *et al.*, "InSe as a case between 3D and 2D layered crystals for excitons," *Nature Communications*, vol. 10, no. 1, pp. 1–8, 2019. arXiv: 1904.00390.

[41] S. J. Magorrian, V. Zólyomi, and V. I. Fal'ko, "Electronic and optical properties of two-dimensional inse from a dft-parametrized tight-binding model," *Phys. Rev. B*, vol. 94, p. 245 431, 24 Dec. 2016.

[42] S. J. Magorrian, V. Zólyomi, and V. I. Fal'ko, "Spin-orbit coupling, optical transitions, and spin pumping in monolayer and few-layer InSe," *Physical Review B*, vol. 96, no. 19, p. 195 428, Nov. 2017. arXiv: 1711.03402.

[43] E. Gamarts, E. Ivchenko, M. Karaman, *et al.*, "Optical orientation and alignment of free excitons in GaSe during resonance excitation. Experiment," *Soviet Journal of Experimental and Theoretical Physics*, vol. 46, no. 3, p. 590, 1977.

[44] Y. Tang, W. Xie, K. C. Mandal, J. A. McGuire, and C. W. Lai, "Optical and spin polarization dynamics in GaSe nanoslabs," *Phys. Rev. B*, vol. 91, p. 195 429, 19 May 2015.

[45] H. Arora and A. Erbe, "Recent progress in contact, mobility, and encapsulation engineering of InSe and GaSe," *InfoMat*, vol. 3, no. 6, pp. 662–693, 2021.

[46] D. J. Late, B. Liu, J. Luo, *et al.*, "Gas and gase ultrathin layer transistors," *Advanced Materials*, vol. 24, no. 26, pp. 3549–3554, 2012.

[47] J. Nelson, T. K. Stanev, D. Lebedev, *et al.*, "Layer-dependent optically induced spin polarization in inse," *Phys. Rev. B*, vol. 107, p. 115 304, 11 Mar. 2023.

[48] C. Ren, S. Wang, H. Tian, *et al.*, "First-principles investigation on electronic properties and band alignment of group iii monochalcogenides," *Scientific Reports*, vol. 9, 1 Dec. 2019.

[49] A. Ceferino, S. J. Magorrian, V. Zólyomi, *et al.*, "Tunable spin-orbit coupling in two-dimensional inse," *Phys. Rev. B*, vol. 104, p. 125 432, 12 Sep. 2021.

[50] L. Liu, L. Wu, A. Wang, *et al.*, "Ferroelectric-Gated InSe Photodetectors with High On/Off Ratios and Photoresponsivity," *Nano Letters*, vol. 20, no. 9, pp. 6666–6673, 2020.

[51] T. Zheng, Z. T. Wu, H. Y. Nan, *et al.*, "Layer-number dependent and structural defect related optical properties of InSe," *RSC Advances*, vol. 7, no. 87, pp. 54 964–54 968, 2017.

[52] T. Cao, Z. Li, and S. G. Louie, "Tunable magnetism and half-metallicity in hole-doped monolayer gase," *Phys. Rev. Lett.*, vol. 114, p. 236 602, 23 Jun. 2015.

[53] W. Feng, G.-Y. Guo, and Y. Yao, "Tunable magneto-optical effects in hole-doped group-iiia metal-monochalcogenide monolayers," *2D Materials*, vol. 4, no. 1, p. 015 017, 2016.

[54] F. Li, X. Zhou, W. Feng, B. Fu, and Y. Yao, "Thickness-dependent magneto-optical effects in hole-doped gas and gase multilayers: A first-principles study," *New Journal of Physics*, vol. 20, no. 4, p. 043 048, 2018.

[55] M. Houssa, R. Meng, K. Iordanidou, G. Pourtois, V. Afanas' ev, and A. Stesmans, "Doping-induced ferromagnetism in inse and sno monolayers," *Journal of Computational Electronics*, vol. 20, pp. 88–94, 1 2021.

[56] S. Zhao, X. Li, B. Dong, *et al.*, "Valley manipulation in monolayer transition metal dichalcogenides and their hybrid systems: Status and challenges," *Reports on Progress in Physics*, vol. 84, no. 2, 2021.

[57] E. Ivchenko, G. Pikus, B. Razbirin, and A. Starukhin, "Optical orientation and alignment of free excitons in GaSe during resonance excitation. Theory," *Soviet Journal of Experimental and Theoretical Physics*, vol. 45, no. 6, p. 1172, 1977.

[58] N. Kuroda, I. Munakata, and Y. Nishina, "Exciton transitions from spin-orbit split off valence bands in layer compound inse," *Solid State Communications*, vol. 33, no. 6, pp. 687–691, 1980.

[59] M. Brotons-Gisbert, R. Proux, R. Picard, *et al.*, "Out-of-plane orientation of luminescent excitons in two-dimensional indium selenide," *Nature Communications*, vol. 10, no. 1, pp. 1–10, 2019.

[60] M. Faraday, "I. experimental researches in electricity.—nineteenth series," *Philosophical Transactions of the Royal Society of London*, no. 136, pp. 1–20, 1846.

[61] R. W. Wood and A. Ellett, "On the influence of magnetic fields on the polarisation of resonance radiation," *Proceedings of The Royal Society A: Mathematical, Physical and Engineering Sciences*, vol. 103, pp. 396–403, 1923.

[62] W. Hanle, "Über eine anomalie bei der polarisation der ramanstrahlung," *Naturwissenschaften*, vol. 19, no. 18, pp. 375–375, 1931.

[63] A. Kastler, "Optical methods of atomic orientation and of magnetic resonance," *JOSA*, vol. 47, no. 6, pp. 460–465, 1957.

[64] R. Parsons, "Band-to-band optical pumping in solids and polarized photoluminescence," *Physical Review Letters*, vol. 23, no. 20, p. 1152, 1969.

[65] D. Press, T. D. Ladd, B. Zhang, and Y. Yamamoto, "Complete quantum control of a single quantum dot spin using ultrafast optical pulses," *Nature*, vol. 456, no. 7219, pp. 218–221, 2008.

[66] I. A. Yugova, A. Greilich, D. R. Yakovlev, *et al.*, "Universal behavior of the electron g factor in $\mathrm{GaAs}/\mathrm{Al}_x\mathrm{Ga}_{1-x}\mathrm{As}$ quantum wells," *Phys. Rev. B*, vol. 75, p. 245 302, 24 Jun. 2007.

[67] C. L. Yang, J. Dai, W. K. Ge, and X. Cui, "Determination of the sign of g factors for conduction electrons using time-resolved Kerr rotation," *Applied Physics Letters*, vol. 96, no. 15, pp. 1–4, 2010.

[68] J. H. Buß, T. Schupp, D. J. As, D. Hägele, and J. Rudolph, "Temperature dependence of the electron Landé g -factor in cubic GaN," *Journal of Applied Physics*, vol. 118, no. 22, p. 225 701, Dec. 2015.

[69] L. Yang, W. Chen, K. M. McCreary, B. T. Jonker, J. Lou, and S. A. Crooker, "Spin Coherence and Dephasing of Localized Electrons in Monolayer MoS 2," *Nano Letters*, vol. 15, no. 12, pp. 8250–8254, Dec. 2015. arXiv: 1511.03255.

[70] E. J. McCormick, M. J. Newburger, Y. K. Luo, *et al.*, "Imaging spin dynamics in monolayer WS 2 by time-resolved Kerr rotation microscopy," *2D Materials*, vol. 5, no. 1, p. 011 010, Nov. 2017. arXiv: 1602.03568.

[71] C. R. Zhu, K. Zhang, M. Glazov, *et al.*, "Exciton valley dynamics probed by kerr rotation in WSe_2 monolayers," *Phys. Rev. B*, vol. 90, p. 161 302, 16 Oct. 2014.

[72] T. LaMountain, H. Bergeron, I. Balla, T. K. Stanev, M. C. Hersam, and N. P. Stern, "Valley-selective optical stark effect probed by kerr rotation," *Phys. Rev. B*, vol. 97, p. 045 307, 4 Jan. 2018.

[73] L. Shi, Q. Zhou, Y. Zhao, *et al.*, "Oxidation mechanism and protection strategy of ultrathin indium selenide: Insight from theory," *The journal of physical chemistry letters*, vol. 8, no. 18, pp. 4368–4373, 2017.

[74] A. A. Kistanov, Y. Cai, K. Zhou, S. V. Dmitriev, and Y.-W. Zhang, "Atomic-scale mechanisms of defect- and light-induced oxidation and degradation of inse," *J. Mater. Chem. C*, vol. 6, pp. 518–525, 3 2018.

[75] L. Wang, I. Meric, P. Y. Huang, *et al.*, "One-dimensional electrical contact to a two-dimensional material," *Science*, vol. 342, no. 6158, pp. 614–617, 2013.

[76] D. G. Hopkinson, V. Zólyomi, A. P. Rooney, *et al.*, "Formation and Healing of Defects in Atomically Thin GaSe and InSe," *ACS Nano*, vol. 13, no. 5, pp. 5112–5123, 2019.

[77] J. Kang, S. A. Wells, V. K. Sangwan, *et al.*, "Solution-Based Processing of Optoelectronically Active Indium Selenide," *Advanced Materials*, vol. 30, no. 38, p. 1 802 990, Sep. 2018.

[78] S. A. Wells, A. Henning, J. T. Gish, V. K. Sangwan, L. J. Lauhon, and M. C. Hersam, "Suppressing Ambient Degradation of Exfoliated InSe Nanosheet Devices via Seeded Atomic Layer Deposition Encapsulation," *Nano Letters*, vol. 18, no. 12, pp. 7876–7882, 2018.

[79] Q. Hao, H. Yi, H. Su, *et al.*, "Phase Identification and Strong Second Harmonic Generation in Pure ϵ-InSe and Its Alloys," *Nano Letters*, vol. 19, no. 4, pp. 2634–2640, 2019.

[80] W. Huang, L. Gan, H. Li, Y. Ma, and T. Zhai, "Phase-Engineered Growth of Ultrathin InSe Flakes by Chemical Vapor Deposition for High-Efficiency Second Harmonic Generation," *Chemistry - A European Journal*, vol. 24, no. 58, pp. 15 678–15 684, 2018.

[81] J. F. Sánchez-Royo, G. Muñoz-Matutano, M. Brotons-Gisbert, *et al.*, "Electronic structure, optical properties, and lattice dynamics in atomically thin indium selenide flakes," *Nano Research*, vol. 7, no. 10, pp. 1556–1568, 2014.

[82] M. Wu, Q. Xie, Y. Wu, *et al.*, "Crystal structure and optical performance in bulk γ-InSe single crystals," *AIP Advances*, vol. 9, no. 2, p. 025 013, Feb. 2019.

[83] S. R. Tamalampudi, R. Sankar, H. Apostoleris, *et al.*, "Thickness-Dependent Resonant Raman and E' Photoluminescence Spectra of Indium Selenide and Indium Selenide/Graphene Heterostructures," *Journal of Physical Chemistry C*, vol. 123, no. 24, pp. 15 345–15 353, 2019.

[84] M. R. Molas, A. V. Tyurnina, V. Z-lyomi, *et al.*, "Raman spectroscopy of GaSe and InSe post-transition metal chalcogenides layers," *arXiv*, pp. 1–8, 2020.

[85] D. V. Rybkovskiy, A. V. Osadchy, and E. D. Obraztsova, "Transition from parabolic to ring-shaped valence band maximum in few-layer gas, gase, and inse," *Phys. Rev. B*, vol. 90, p. 235 302, 23 Dec. 2014.

[86] I. A. Kibirev, A. V. Matetskiy, A. V. Zotov, and A. A. Saranin, "Thickness-dependent transition of the valence band shape from parabolic to Mexican-hat-like in the MBE grown InSe ultrathin films," *Applied Physics Letters*, vol. 112, no. 19, May 2018.

[87] F. Meier and B. P. Zakharchenya, Eds., *Optical Orientation*. Amsterdam: North-Holland Physics Publishing, 1984.

[88] S. Takasuna, J. Shiogai, S. Matsuzaka, M. Kohda, Y. Oyama, and J. Nitta, "Weak antilocalization induced by rashba spin-orbit interaction in layered iii-vi compound semiconductor gase thin films," *Phys. Rev. B*, vol. 96, p. 161 303, 16 Oct. 2017.

[89] G. Wang, L. Bouet, M. M. Glazov, *et al.*, "Magneto-optics in transition metal diselenide monolayers," *2D Materials*, vol. 2, no. 3, 2015. arXiv: 1503.04105.

[90] C. Hermann and C. Weisbuch, "k • p perturbation theory in III-V compounds and alloys: a reexamination," *Physical Review B*, vol. 15, no. 2, pp. 823–833, Jan. 1977.

[91] J. Förste, N. V. Tepliakov, S. Y. Kruchinin, *et al.*, "Exciton g-factors in monolayer and bilayer wse_2 from experiment and theory," *Nat. Commun.*, vol. 112, p. 4539, 2020.

[92] T. Woźniak, P. E. F. Junior, G. Seifert, A. Chaves, and J. Kunstmann, "Exciton g factors of van der waals heterostructures from first-principles calculations," *Phys. Rev. B*, vol. 101, p. 235 408, 2020.

[93] T. Deilmann, P. Krüger, and M. Rohlfing, "Ab initio studies of exciton g factors: Monolayer transition metal dichalcogenides in magnetic fields," *Phys. Rev. Lett.*, vol. 124, p. 226 402, 2020.

[94] F. Xuan and S. Y. Quek, "Valley zeeman effect and landau levels in two-dimensional transition metal dichalcogenides," *Phys. Rev. Research*, vol. 2, p. 033 256, 2020.

[95] X. Yao and X. Zhang, "Electronic structures of twisted bilayer inse/inse and heterobilayer graphene/inse," *ACS Omega*, vol. 6, p. 13 426, 2021.

[96] M. Förg, A. S. Baimuratov, S. Y. Kruchinin, *et al.*, "Moiré excitons in mose2-wse2 heterobilayers and heterotrilayers," *Nat. Commun.*, vol. 12, p. 1656, 2021.

[97] L. M. Roth, B. Lax, and S. Zwerdling, "Theory of optical magneto-absorption effects in semiconductors," *Phys. Rev.*, vol. 114, p. 90, 1959.

[98] D. Xiao, M.-C. Chang, and Q. Niu, "Berry phase effects on electronic properties," *Rev. Mod. Phys.*, vol. 82, p. 1959, 2010.

[99] J. P. Perdew, K. Burke, and M. Ernzerhof, "Generalized gradient approximation made simple," *Phys. Rev. Lett.*, vol. 77, pp. 3865–3868, 18 Oct. 1996.

[100] P. Giannozzi, S. Baroni, N. Bonini, *et al.*, "Quantum espresso: A modular and open-source software project for quantum simulations of materials," *J. Phys.: Condens. Matter*, vol. 21, p. 395 502, 2009.

[101] M. Burkatzki, C. Filippi, and M. Dolg, "Energy-consistent pseudopotentials for quantum monte carlo calculations," *J. Chem. Phys.*, vol. 126, p. 234 105, 2007.

[102] M. Burkatzki, C. Filippi, and M. Dolg, "Energy-consistent small-core pseudopotentials for 3d-transition metals adapted to quantum monte carlo calculations," *J. Chem. Phys.*, vol. 129, p. 164 115, 2008.

[103] S. Grimme, J. Antony, S. Ehrlich, and H. Krieg, "A consistent and accurate ab initio parametrization of density functional dispersion correction (dft-d) for the 94 elements h-pu," *J. Chem. Phys.*, vol. 132, p. 154 104, 2010.

[104] K. Premasiri, S. K. Radha, S. Sucharitakul, *et al.*, "Tuning Rashba Spin-Orbit Coupling in Gated Multilayer InSe," *Nano Letters*, vol. 18, no. 7, pp. 4403–4408, 2018.

[105] J. Zeng, S.-J. Liang, A. Gao, *et al.*, "Gate-tunable weak antilocalization in a few-layer inse," *Phys. Rev. B*, vol. 98, p. 125 414, 12 Sep. 2018.

[106] A. Manchon, H. C. Koo, J. Nitta, S. M. Frolov, and R. A. Duine, "New perspectives for rashba spin–orbit coupling," *Nature materials*, vol. 14, no. 9, pp. 871–882, 2015.

[107] Y. Zhang, X. Sun, K. Jia, *et al.*, "Enhancement of Inse field-effect-transistor performance against degradation of Inse film in air environment," *Nanomaterials*, vol. 11, no. 12, pp. 1–7, 2021.

[108] Q. Hao, J. Liu, G. Wang, *et al.*, "Surface-Modified Ultrathin InSe Nanosheets with Enhanced Stability and Photoluminescence for High-Performance Optoelectronics," *ACS Nano*, vol. 14, no. 9, pp. 11 373–11 382, 2020.

[109] V. K. Khanna, "Carrier lifetimes and recombination-generation mechanisms in semiconductor device physics," *European Journal of Physics*, vol. 25, no. 2, pp. 221–237, 2004.

[110] W. Gerlach, H. D. Schlangenotto, and H. F. Maeder, "On the radiative recombination rate in silicon," *Physica Status Solidi (a)*, vol. 13, pp. 277–283, 1972.

[111] Y. Tang, W. Xie, K. C. Mandal, J. A. McGuire, and C. W. Lai, "Exciton spin dynamics in GaSe," *Journal of Applied Physics*, vol. 118, pp. 1–8, 11 2015.

[112] A. Vinattieri, J. Shah, T. C. Damen, *et al.*, "Exciton dynamics in gaas quantum wells under resonant excitation," 1994, pp. 15–1994.

[113] C. Zhong, V. K. Sangwan, J. Kang, J. Luxa, M. C. Hersam, and E. A. Weiss, "Hot Carrier and Surface Recombination Dynamics in Layered InSe Crystals," *J. Phys. Chem. Lett*, vol. 10, p. 499, 2019.

[114] B. V. Olson, E. A. Kadlec, J. K. Kim, *et al.*, "Intensity- and temperature-dependent carrier recombination in $\mathrm{InAs}/\mathrm{InAs}_{1-x}\mathrm{Sb}_x$ type-ii superlattices," *Phys. Rev. Appl.*, vol. 3, p. 044 010, 4 Apr. 2015.

[115] E. Kioupakis, Q. Yan, D. Steiauf, and C. G. Van de Walle, "Temperature and carrier-density dependence of auger and radiative recombination in nitride optoelectronic devices," *New Journal of Physics*, vol. 15, no. 12, p. 125 006, 2013.

[116] L. Wu, J. Shi, Z. Zhou, *et al.*, "Inse/hbn/graphite heterostructure for high-performance 2d electronics and flexible electronics," *Nano Research*, vol. 13, pp. 1127–1132, 2020.

[117] Z. Zhou, L. Wu, J. Chen, *et al.*, "Electrostatic gating of solid-ion-conductor on inse flakes and inse/h-bn heterostructures," *Chinese Physics B*, vol. 29, no. 11, p. 118 501, 2020.

[118] Y. Lin, C. Zhang, L. Guan, Z. Sun, and J. Tao, "The magnetic proximity effect induced large valley splitting in 2d inse/fei2 heterostructures," *Nanomaterials*, vol. 10, no. 9, p. 1642, 2020.

[119] N. Liu, S. Zhou, and J. Zhao, "Photoinduced Spin Injection and Ferromagnetism in 2D Group III Monochalcogenides," *The Journal of Physical Chemistry Letters*, vol. 13, no. 2, pp. 590–597, 2022.

[120] B. Huang, G. Clark, E. Navarro-Moratalla, *et al.*, "Layer-dependent ferromagnetism in a van der waals crystal down to the monolayer limit," *Nature*, vol. 546, pp. 270–273, 7657 Jun. 2017.

[121] K. S. Burch, D. Mandrus, and J. G. Park, "Magnetism in two-dimensional van der waals materials," *Nature*, vol. 563, pp. 47–52, 7729 Nov. 2018.

[122] S. Yang, T. Zhang, and C. Jiang, "Van der waals magnets: Material family, detection and modulation of magnetism, and perspective in spintronics," *Advanced Science*, vol. 8, 2 Jan. 2021.

[123] M. Gibertini, M. Koperski, A. F. Morpurgo, and K. S. Novoselov, "Magnetic 2d materials and heterostructures," *Nature Nanotechnology*, vol. 14, pp. 408–419, 5 May 2019.

[124] K. S. Novoselov, A. Mishchenko, A. Carvalho, and A. H. C. Neto, "2d materials and van der waals heterostructures," *Science*, vol. 353, 6298 Jul. 2016.

[125] N. D. Mermin and H. Wagner, "Absence of ferromagnetism or antiferromagnetism in one- or two-dimensional isotropic heisenberg models," *Phys. Rev. Lett.*, vol. 17, pp. 1133–1136, 22 Nov. 1966.

[126] R. B. Griffiths, "Peierls proof of spontaneous magnetization in a two-dimensional ising ferromagnet," *Phys. Rev.*, vol. 136, A437–A439, 2A Oct. 1964.

[127] D. L. Cortie, G. L. Causer, K. C. Rule, H. Fritzsche, W. Kreuzpaintner, and F. Klose, "Two-dimensional magnets: Forgotten history and recent progress towards spintronic applications," *Advanced Functional Materials*, vol. 30, 18 May 2020.

[128] T. Li, S. Jiang, N. Sivadas, *et al.*, "Pressure-controlled interlayer magnetism in atomically thin cri3," *Nature Materials*, vol. 18, pp. 1303–1308, 12 Dec. 2019.

[129] K. F. Mak, J. Shan, and D. C. Ralph, "Probing and controlling magnetic states in 2d layered magnetic materials," *Nature Reviews Physics*, vol. 1, no. 11, pp. 646–661, 2019.

[130] H. H. Kim, B. Yang, S. Tian, *et al.*, "Tailored tunnel magnetoresistance response in three ultrathin chromium trihalides," *Nano Letters*, vol. 19, pp. 5739–5745, 8 Aug. 2019.

[131] C. Jin, Z. Tao, K. Kang, *et al.*, "Imaging and control of critical fluctuations in two-dimensional magnets," *Nature Materials*, vol. 19, no. 12, pp. 1290–1294, 2020.

[132] J. L. Lado and J. Fernández-Rossier, "On the origin of magnetic anisotropy in two dimensional cri3," *2D Materials*, vol. 4, 3 Sep. 2017.

[133] S. Jiang, J. Shan, and K. F. Mak, "Electric-field switching of two-dimensional van der waals magnets," *Nature Materials*, vol. 17, pp. 406–410, 5 2018.

[134] D. Zhong, K. L. Seyler, X. Linpeng, *et al.*, "Van der Waals engineering of ferromagnetic semiconductor heterostructures for spin and valleytronics," *Science Advances*, vol. 3, no. 5, pp. 1–7, 2017. arXiv: 1704.00841.

[135] D. Zhong, K. L. Seyler, X. Linpeng, *et al.*, "Layer-resolved magnetic proximity effect in van der Waals heterostructures," *Nature Nanotechnology*, vol. 15, no. 3, pp. 187–191, 2020. arXiv: 2001.03861.

[136] T. P. Lyons, D. Gillard, A. Molina-Sánchez, *et al.*, "Interplay between spin proximity effect and charge-dependent exciton dynamics in MoSe2/CrBr3 van der Waals heterostructures," *Nature Communications*, vol. 11, no. 1, 2020. arXiv: 2004.04073.

[137] W. Hu and J. Yang, "Two-dimensional van der Waals heterojunctions for functional materials and devices," *Journal of Materials Chemistry C*, vol. 5, no. 47, pp. 12 289–12 297, 2017.

[138] Z. Guo, R. Cao, H. Wang, *et al.*, "High-performance polarization-sensitive photodetectors on two-dimensional β-inse," *National Science Review*, vol. 9, no. 5, nwab098, 2022.

[139] T. K. Stanev, "Engineering low-dimensional layered structures," *Northwestern University*,

CONTROLLING MAGNETO-OPTICAL PROPERTIES IN 2D INSE

Defense Committee:

Nathaniel P. Stern
Physics and Astronomy
Evanston

Mark C. Hersam
Material Science and Engineering
Evanston

Pedram Khalili
Electrical and Computer Engineering
Evanston

APPENDIX A

MATHEMATICA CALCULATIONS

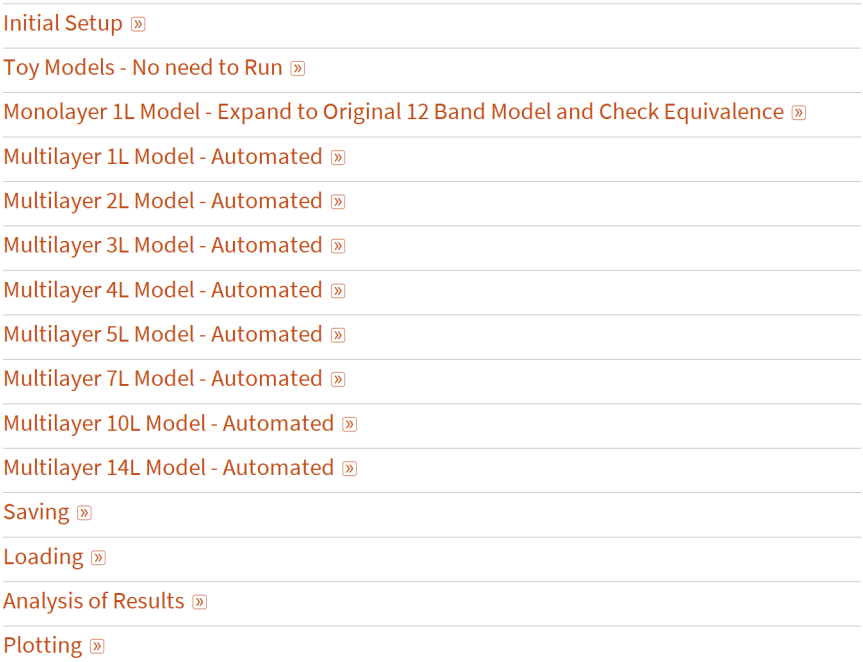

Figure A.1: Different sections of the *Mathematica* code, ”InSe g-factor calculation - Perturbation Theory”.

To perform g-factor calculations using the InSe toy model, *Quantum Notation*, created by José Gómez-Muñóz for quantum calculations in Dirac bra-ket notation, was used as an add-on to *Wolfram Mathematica*. The title of the *Mathematica* script used for these calculations is ”InSe g-factor calculation - Perturbation Theory” and was written by Nathaniel P. Stern. It uses the parameters and formulation found in Ref. [42] to calculate optical spin properties in InSe. The most recent edition of this code is v5: 10/20/2021. The main sections of the code can be seen in Figure A.1.

A.1 Initial Setup and Toy Models

"Initial Setup" defines parameters and matrices needed to construct the monolayer Hamiltonian for InSe at the Γ point as shown in Ref. [42]. This involves creating arrays with appropriate parameters and constructing spin and orbital matrices, which are converted into proper Dirac notation (Figure A.2).

```
Spin2 = MatrixToDirac[PauliMatrix[2], {2}, {1_î → -1/2_μ̂, 0_î → 1/2_μ̂}];

In[ ]:= Spin2
Out[ ]= -i |1/2_μ̂⟩·⟨-1/2_μ̂| + i |-1/2_μ̂⟩·⟨1/2_μ̂|

Orbital13 = MatrixToDirac[PauliMatrix[3], {2}, {0_î → v1x_â, 1_î → v1y_â}];

In[ ]:= Orbital13
Out[ ]= |v1x_â⟩·⟨v1x_â| - |v1y_â⟩·⟨v1y_â|
```

Figure A.2: Example of how spin and orbital matrices can be created in *Mathematica* using *Quantum Notation*.

The second section ("Toy Models - No need to Run") is for test calculations of an 8 band Kane model of InSe. In this section, it is shown that constructing the Hamiltonian in the J_z basis or XYZ basis returns the same eigenvalues when proper transformations are performed. However, when calculating the effective mass or the effective g-factor, the XYZ basis must be transformed into the J_z basis.

```
In[ ]:= Hi = (Hc | c_â⟩ · ⟨c_â | ⊗ Spin0 + Ez dz | c_â⟩ · ⟨v_â | ⊗ Spin0
          + e Beta1 / (c me) | c_â⟩ · (Ax ⟨v1x_â | + Ay ⟨v1y_â |) ⊗ Spin0
          + lambdacv2 | c_â⟩ · (1 / 2 ⟨v2x_â | ⊗ Spin1 + 1 / 2 ⟨v2y_â | ⊗ Spin2)
          + Ez dz | v_â⟩ · ⟨c_â | ⊗ Spin0
          + Hv | v_â⟩ · ⟨v_â | ⊗ Spin0
          + lambdavv1 | v_â⟩ · (1 / 2 ⟨v1x_â | ⊗ Spin1 + 1 / 2 ⟨v1y_â | ⊗ Spin2)
          + e Beta2 / (c me) | v_â⟩ · (Ax ⟨v2x_â | + Ay ⟨v2y_â |) ⊗ Spin0
          + e Beta1 / (c me) (Ax | v1x_â⟩ + Ay | v1y_â⟩) · ⟨c_â | ⊗ Spin0
          + lambdavv1 (1 / 2 | v1x_â⟩ · ⟨v_â | ⊗ Spin1 + 1 / 2 | v1y_â⟩ · ⟨v_â | ⊗ Spin2)
          + ( Hv1 ⊗ Spin0 + lambdav1 1 / 2 Spin3 ⊗ Orbital12)
          + lambdacv2 (1 / 2 | v2x_â⟩ · ⟨c_â | ⊗ Spin1 + 1 / 2 | v2y_â⟩ · ⟨c_â | ⊗ Spin2)
          + e Beta2 / (c me) (Ax | v2x_â⟩ + Ay | v2y_â⟩) · ⟨v_â | ⊗ Spin0
          + ( Hv2 ⊗ Spin0 + lambdav2 1 / 2 Spin3 ⊗ Orbital22)) :
```

Figure A.3: Screen shot of the monolayer Hamiltonian for InSe using *Quantum Notation* syntax.

A.2 Monolayer 1L Model - Expand to Original 12 Band Model

In this section, the simple model is extended into the full Magorrian model [42] for monolayer InSe (Figure A.3). The explicit form of $\boldsymbol{k} \cdot \boldsymbol{p}$ perturbation is incorporated as well for consistency (Figure A.4). From this perturbed Hamiltonian, we can acquire the $\boldsymbol{p_x}$ and $\boldsymbol{p_y}$ matrices ($\boldsymbol{p} = -i\hbar\nabla$). These matrices can be used to calculate the effective mass [90]

$$\frac{m_0}{m^*_{nk}} - 1 = \sum_u \frac{|\langle n|\boldsymbol{p_k}|u\rangle|^2}{E_n - E_u}, \tag{A.1}$$

where m_0 is the free electron mass and k indexes x, y, or z momentum. The effective mass for the conduction band was calculated to be $\sim$.14 m_0, which is similar to values found in literature [38], [41]. Confirming that the toy model has been implemented correctly in this code. By taking eigenvalues of the Hamiltonian and the correct matrix elements from the momentum matrices, the out-of-plane effective g-factor can be calculated using eq. 3.8.

```
HiWithCoupling = Hi + I (Ec - Ev) dz kz / e | c_â⟩ · ⟨v_â | ⊗ Spin0 -
  I (Ec - Ev) Conjugate[dz] kz / e | v_â⟩ · ⟨c_â | ⊗ Spin0 +
  Beta1 hbar / me | c_â⟩ · (kx ⟨v1x_â | + ky ⟨v1y_â |) ⊗ Spin0 +
  Conjugate[Beta1] hbar / me (kx | v1x_â⟩ + ky | v1y_â⟩ ) · (⟨c_â |) ⊗ Spin0 +
  Beta2 hbar / me | v_â⟩ · (kx ⟨v2x_â | + ky ⟨v2y_â |) ⊗ Spin0 +
  Conjugate[Beta2] hbar / me (kx | v2x_â⟩ + ky | v2y_â⟩ ) · (⟨v_â |) ⊗ Spin0
```

Figure A.4: Screen shot of the perturbed monolayer Hamiltonian for InSe using *Quantum Notation* syntax.

A.3 Automated Calculations for the Multilayer Hamiltonian

In order to calculate the effective g-factor for different thicknesses, eq. 2.5 was implemented in *Mathematica*. This equation can be broken down into three parts,

$$\hat{H}^N = H_0 + H_{onsite} + H_{interlayer} \tag{A.2}$$

where H_0 is associated with the band energies for layer number N, H_{onsite} describes interactions within the layer, and $H_{interlayer}$ describes interactions between layers.

Using this framework, the multilayer Hamiltonian can be created. The calculation of this Hamiltonian is automated in the *Mathematica* script. By designating ”Nlayers”, or thickness, the code uses the hopping model to ’stack’ the monolayer Hamiltonian N times. Note, the time to compute the multilayer Hamiltonian can be very long. Therefore, the greatest number of layers that is stacked in this code is 14 (which can take several hours to run on an Intel i7 processor). The results for 1L to 14L are saved to ”layer results 10-21-2021.txt”. Values are saved for each thickness: the energy for each band (val), the wave vector for each band (vec), effective mass for each band (meff), the orbital g-factor for each band (gOrb), and the J_z matrix.

A.4 Analysis and Plotting

The text file, ”layer results 10-21-2021.txt”, can be loaded in order to conduct data analysis. Currently, the ”Analysis” section of the *Mathematica* code has several values that are extracted from the text file: layer number, indices for the primary bands, energies for the primary bands, and orbital g-factors for primary bands.

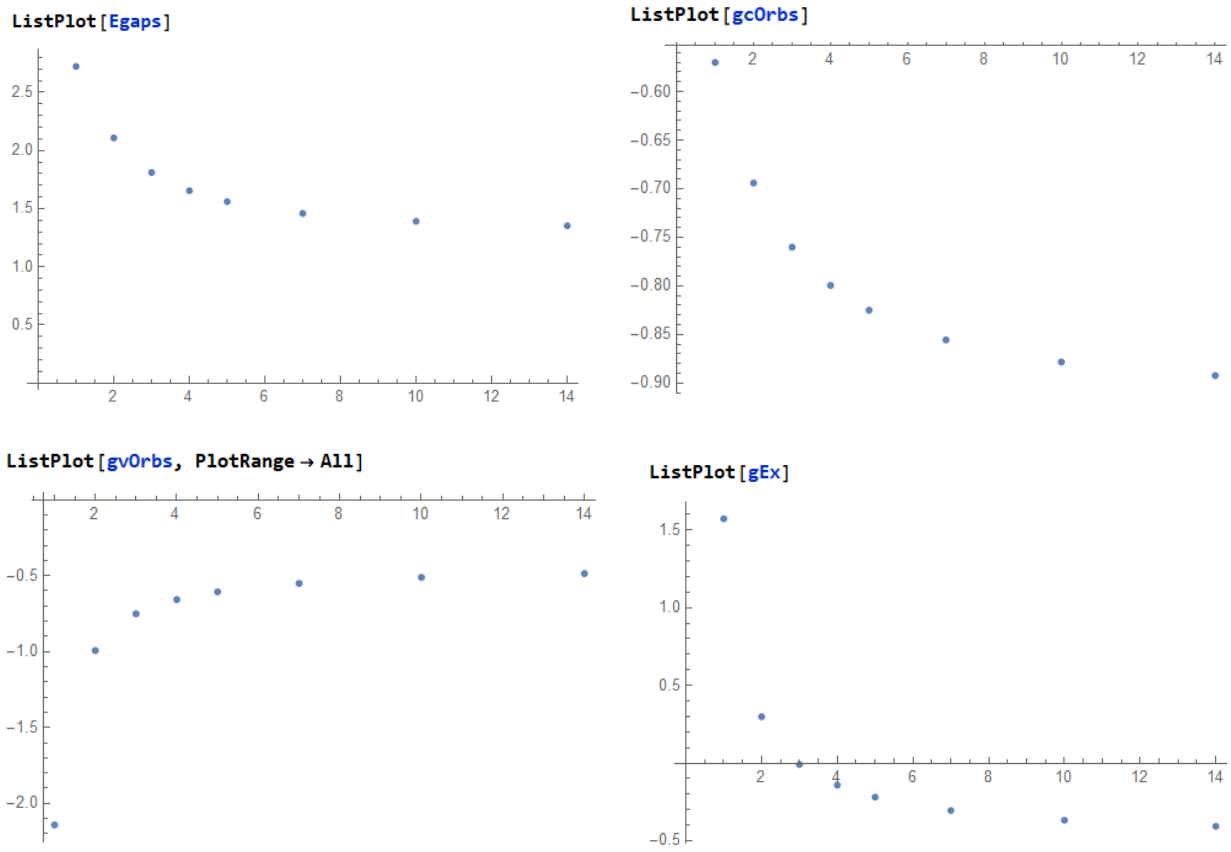

Figure A.5: Plots show band gap energy (Egaps), orbital g-factor of the conduction band (gcOrb), orbital g-factor of the valence band (gvOrb), and excitonic g-factor (gEx).

In the ”Plotting” section, trends can be observed for different parameters with respect to increasing layer number. This includes primary band gap size, orbital g-factor of the conduction

band, orbital g-factor of the valence band, and excitonic g-factor (all shown in Figure A.5). The band gap energy decreases in a non-linear fashion with increasing thickness, this trend matches with results reported in literature [38], [41], [47]. Orbital g-factors, both conduction and valence, have a non-linear change and seem to settle at large thicknesses. The excitonic g-factor is calculated using eq. 3.10.

VITA

Education

2017 B.S Physics, Brown University, Providence, RI

2023 Ph.D Applied Physics, Northwestern University, Evanston, IL

Publications

1. **J. Nelson**, D. Lebedev, M. C. Hersam, and N. P. Stern. Electrical tuning of polarized emission in InSe. In Preperation.

2. **J. Nelson**, T. K. Stanev, D. Lebedev, T. LaMountain, J. T. Gish, H. Zeng, H. Shin, O. Heinonen, K. Watanabe, T. Taniguchi, M. Hersam, and N. P. Stern. Layer-dependent optically induced spin polarization in InSe. Phys. Rev. B 107, 115304 (2023).

3. T. LaMountain, **J. Nelson**, E. J. Lenferink, S. H. Amsterdam, A. A. Murthy, H. Zeng, T. J. Marks, V. P. Dravid, M. C. Hersam and N. P. Stern. Valley-selective optical Stark effect of exciton-polaritons in a monolayer semiconductor. Nature Communications volume 12, 4530 (2021).

4. **J. Nelson,** C. M Bhat, and B. S. Hendricks. Online Measurement of the Energy Spread of Multi-turn Beam in the Fermilab Booster at Injection. Proceedings of HB2016, Malmo, Sweden, 237 (2016).

5. CMS Collobration. Characterisation of irradiated thin silicon sensors for the CMS phase II pixel upgrade. The Euro-pean Physical Journal C 77, 567 (2017).

Conference Presentations

- ”Layer dependent spin properties in InSe”. APS March Meeting 2022. Chicago, IL
- ”Probing spin dynamics in InSe with time-resolve Kerr rotation”. APS March Meeting 2021
- ”Spin relaxation in InSe probed by time-resolved Kerr rotation”. APS March Meeting 2020
- ”Ultrfast Pump-Probe Spectroscopy of Quasiparticles Dynamics in Supercon- ducting Radio Frequency Cavities”. Northwestern BGSA Research Conference. Chicago, IL
- ”A Computer Program to Measure the Energy Spread of Multi-turn Beam in the Fermilab Booster at Injection”. APS April Meeting 2016. Salt Lake City, UT